

Austenite formation in C-Mn steel

PhD thesis

Viktorija I. Savran

The research described in this thesis was performed in the department of Materials Science and Technology, the Delft University of Technology



This research was carried out as part of the innovation program of the Materials Innovation institute (M2i) (formally, the Netherlands Institute for Metals research) on the “A study of the ferrite to austenite heating transformation in order to better control the microstructure in cold-rolled annealed multiphase steels” project number MC5.03171



Austenite formation in C-Mn steel

PROEFSCHRIFT

ter verkrijging van de graad van doctor
aan de Technische Universiteit Delft,
op gezag van de Rector Magnificus prof. dr. ir. J.T. Fokkema,
voorzitter van het College voor Promoties,
in het openbaar te verdedigen op maandag 23 februari 2009 om 15:00 uur

door

Viktorija Ivanivna SAVRAN

materiaalkundig ingenieur
Zaporozhye State Technical University (Ukraine)
Technische Universiteit Delft (the Netherlands)
geboren te Zaporizhzhya, Ukraine

Dit proefschrift is goedgekeurd door de promotor:
Prof. dr. ir. L.A.I. Kestens

Toegevoegd promotor: Dr. ir. J. Sietsma

Samenstelling promotiecommissie:

Rector Magnificus, voorzitter

Prof. dr. ir. Leo Kestens, Technische Universiteit Delft, promotor

Dr. ir. Jilt Sietsma, Technische Universiteit Delft, toegevoegd promotor

Prof. dr. Matthias Militzer, University of British Columbia, Vancouver, Canada

Prof. dr. Andy Howe, University of Sheffield, UK

Prof. dr. Guido Janssen, Technische Universiteit Delft

Dr. ir. Erik Offerman, Technische Universiteit Delft

Dr. ir. Yvonne van Leeuwen, VROM Inspectie, Kernfysische Dienst

Prof. dr. I.M. Richardson, Technische Universiteit Delft, reservelid

ISBN: 978-90-77172-40-7

Keywords: austenitization, ferrite, pearlite, austenite, cementite, austenite growth kinetics, phase field modeling, microstructure simulation, synchrotron radiation, dilatometry

Copyright © 2009 by V.I. Savran

All rights reserved. No part of the material protected by this copyright notice may be reproduced or utilized in any form or by any means, electronic or mechanical, including photocopying, recording or by any information storage and retrieval system, without written permission from the author.

Printed in the Netherlands

*This thesis is dedicated with love
to my husband Sebastiaan*

Content

1. Introduction	1
1.1. Steel and its phases	1
1.2. Phase diagram	2
1.3. Austenitization	3
1.4. This thesis	4
<i>References</i>	6
2. Background	7
2.1. Experimental	8
2.1.1. The formation of austenite in pure iron: ferrite	8
2.1.2. The formation of austenite in steels	8
2.1.2.1. The formation of austenite from lamellar pearlite in eutectoid steels	9
2.1.2.2. The formation of austenite from pro-eutectoid ferrite and pearlite in hypo-eutectoid steels	13
2.2. Modeling	16
<i>Summary</i>	18
<i>References</i>	19

Part I. Experimental

3. Material and experimental techniques	21
3.1. Material	22
3.2. Experimental techniques	23
3.2.1. Optical and scanning electron microscopy (OM and SEM)	23
3.2.2. Electron probe microanalysis (EPMA)	24
3.2.3. Dilatometry	25
3.2.4. Three dimensional X-ray diffraction microscopy (3DXRD)	28
<i>References</i>	29
4. Microstructural features of austenite formation in C35 and C45 alloys	31
4.1. Introduction	32
4.2. Theoretical background	33
4.2.1. Driving force for nucleation in hypo-eutectoid steel	33
4.2.2. Temperature range 1: $A1 < T < A3$	35
4.2.3. Temperature range 2: $T > A3$	37
4.3. Experimental procedure	38
4.4. Results	38
4.4.1. Nucleation	38

4.4.2. Growth morphologies	41
4.5. Discussion	44
4.5.1. Nucleation	45
4.5.2. Growth morphologies	46
4.6. Conclusions	47
<i>References</i>	48
5. Austenite nucleation and growth on the level of individual grains observed by 3DXRD microscopy	49
5.1. Introduction	50
5.2. Background	50
5.2.1. Nucleation	50
5.2.2. Growth	53
5.3. Results and discussion	55
5.3.1. Volume fraction	55
5.3.2. Nucleation	56
5.3.3. Growth types of individual grains	60
5.4. Conclusions	64
<i>References</i>	64

Part II. Modeling

6. Two-dimensional phase field model for the pearlite+ferrite-to-austenite transformation during continuous heating	67
6.1. Introduction	68
6.2. Model formulation	68
6.2.1. Phase field concept	69
6.2.2. Nucleation	74
6.3. Experimental and simulation conditions	75
6.3.1. Materials and dilatometric measurements	75
6.3.2. Simulation conditions	75
6.4. Results and Discussion	78
6.4.1. Volume fractions	78
6.4.1.1. Overall austenite volume fraction	78
6.4.1.2. Ferrite and pearlite volume fractions	82
6.4.2. Evolution of the microstructure and carbon content	84
6.4.3. Growth types of individual grains	88
6.5. Conclusions	91
<i>References</i>	92

7. Carbon redistribution during continuous heating of the pearlite-ferrite microstructure	95
7.1. Introduction	96
7.2. Simulation conditions	97
7.3. Results and discussion	97
7.4. Conclusions	106
<i>References</i>	106
8. Detailed phase-field modeling of austenite growth in a ferrite-pearlite structure	109
8.1. Introduction	110
8.2. Simulation conditions	110
8.3. Results and discussion	114
8.3.1. Austenite growth near the source of carbon	119
8.3.2. Austenite growth away from the source of carbon	122
8.4. Conclusions	126
<i>References</i>	126
Summary	127
Samenvatting	131
Acknowledgments	135
List of publications	137
Curriculum vitae	139
Appendix	141

Chapter 1

Introduction

1.1. Steel and its phases

One of the most abundant metals on our planet is *Iron*. It forms up to 35 % of the mass of the Earth as a whole [1]. Due to its rather easy accessibility and manufacturing, iron is the most used of all the metals. Its combination of low cost and high strength makes it irreplaceable, especially in applications like automobiles, structural components for buildings *etc.*

The best-known alloy of iron is *steel* [1]. Iron and *Carbon* are the basic elements of all steels, but depending on the application of the steel product, other alloying elements can be added to improve the properties and meet the requirements for a certain application. Changing the chemical composition of the steel by adding alloying elements is not the only way to influence the properties of the final product. The other possibility to influence the properties - *heat treatment* - is related to the fact that at different temperatures iron in equilibrium has different *crystallographic lattices*, i.e. the arrangement of atoms that repeats periodically in three dimensions. Depending on the material composition, up to the transition temperature A_3 (see Fig. 1.1) and at very high temperatures (between 1400 °C and 1539 °C) iron has the *body centered cubic (bcc)* structure, named *ferrite*, and at intermediate temperatures iron has the *face centered cubic (fcc)* atomic structure, named *austenite* [1]. Carbon is a relatively small interstitial atom that tends to fit into the octahedral voids of the iron lattice. It strengthens steel and gives it the ability to harden by heat treatment. *Ferrite* at equilibrium contains a maximum of 0.025 wt. % (0.116 at. %) carbon at 727 °C and 0.008 wt. % (0.037 at. %) carbon at room temperature. *Austenite* can contain up to 2.0 wt. % (9.0 at. %) of carbon.

Another phase, which is quite often present in steels, is *cementite* (Fe_3C). Unlike ferrite and austenite, cementite is a very hard intermetallic compound consisting of 6.7 wt. % (25 at. %) of carbon [1]. Cementite is very hard and therefore can act as the strengthening phase in steel.

An important structural constituent to mention is *pearlite*. Pearlite is not a single phase, but a mixture of alternating lamellae of ferrite (α) and cementite (Fe_3C) in a single grain [1]. Pearlite forms by an eutectoid reaction when austenite is slowly cooled below 727 °C. The eutectoid composition of austenite is approximately 0.8 wt. % (3.7 at. %) carbon; steel with less carbon will contain a corresponding portion of ferrite that does not participate in the eutectoid reaction.

The last two phases that have to be mentioned are *martensite* and *bainite*. They are not stable phases and thus not shown on the phase diagram. *Martensite* is

formed by rapid cooling (quenching) of austenite, which traps carbon atoms that do not have time to diffuse out of the crystal structure. It is a rather hard phase and is formed by displacive transformation below the martensite start temperature (M_s). The difference between martensite and austenite is that martensite has a body centered tetragonal crystal structure, whereas austenite has a face centered cubic structure. *Bainite* is another decomposition product that may form when austenite is cooled past a critical temperature of 727 °C, but normally forms in the range 250-450 °C. A fine non-lamellar structure, bainite commonly consists of ferrite and cementite or other carbide. It is in constitution similar to pearlite, but with the ferrite forming by a displacive mechanism similar to martensite formation, usually followed by precipitation of carbides from the supersaturated ferrite or austenite. The temperature range for transformation to bainite is between those for pearlite and martensite. When formed during continuous cooling, the cooling rate to form bainite is higher than that at which pearlite forms, but lower than that to form martensite, in steel of the same composition.

1.2. Phase diagram

The most widely-used way to represent the existence of the different phases in equilibrium depending on temperature and carbon content is by means of a phase diagram. A phase diagram is a type of graph that shows the equilibrium conditions for the thermodynamically distinct phases. The Fe-C phase diagram is shown in Fig. 1.1 [2]. Depending on the carbon concentration in the steel, the diagram is divided into four parts:

- a) *hypo-eutectoid* steels, which contain less than 0.80 wt. % of carbon;
- b) *eutectoid* steel, which contains 0.80 wt. % of carbon;
- c) *hyper-eutectoid* steels, which contain more than 0.80 wt. % of carbon;
- d) *cast irons*, which contain more than 2 wt. % of carbon.

In this thesis only the hypo-eutectoid part of the diagram, where the carbon content is less than 0.80 wt. %, is considered. Typical hypo-eutectoid steel at room temperature has a pearlite-ferrite microstructure with different phase fractions, which are determined by the amount of carbon in the steel. In order to influence the properties of the steel, some alloying elements other than carbon, like manganese, chromium, vanadium, tungsten *etc.* can be added. In general, two types of alloying elements can be distinguished in accordance to their solubility in the iron matrix. Interstitially dissolved elements, like carbon and nitrogen, and substitutionally dissolved elements, like manganese, chromium *etc.* Interstitial elements are usually located in the octahedral voids; whereas substitutional elements are located at the same lattice sites as iron atoms.

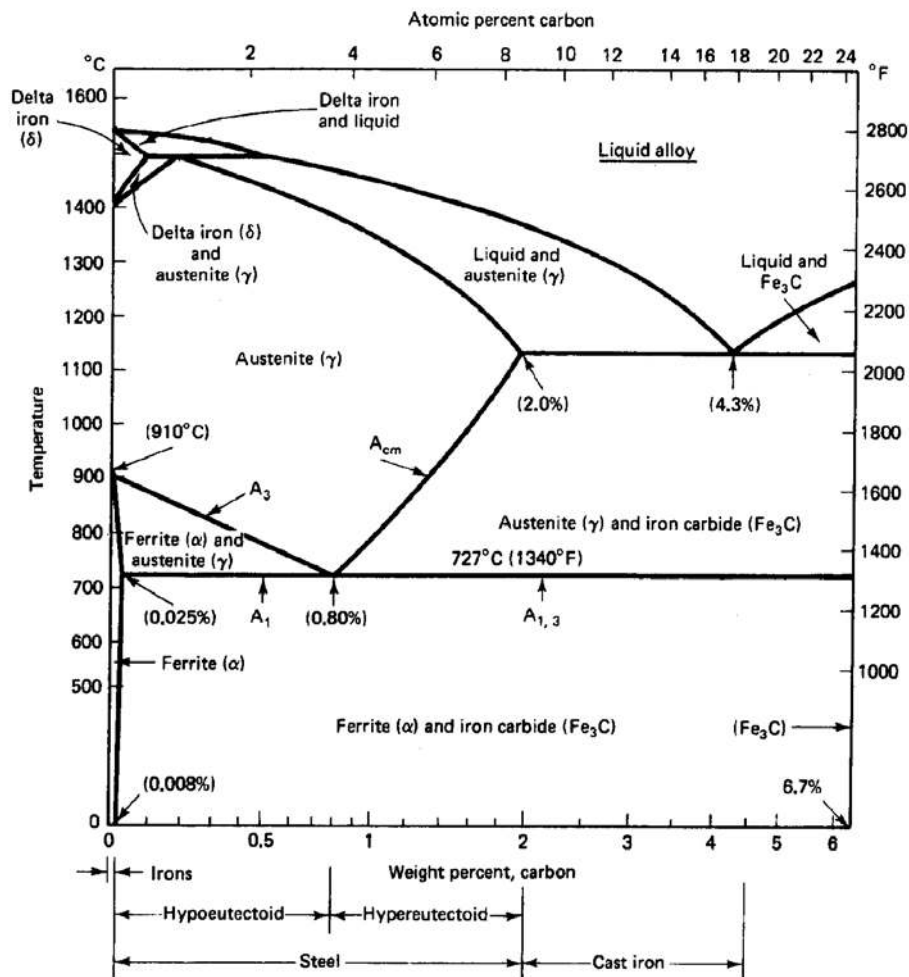


Figure 1.1. Fe-C Phase diagram, indicating the thermodynamically stable phases as a function of carbon concentration and temperature [2].

1.3. Austenitization

In the process of steel making, in order to obtain the desired mechanical and physical properties of the final product, almost always suitable heat treatment(s) must be performed. The first step in a heat treatment process is *austenitization* [3], which has a strong influence on the final properties of the structure of the material. In order to induce austenitization the material is heated from room temperature, where a hypoeutectoid steel typically has a ferrite+pearlite microstructure, through the two-phase region (ferrite+austenite) to the one-phase austenite region. The main features of austenitization are:

- a) constant increase in atom mobility and driving force with increasing temperature. With increasing overheating the phase transition accelerates due to the increased nucleation and growth rates;

- b) formation of a one-phase structure (austenite) with homogeneous carbon distribution from a two-phase mixture (ferrite-pearlite). The transformation of bcc structure into fcc structure is complicated by the carbon redistribution between the phases.

A major interest in austenitization was raised during the present development of Dual-Phase (DP) and Transformation Induced Plasticity (TRIP) steels. These new generations of multiphase steels promise a strip material for automotive applications with an optimum combination of high strength and ductility. At present, the principal factor used to tailor the properties of DP steels is the total volume fraction of martensite in the final microstructure. TRIP steels are more complex, but final properties are largely manipulated using the bulk chemistry and cooling cycles to provide a complex phase mixture containing retained austenite. In both cases little control of the size distribution, spatial distribution and geometry of the microstructural constituents is exercised. This is in part due to the practical limitations imposed by existing production lines, but is also due to a shortfall in the understanding of the evolution of the microstructure during austenitization and parameters that control it. Optimization of multiphase products will be much more efficient with this understanding.

1.4. This thesis

The aim of the thesis is to develop knowledge and to gain better understanding of the formation of the austenite microstructure in steel during heating, e.g. austenite nucleation kinetics, austenite growth modes and morphologies, redistribution of carbon between the phases during the transformation. Although the phase transformations that take place during cooling from austenitic temperatures have extensively been studied, the transformation during heating has drawn little attention. Nevertheless, it is during this process that the blueprint for the eventual microstructure is being formed, like the phase fractions and the spatial and size distribution of the ferrite and the martensite, bainite grains.

The content of the thesis is arranged as follows:

Chapter 2 gives an overview of the literature on the austenite formation from different initial microstructures (ferrite, pearlite, ferrite+pearlite), both in experimental studies and simulations.

Chapter 3 describes the alloys used in this project as well as the characteristics of different techniques used for the experimental research presented in this thesis: optical and scanning electron microscopy (OM and SEM) [4, 5]; electron probe micro analysis (EPMA) [6]; dilatometry [7] and three-dimensional X-ray diffraction microscopy (3D-XRD) [8].

In **chapter 4** the microstructural features of austenite formation are studied using OM, SEM and EPMA. It is shown that formation of the austenitic phase upon heating is possible in pearlite as well as in ferrite regions; however in the second case it proceeds at a much lower rate, as carbon has to diffuse from the carbon-rich regions (former pearlite, acting as a source of carbon). The character of the pearlite-to-

austenite transformation is shown to be dependent on the heating rate. The formation of metastable austenite (containing 0.27 wt. % C) on the ferrite-ferrite grain boundaries is described and a possible explanation, which is based on thermodynamic considerations, is given. It is also shown that carbon inhomogeneities are responsible for some specific phenomena observed in the α/γ structure. The formation of a finger-type austenite, a specific growth morphology, occurs on the pearlite-ferrite grain boundaries and coincides with the position of cementite plates. In locations where the direction of the cementite lamellae is not perpendicular to the grain boundary, the formation of a “black” phase, bainite, takes place.

Chapter 5 presents the results on the austenite nucleation and growth measured on the level of individual grains using 3D-XRD microscopy. The unique experimental data on austenite nucleation show two different nucleation regimes: initial fast nucleation, most likely on pearlite colonies, and slower nucleation on the ferrite/ferrite grain boundaries. **Chapter 5** also presents the kinetics of individual austenite grains growing during ferrite+pearlite decomposition into austenite. A quantitative model interpretation of the nucleation and growth data is given.

Chapter 6 presents a model for the ferrite+pearlite-to-austenite transformation, which is based on the phase-field approach. The model is able to describe qualitatively and quantitatively the pearlite+ferrite-to-austenite transformation during continuous heating. The pearlite phase is considered to be a single phase with a uniform composition. Nucleation is described by the Classical Nucleation Theory (CNT) [9]. The interface mobility, governing the growth rate, is used as a fitting parameter to fit the experimental and the simulated austenite volume fraction curves. A good agreement in the development of the simulated and experimental microstructure is observed. The derived carbon profiles show the development of strong carbon gradients with increasing heating rate. The refinement of the microstructure with increasing the heating rate is also captured by the model.

In **chapter 7** the redistribution of carbon during austenitization is studied in detail using the model developed in **chapter 6**. It is shown that the character of the phase transformation indicated by the concentration of carbon in austenite on the austenite-ferrite interface, strongly depends on the heating rate. A transition from the diffusion-controlled mode to interface-controlled mode with increasing heating rate is thus observed and analyzed. The well-established assumption of the diffusion-controlled mode for the ferrite-to-austenite transformation upon heating is only applicable for a relatively narrow range of low heating rates. For most heating rates that are of interest to the industry a mixed-mode approach will give a better representation of the transformation.

Finally, in **chapter 8**, different austenite nucleation sites, near the source of carbon (pearlite-ferrite boundary) and away from the source of carbon (ferrite-ferrite boundary) are analyzed by means of phase-field modeling. It is shown that austenite grains on the pearlite-ferrite grain boundary grow almost 10 times faster than the ones growing on the ferrite-ferrite grain boundary. This is directly related to the carbon concentration profiles. A highly inhomogeneous carbon distribution develops during the transformation, both in ferrite and austenite, and some time is necessary to obtain a homogeneous (in carbon) microstructure. Carbon gradients that develop during the

isothermal holding in the ferrite phase play a crucial role in the austenite transformation kinetics.

References

- [1] *Handbook of chemistry and physics*. Boca Raton (FL): CRC Press; 1989.
- [2] H.W. Pollack, *Materials Science and Metallurgy*, 4th ed., Englewood Cliffs, NJ: Prentice-Hall, Inc, 1988, p. 554.
- [3] C.R. Brooks, *Principles of the austenitization of steels*, Elsevier Science Publishers, England, 1992.
- [4] H.C. Sörby, *J. Iron Steel Ins. (London)*, 1886, pp. 140-144.
- [5] M. Knoll, E. Ruska, *Z. Phys.*, 1932, vol. 78, pp. 318-339
- [6] D.B. Wittry, Electron Probe Microanalyzer, US Patent No 2916621, Washington, DC: U.S. Patent and Trademark Office, 1958.
- [7] T. A. Kop, *A dilatometric study of the austenite/ferrite interface mobility*, PhD Thesis, TU Delft, the Netherlands, 2000, p.130.
- [8] H.F. Poulsen, *Three-dimensional X-ray diffraction microscopy: mapping polycrystals and their dynamics*, Springer, 2004, p. 156.
- [9] H.I. Aaronson, J.K. Lee, In: *Lectures on the Theory of Phase transformations*, Met. Soc., New York, 1977.

Chapter 2

Background

Abstract

In the first part of this chapter the experimental evidence that is available on the austenitization of ferrite, pearlite and ferrite+pearlite microstructures, will be presented. The investigators in the literature pointed out the complexity of the austenite formation, in that the austenite is nucleating and growing from different sites in the initial microstructures consisting of different phases (ferrite and pearlite, which is a mixture of ferrite and cementite), with different degrees of stability. Pearlite-to-austenite transformation is a much faster process than ferrite-to-austenite transformation [1]. Possible nucleation sites in a ferrite-pearlite structure are claimed to be the grain boundaries, edges and corners.

In the second part of this chapter modeling methods that are used for modeling solid phase transformations will be presented. Among all the models and techniques, *phase-field* theory will be addressed in particular as the modeling part of the thesis is based on this approach.

2.1. Experimental

2.1.1. The formation of austenite in pure iron: ferrite

In pure iron, the rate of formation of austenite from ferrite is quite rapid, and even the use of a very high (i.e. $10,000^{\circ}\text{C/s}$) heating rate cannot suppress the transformation to a great extent [2]. Figure 2.1 shows some data illustrating this effect. There is only a very small change in the transformation temperature ($\sim 50^{\circ}\text{C}$) over the heating rate range of 0-20,000 $^{\circ}\text{C/s}$ [3]. Such data show that the nucleation and growth of austenite in pure iron is very rapid.

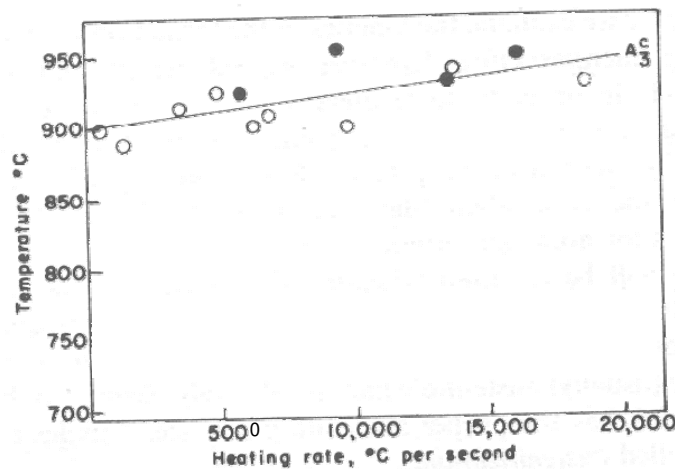


Figure 2.1. The effect of heating rate on the temperature at which ferrite transforms to austenite in pure iron (upper curve), after [3]. The symbols show two different sets of data.

2.1.2. The formation of austenite in steels

The situation for forming austenite is different from the transformation process during cooling. As the temperature is raised into the austenite region, the free energy change increases (this is the difference in the free energy of the product phase, austenite, and the parent phases, such as pearlite or ferrite). Thus, the rate of formation of austenite should increase with increasing temperature. Also, with increasing temperature the atomic mobility increases. Thus both the thermodynamic driving force for the formation of austenite and the atomic mobility become larger with higher temperatures, and therefore the rate of nucleation and the rate of growth will continuously increase with increasing temperature.

2.1.2.1. The formation of austenite from lamellar pearlite in eutectoid steels

Once a suitable temperature has been reached, and this needs to be only slightly above the A_1 temperature (see Fig. 1.1), austenitization of eutectoid steel proceeds by four distinct steps [4], namely:

- a) pearlite remains unaffected for a short incubation period;
- b) transformation of “pearlitic” ferrite to austenite, which occurs by nucleation followed by growth;
- c) transformation of cementite into the newly formed austenite; and
- d) diffusion of carbon away from the cementite-austenite interface into the austenite.

As an austenite region grows in pearlite, at the austenite-pearlite interface the eutectoid reaction of ferrite+carbide→austenite occurs. The possible sites for nucleation of austenite in this case are [4, 5]:

- a) the interface between the cementite and ferrite plates in the pearlite colony (site 1 in Fig. 2.2).
- b) the grain boundaries (site 2 in Fig.2.2).

As was mentioned by several authors [4-9], the second site is the most favorable. Nucleation of austenite within the pearlitic structure occurs preferentially at the intersection of pearlite colonies (grain boundaries) (see Fig. 2.3a, b). New grains of austenite nucleate at the boundaries and a pearlite colony can contain more than one new austenite grain (see Fig. 2.3b).

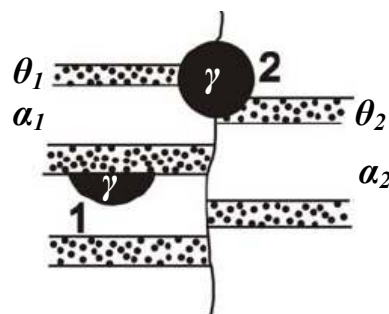


Figure 2.2. Possible nucleation sites for austenite in the pearlite structure. 1) the interface between the cementite and ferrite plates in the pearlite colony, 2) the pearlite-pearlite grain boundaries. α =ferrite, θ =cementite, γ =austenite [4].

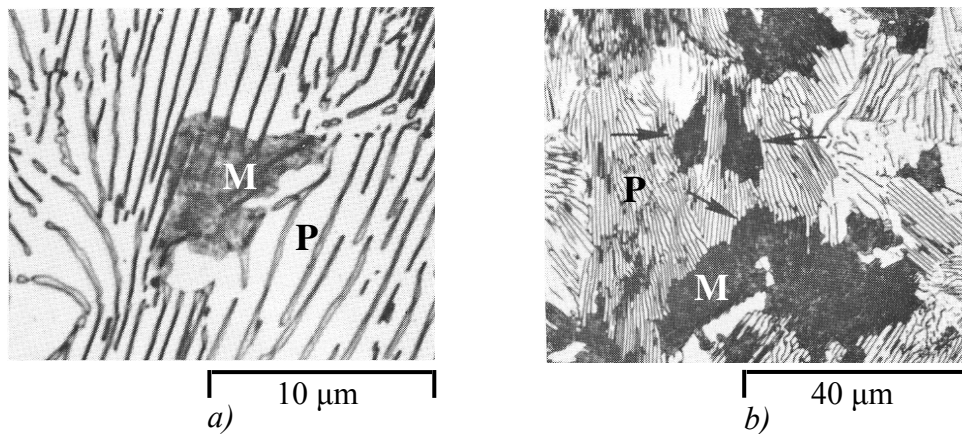


Figure 2.3. Formation of austenite from lamellar pearlite in 0.8 wt. % C steel, heated at 730 °C for a) 20 s and b) 40 s. Arrows indicate three individual austenite grains initiated in a single pearlite colony. Etchant: a) picral, b) bisulfite. P=pearlite, M=martensite (austenite at higher temperatures) [9].

According to Mehl [6], the density of potential nucleation sites in pearlite is much higher than the experimentally observed density of austenite grains formed. Careful examination of the microstructure of austenite, which has formed from pearlite, shows that the austenite grains preferentially nucleate at the interface between pearlite colonies (on the pearlite-pearlite grain boundaries). At this location, the boundaries separating the ferrite in one pearlite colony from that of the other and that between the carbide in the two colonies, both are high angle boundaries.

Similar observations were made by Speich *et al.* [4]. They observed that the nucleation rate of austenite in the pearlite structure was not very high, in spite of the large amount of interfacial area on which nucleation can occur. The surface energy is known to be a function of the lattice mismatch between two crystals and a high angle boundary would favor nucleation. This appears to be the reason for the lack of nucleation on the ferrite-carbide interfaces of pearlite. Nucleation occurs at the high angle boundary between pearlite colonies, where the surface energy is more favorable.

The new grains of austenite grow laterally along the plates of ferrite in a pearlite colony and expand to replace the ferrite in the colony. An interesting observation was made by Speich *et al.* [4]. They noticed that the austenite growth front is not planar and the pearlite-austenite interface is considerably deformed. The cementite plates dissolve in this austenite, but the austenite grains grow at a faster rate than that at which the cementite plates dissolve (Fig. 2.3a; 2.4a, b). This residual cementite is first plate-like, then breaks up (Fig. 2.4a–c) and completely dissolves (Fig. 2.4d). This sequence can be well advanced in some regions, while other regions of a parent pearlite colony are still unaffected (Fig. 2.4b).

Indications of the previously existing cementite plates usually are visible for a short period after the cementite itself has disappeared (Fig. 2.4c) due to the in-

homogeneous distribution of carbon in the austenite during this period, but these traces also disappear in time (see Fig. 2.4d) [9].

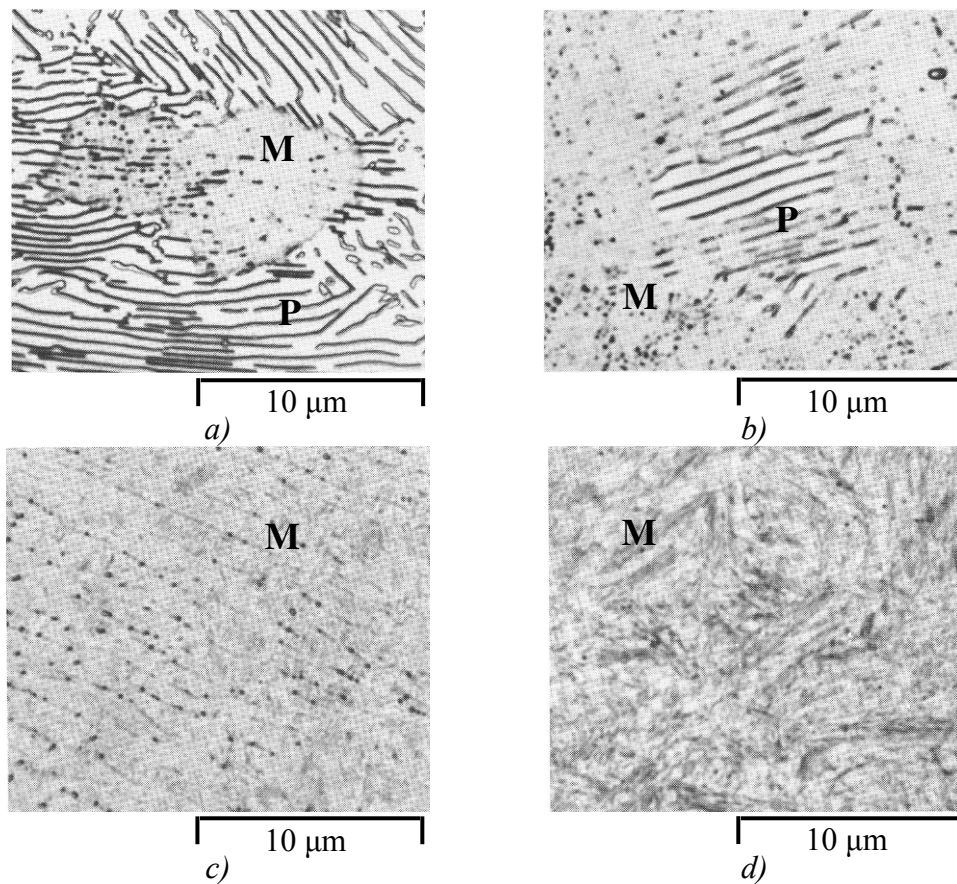


Figure 2.4. Formation of austenite from lamellar pearlite in 0.8 wt. % C steel, annealed at 730 °C for a) 26 s, b) 30 s, c) 60 s and d) 300 s. Etchant: picral. P=pearlite, M=martensite (austenite at higher temperatures) [9].

Figure 2.5 shows data of the carbon content of austenite as a function of austenitizing time for a 1.27 wt. % C steel [10]. The austenitizing temperatures are all in the two-phase austenite+iron carbide region. The carbon content of the austenite at equilibrium is given by the solubility limit at the temperature of interest. The time for the disappearance of ferrite is marked by the arrows. For example, at 800 °C, the ferrite is transformed after about 1 s, at which time the carbon content of the austenite is about 0.6 wt. %. This continuously increases with time as more carbide is dissolved, attaining the equilibrium value of about 0.8 wt. % in about 1 h. (Note that the final carbon content from the figure is slightly different from that obtained from the iron-carbon phase diagram because the steel used in this study contains 0.36 % Mn and 0.19 % Cr).

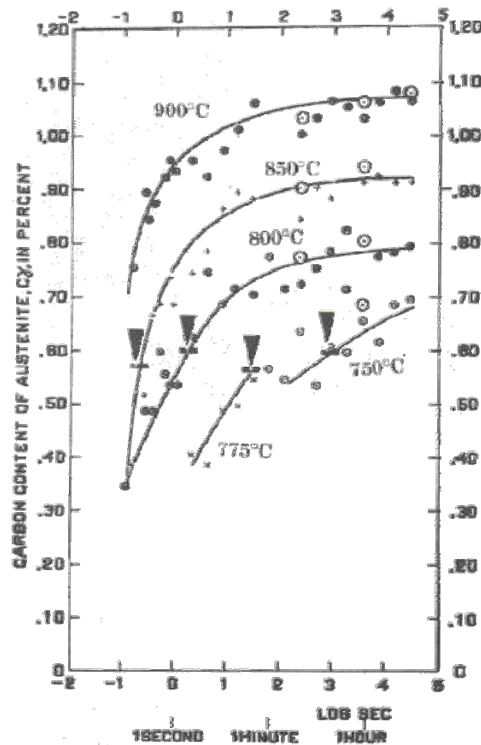


Figure 2.5. Carbon content of austenite as a function of austenitizing time and temperature for a 1.27 % C steel. The arrows mark the time for the disappearance of ferrite [10].

Studies on the austenite growth rates [4, 7, 11, 12] into pearlite showed that the dissolution process is controlled by the diffusion of carbon in the growing phase, and it was assumed that the effective diffusion distance is approximately equal to the interlamellar spacing of pearlite. Roósz *et al.* [2] studied the isothermal formation of austenite in eutectoid steel and suggested that the austenite growth rate, \dot{G} , in general form can be expressed as:

$$\dot{G} \propto \frac{1}{\sigma_0^2} \quad (2.1)$$

where σ_0 is the interlamellar spacing of pearlite.

Caballero *et al.* [13], studying the effect of the initial microstructure on the austenitization, concluded that the austenite formation starts at a higher temperature for coarser pearlite. Also, the transformation rates are slower for a coarser initial pearlite microstructure. The same effect was previously observed by Mehl [6].

Summarizing, the following sequence of events occurs during austenitization of pearlitic structure after the steel reaches the austenitizing temperature:

1. The pearlite remains unaffected for a short incubation period.
2. Nucleation of austenite takes place preferentially at the colony boundaries (pearlite-pearlite grain boundaries).
3. The ferrite begins to transform to austenite; cementite dissolves in this austenite, but at a slower rate. The structure during this stage consists of a mixture of pearlite, austenite and cementite.
4. Some undissolved cementite remains when all ferrite in a pearlite colony has transformed to austenite. The structure during this stage consists of a mixture of austenite and cementite.
5. The cementite dissolves completely but the austenite is inhomogeneous in composition, the carbon content being highest at the location of pre-existing cementite plates. The structure during this stage consists of inhomogeneous austenite.
6. Homogeneous austenite is produced by diffusion of carbon away from the original sites of the cementite plates.

2.1.2.2. The formation of austenite from pro-eutectoid ferrite and pearlite in hypo-eutectoid steels

Transformation of the pearlitic regions at temperatures above the A_1 temperature occurs by the same processes as mentioned for the lamellar pearlite (see section 2.1.2.1). Upon heating, the pearlite regions, which contain about 0.8 wt. % C, become unstable above the eutectoid temperature and transform to austenite. Nucleation takes place predominantly on the pearlite-ferrite grain boundaries [7]. The pearlite phase is the first one that transforms to austenite [1]. After the pearlite-to-austenite transformation is completed, the structure consists of regions of austenite, replacing the original areas of pearlite, and regions of unaffected pro-eutectoid ferrite (see Fig. 2.8a and 2.8b). The pro-eutectoid ferrite is continuously reduced with increasing austenitizing temperature (Fig. 2.8c) and disappears completely after the A_3 temperature is exceeded (Fig. 2.8d) [9]. Simultaneously, carbon in the austenite regions (formed from pearlite colonies) is diffusing to the austenite formed from the ferrite regions. It is adopted that solution of pro-eutectoid ferrite is a diffusion-controlled process, for which the rate-controlling factor is the diffusion of carbon in austenite [9].

Dykhuisen *et al.* [14], who studied the austenitization in low carbon steel, suggested some overlap between the pearlite-to-austenite and ferrite-to-austenite transformations. The authors estimated that the transformation of ferrite does not start until 10 % of pearlite is transformed to austenite. They argued that ferrite cannot transform at temperatures slightly above the eutectoid temperature until carbon is available from the pearlite regions. The transformation process is limited by the diffusion of carbon in austenite. The transformation of ferrite proceeds at a much lower rate than the transformation of pearlite.

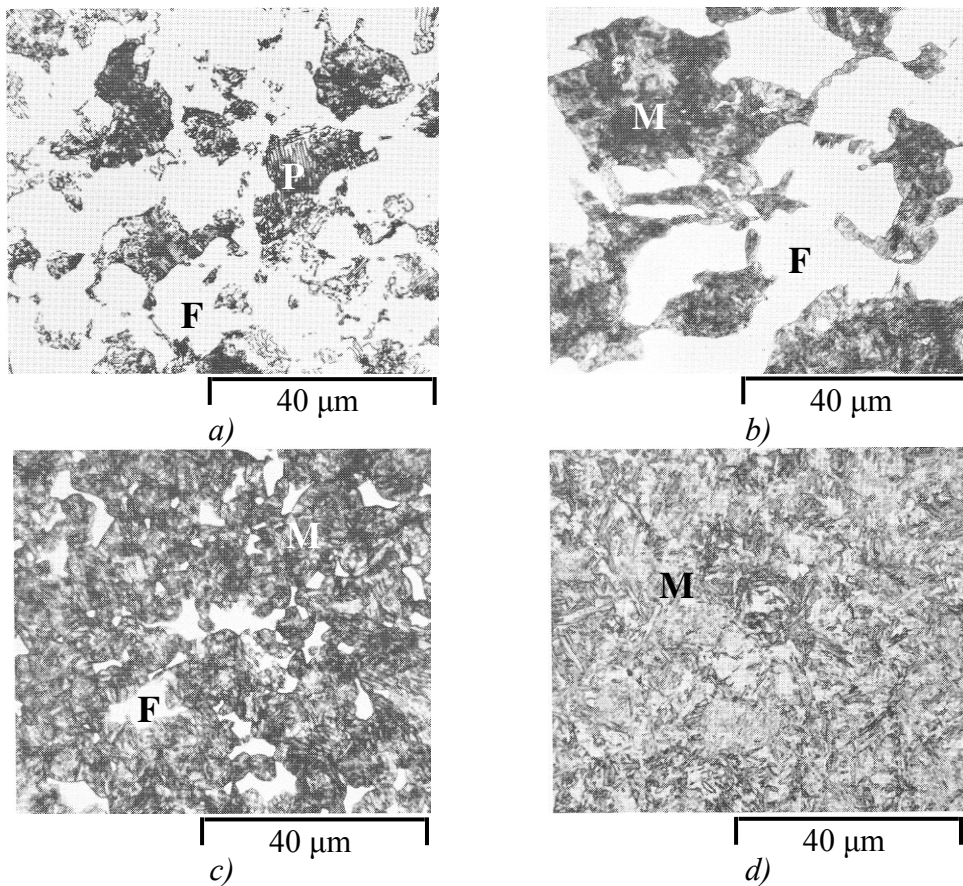


Figure 2.8. Formation of austenite from pearlite and pro-eutectoid ferrite in 0.4 wt. % C steel, heated for 15 min at a) as received, b) 740 °C, c) 770 °C and d) 795 °C. Etchant: picral. F=ferrite, P=pearlite, M=martensite (austenite at higher temperatures) [9].

Recently, Schmidt *et al.* [15, 16] who studied the austenite formation from a ferrite-pearlite microstructure during continuous heating using hot-stage confocal microscopy, observed that at low heating rates the formation of austenite is controlled by the long-range diffusion of carbon. However, at higher heating rates under certain conditions (above the T_0 temperature) the growth rate increased drastically and the interface-controlled reaction growth mechanism was claimed to be responsible for the transformation. Thus, results appear to suggest that assuming long-range diffusion of carbon to be determining for different heating conditions might not be accurate and a change from diffusion-controlled to interface-controlled transformation can be expected during austenitization of steels with a pearlite-ferrite microstructure.

Figure 2.9 shows the fraction of austenite as a function of temperature for three heating rates [14]. The initial pearlite-to-austenite transformation proceeds faster than the subsequent ferrite-to-austenite transformation. As expected, the reaction is

shifted to higher temperatures for the higher heating rates. The main difference is in the slopes of the curves after the transition from pearlite dissolution to proeutectoid ferrite dissolution.

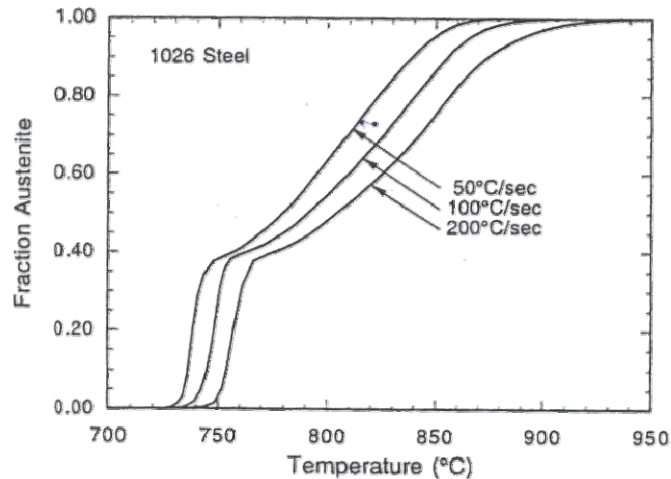


Figure 2.9. Austenite fraction formed as a function of temperature for the heating rates of 50, 100 and 200 °C/s [14].

Datta *et al.* [1] carried out a quantitative microstructural analysis of the austenitization kinetics from a pearlite/ferrite initial microstructure at different intercritical annealing temperatures in low-carbon steel, containing 0.15 wt.% C. They pointed out that at all tested temperatures the pearlite-to-austenite transformation was completed in less than one second. The kinetics of the ferrite-to-austenite transformation at higher temperatures ($T \geq 870$ °C, above A_3) was found to be different from those tested at lower temperatures ($T < 870$ °C, below A_3). At higher temperatures, in the single-phase region, the growth kinetics approaches a constant level at longer times.

After the ferrite/pearlite transformation to austenite is completed, and that has to be above the A_3 temperature, the carbon concentration gradients remain in austenite for a certain time. In the regions of the former pearlite grains there is an excess of carbon, whereas in the regions of the former ferrite grains there is a lack of carbon. These concentration gradients, which are to great extent determined by the heating rate, can remain for some certain time but eventually vanish and a homogeneous in carbon content austenitic structure is formed.

Summarizing, the austenitization of the ferrite-pearlite structure proceeds in three major steps:

- 1) pearlite dissolution and growth of austenite into pearlite (fast process);
- 2) ferrite-to-austenite transformation, which is primarily controlled by the diffusion of carbon in austenite (slow process). Some overlap between steps 1 and 2 can take place.
- 3) carbon homogenization in the structure.

2.2. Modeling

In the previous section a review on the experimental observations of ferrite-, pearlite- and pearlite/ferrite-to-austenite transformation was given. Besides the experimental studies, various scientific methods/models were developed to describe the transformation kinetics, each having different strengths and weaknesses [17-24]. A major motivation behind the modeling is that an accurate model provides information on the actual microstructural processes that cannot directly be obtained from the experiments.

Austenitization, as most of the solid state transformations, consists of two major steps: nucleation and growth. Before a model can be build several questions/assumptions have to be answered/adopted.

1. How the nucleation process will be modeled:
 - no nucleation;
 - instantaneous nucleation;
 - constant nucleation rate;
 - using *Classical Nucleation theory*.
2. How the growth part of the transformation will be modeled:
 - diffusion-controlled;
 - interface-controlled;
 - mixed-mode approach.
3. How the microstructure will be modeled:
 - no microstructural input;
 - schematic/simplified microstructure;
 - Voronoi assumption;
 - realistic microstructure.

In general, all models that are available in the literature are based on two major calculation methods, those based on the solution of a set of equations, so-called *Deterministic* models, and those that introduce stochastic variables into the calculation process, so-called *Probabilistic* models.

Deterministic models are based on the time-integration of a set of equations for a system consisting of a number of volume elements. At the end of calculation, the microstructure is described on the length scale of the features of interest, such as grain size or particle spacing *etc.* Roósz *et al.* [7] described the nucleation and growth during austenitization using Avrami's equation. This approach was used for isothermal conditions and later extended by Garcia de Andrés and Caballero [24] to non-isothermal conditions. The developed model includes the effects of nucleation and growth rates, which depend on the activation and interfacial energies, the overheating and structure parameters, such as the pearlite colony size and interlamellar spacing. A big disadvantage of this approach is that it requires an extensive experimental database and the visualization of the microstructure is not possible.

Another type of the deterministic models that were developed are based on the solution of the diffusion equation [19, 20]. These models assume that local equilibrium conditions are present at all interfaces and carbon diffusion in ferrite is ignored. The assumption of the local equilibrium condition implies that the transformation is a diffusion-controlled process, which might not necessarily be the case; and neglecting carbon diffusion in ferrite might lead to a misunderstanding of the kinetics of the transformation.

Probabilistic models were introduced to account for the stochastic character of the nucleation processes in the microstructure evolution. There are several well-known techniques, such as Monte Carlo (MC) [25, 26] and the Cellular Automata (CA) [26] techniques, which allow implementation of a probabilistic behavior based on a pre-defined set of rules. Probabilistic (stochastic) models use statistical or stochastic distributions for the nucleation features, taking into account the crystallographic anisotropy and preferential growth directions. Very few models in the literature use *Monte Carlo* simulation [18]. These models give a good qualitative representation of the microstructure, however in some cases suffer from numerical anisotropy, for example, a diffusion equation for an isotropic medium formulated with a cubic grid becomes orthotropic (diffusion along a diagonal does not occur at the same speed as along the axis of the grid).

During the last several decades the *Phase field* model became one of the most powerful methods for modeling many types of microstructure evolution processes. *Phase field* models can be combined with diffusion calculations, in order to incorporate both diffusion processes and the finite rate of the interface reaction, which avoids the assumption of the transformation being diffusion- or interface controlled. The model can in principle also incorporate the effects of anisotropic boundary energies and mobilities, and the effect of boundary plane orientation. A big advantage of the phase-field over other models is that it allows different morphologies to form, depending on the nucleation and growth conditions. A useful contribution to the above advantages is that in addition to modeling the kinetics of phase transformation, it can also generate characteristic microstructures, which represent potentially useful prototypes for the microstructures resulting from nucleation and growth processes in materials. Also, the phase field model can be linked with thermodynamic and kinetic databases, such as Thermo-Calc, Dictra, CALPHAD. Main disadvantages of phase field approach are first of all the assumption of the diffuse interface, which is not physical, and secondly, it is computationally very demanding.

So far, the phase-field model was applied to simulate grain growth [27-29], anisotropic grain growth [30], spinodal decomposition [31] and solidification [32-34]. A number of reviews appeared on this method [35, 36]. Application of the phase-field approach to model the metallurgical processes in steel was extensively studied in the European project VESPISM [37].

The phase field model was first introduced for modeling solidification of a pure melt to avoid tracking of a solid-liquid interface during solidification by replacing the sharp solid-liquid interface by using an artificial, continuous, non-conserved phase field, which describes a diffuse interface. Instead of defining a moving boundary condition at

the solid-liquid interface, the interface movement is described by the temporal evolution of this phase variable, which can vary between two extremes: usually 0 and 1 in the bulk regions; and changes continuously over a diffuse interface.

Many of the phase-fields models are based on the classical phase-field approach proposed by Wheeler, Boettinger and McFadden [33] for binary alloys. In this approach a continuous composition field is defined through the interface and the free energy density is extrapolated as a composition-weighted mixture of the free energy densities of the pure materials. A disadvantage of this approach is that the parameters depend on the interfacial thickness, which is usually significantly thicker than in reality.

Steinbach *et. al.* [38] proposed a multi-domain model with a different definition of the free energy density in the interface. In their model, the interfacial region is assumed to be a mixture of phases with different compositions, however constant in their concentration ratio. Besides the general advantage of being able to treat complex microstructures, the big advantages of the multi-domain model are:

- a) the *Classical Nucleation Theory* can be rather easily incorporated in the model. This gives a more realistic representation of the nucleation process.
- b) the interface mobility and the carbon diffusion are both incorporated in the model. This allows the different growth modes (diffusion-controlled, interface-controlled or mixed-mode) be reproduced within one formulation.

At the moment it is the most elaborate model that is available for modeling different microstructures and therefore will be used as a base tool to model the austenitization process. A more detailed description of the model and its adaptation to model ferrite/pearlite-to-austenite transformation will be given in the *Modeling* part of the thesis.

Summary

In this chapter, a review on the available experimental evidence on the formation of austenite from ferrite, pearlite and ferrite/pearlite initial microstructures is given (in section 2.1) together with the description of the models available to simulate the austenitization process (in section 2.2).

The kinetics of the austenite formation is largely determined by the initial microstructure and in particular by the phases present in it. If only ferrite phase is present, then the *ferrite-to-austenite* transformation is a very fast process and proceeds by a massive transformation mechanism. There is only a slight change in transformation kinetics with increasing heating rate and it is an interface-controlled process.

If the microstructure consists of a ferrite-pearlite mixture, the austenite formation process proceeds in two steps:

1. *Pearlite-to-austenite* transformation. This is a rather rapid process and proceeds within a narrow temperature range. The nucleation takes place at the pearlite-pearlite grain boundaries, where the crystal mismatch energy is maximum. The phase

transformation proceeds in the following way. After nucleation the transformation of pearlite/ferrite-to-austenite takes place. In a later stage, the cementite plates dissolve in this austenite and after a sufficiently long time a homogeneous austenite is formed. The growth of newly formed austenite regions is not planar and is faster if the interlamellar spacing is smaller. The kinetics is controlled by carbon diffusion (in austenite) and the effective diffusion distance, which is approximately equal to the interlamellar spacing.

2. *Ferrite-to-austenite* transformation. This is a much slower process compared to the pearlite-to-austenite transformation. It starts after a delay and is more strongly affected by the heating rate. Higher heating rates delay the transformation to higher temperatures. By the end of the transformation the formed austenite structure is not homogeneous in carbon content and some time is necessary for the diffusion processes to take place and homogenize the structure.

Phase-field modeling is a powerful tool that is capable to model phase transformations in steels. The phase-field approach offers a number of advantages. First of all, with the phase-field model it is possible to model the evolution of arbitrary morphologies and complex microstructures without tracking the position of the interfaces. Secondly, it can be applied to essentially all types of microstructures. Thirdly, a priori assumption on the transformation mode (diffusion-, interface- or mixed-mode) is not necessary. And finally, *Classical Nucleation Theory* can be incorporated to model the nucleation process.

References

- [1] D.P. Datta, A.M. Gokhale, *Metall. Trans. A*, 1981, vol. 12A, pp. 443-450.
- [2] C.R. Brooks: *Principles of The Austenitization of Steels*, Elsevier Applied Science, London, UK, 1992, pp. 81-144.
- [3] W. L. Haworth, J. G. Parr, *Trans. Amer. Society for Metals*, 1965, vol. 58, p.476.
- [4] G. R. Speich, A. Szirmai, *Trans. Metall. Society*, 1969, vol. 245, p. 1063-1074.
- [5] F.G. Caballero, C. Capdevila, C. Garcia de Andrés, *Mater. Sci. Tech.*, 2001, vol. 17, pp. 1114-1118.
- [6] R. F. Mehl, *Trans. Amer. Society for Metals*, 1941, vol. 29, p. 813.
- [7] A. Roósz, Z. Gácsi, E.G. Fuchs, *Acta Metall.*, 1983, vol. 31, no. 4, pp. 509-517.
- [8] C. Garcia de Andrés, F.G. Caballero, C. Capdevila, *Scripta Mater.*, 1998, vol. 38, no. 12, pp. 1835-1842.
- [9] L. E. Samuels, *Optical Microscopy of Carbon Steels*. American Society for Metals, Metals Park, OH, USA, 1980.
- [10] G. Molinder, *Acta Metall.*, 1956, vol. 4, pp. 565-571.
- [11] R. R. Judd, H. W. Paxton, *Trans. Metall. Society*, 1968, vol. 242, p. 206.
- [12] M. Hillert, K. Nilsson, L.E. Törndahl, *J. Iron Steel Inst.*, 1971, vol. 209, pp. 49-66.
- [13] F.G. Caballero, C. Capdevila, C. Garcia de Andrés, *Scripta Mater.*, 2000, vol. 42, pp. 1159-1165.

- [14] R.C. Dykhuizen, C.V. Robino, G.A. Knorovsky, *Metall. Mater. Trans. B*, 1999, vol. 30B, pp. 107-117.
- [15] E. Schmidt, Y. Wang, S. Sridhar, *Metall. Mater. Trans. A*, 2006, vol. 37A, pp. 1799-1810.
- [16] E. D. Schmidt, E. B. Damm, S. Sridhar, *Metall. Mater. Trans. A*, 2007, vol. 38A, pp. 244-260.
- [17] F.G. Caballero, C. Capdevila, C. Garcia de Andrés, *ISIJ Intern.*, 2001, vol. 41, pp. 1093-1102.
- [18] A. Jacot, M. Rappaz, *Acta Mater.*, 1999, vol. 47, pp. 1645-1651.
- [19] T. Akbay, R.C. Reed, C. Atkinson, *Acta Metall.*, 1994, vol. 42, pp. 1469.
- [20] C. Atkinson, T. Akbay, R.C. Reed, *Acta Metall.*, 1995, vol. 43, pp. 2013.
- [21] D. Gaude-Fugarolas, H.K.D.H. Bhadeshia, *J. Mater. Sci*, 2003, vol. 38, pp. 1195-1201.
- [22] L. Gavard, H.K.D.H. Bhadeshia, D.J.C. Mackay, S. Suzuki, *Mater. Sci and Techn.*, 1996, vol. 12, pp. 453-463.
- [23] C.A.L. Bailer-Jones, H.K.D.H. Bhadeshia, D.J.C. Mackay, *Mater. Sci and Techn.*, 2001, vol. 15, pp. 287-294.
- [24] C. Garcia de Andrés, F.G. Caballero, C. Capdevila, *Scripta Mater.*, 1998, vol. 39, no. 6, pp. 791-796.
- [25] M.P. Allen, D.J. Tildesley, *Computer Simulation of Liquids*, Oxford Science Publications, Oxford, 1996.
- [26] D. Raabe, *Computational Materials Science*, Wiley, New York, 1998.
- [27] D. Fan, L.Q. Chen, *Acta Mater.*, 1997, vol. 45, no.2, pp. 611-622.
- [28] C.E. Krill, L.Q. Chen, *Acta Mater.*, 2002, vol. 50, pp. 3057-3073.
- [29] B. Nestler, *J. of Crystal Growth*, 1999, vol. 204, no. 1-2, pp. 224-228.

- [30] A. Kazaryan, Y. Wang, S.A. Dregia, B.R. Patton, *Acta Mater.*, 2002, vol. 50, pp. 2491-2502.
- [31] D.J. Eyre, *Mathematics of microstructure evolution*, Ed. L.Q. Chen et al., *The Minerals, Metals and Materials Society*, 1996.
- [32] J.A. Warren, W.J. Boettinger, *Acta Metall. Mater.*, 1996, vol. 43, pp. 689-703.
- [33] A.A. Wheeler, W.J. Boettinger, G.B. Mc Fadden, *Phys. Rev. A*, 1992, vol. 45, pp. 7424-7439.
- [34] I. Loginova, G. Amberg, J. Ågren, *Acta Mater.*, 2001, vol. 49, no. 3, pp. 573-581.
- [35] L.Q. Chen, Y.Z. Wang, *JOM*, 1996, vol. 48, no.10, pp. 13-18.
- [36] L.Q. Chen, *Annual review of material science research*, 2002, vol. 32, pp. 113-140.
- [37] <http://cordis.europa.eu/>
- [38] I. Steinbach, F. Pezzolla, B. Nestler, M. Seeßelberg, R. Prieler, G.J. Schmitz, and J.L.L. Rezende, *Physica D*, 1996, vol. 94, pp. 135-47.

Chapter 3

Material and experimental techniques

Abstract

In this chapter, the material and the experimental techniques used in this study are described. A standard method that was for a long time used in determining the kinetics of transformation is optical microscopy. In spite of the great amount of work done using this technique [1-5], there are some drawbacks that prevent this method from being able accurately characterize the transformation (examples will be given later in this chapter). To overcome the difficulties associated with studying the austenitization process, it is desirable to use techniques that continuously measure the progress of the transformation. Among those, dilatometry is an alternative and possibly the most popular method in determining the overall transformation kinetics. A number of studies have been done using this technique [6-9]. While dilatometry is a very powerful and convenient method for studying the phase transformations, there are some cases when its applicability is limited. For example, the pro-eutectoid ferrite and pearlite simultaneously transform into austenite on heating, and the two processes are not easily distinguished by dilatometry. Another disadvantage of the dilatometric method is that it does not give information on the nucleation and growth rates. To overcome the challenges mentioned above a new technique was developed recently [10]: diffraction experiments with synchrotron radiation give *in-situ* information on both the fraction transformed and the number density of the grains.

3.1. Materials

The materials used in the current research are C22, C35, C45 and C60 alloys. The chemical compositions of the experimental alloys are shown in Table 3.1. Typical micrographs of the initial microstructures for the studied alloys are shown in Fig. 3.1. The microstructures consist of a ferrite and pearlite mixture with different phase volume fractions, given in Table 3.2.

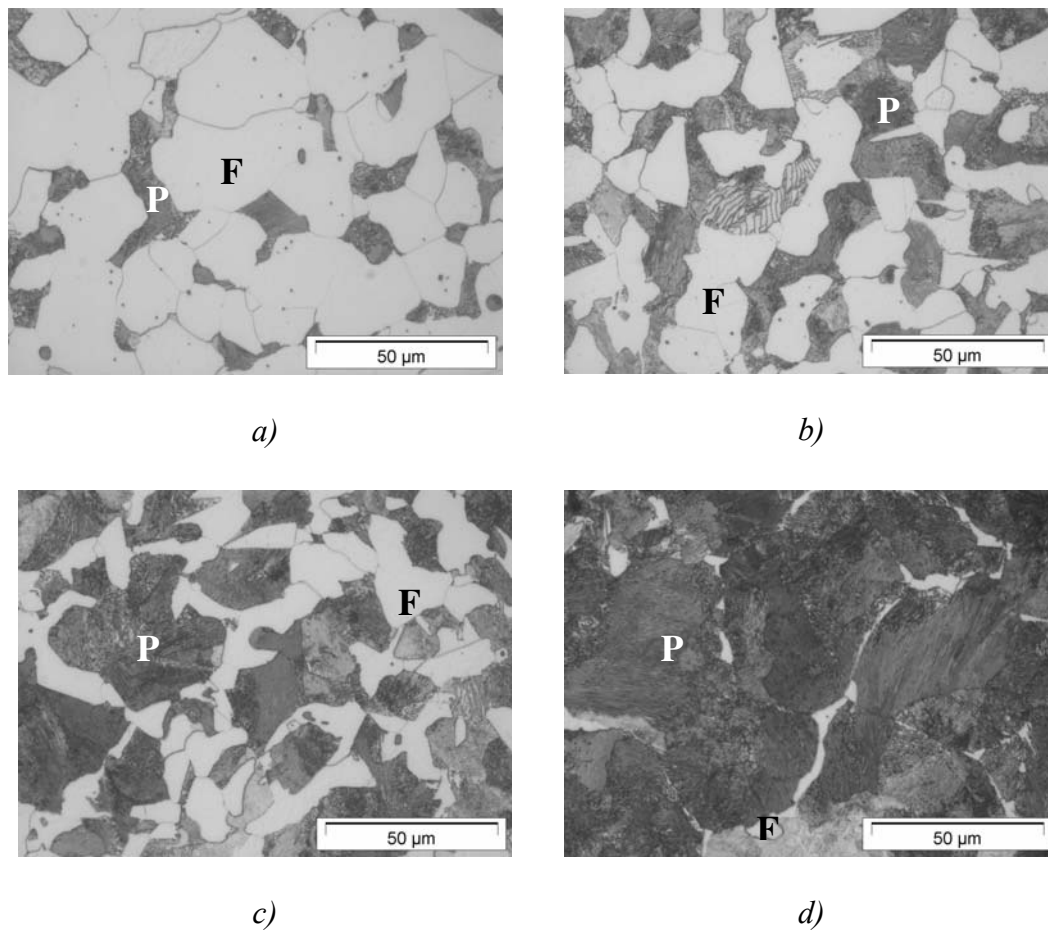


Figure 3.1. Optical micrographs of the initial microstructures for a) C22, b) C35, c) C45 and d) C60 alloys. F = ferrite (light) and P = pearlite (dark).

Table 3.1. Composition of the experimental alloys in weight percent.

Alloy	C	Mn	Si	Cu	Cr	Ni	Mo	Sn	P	S	Al
C22	0.214	0.513	0.200	0.086	0.021	0.049	0.003	0.003	0.019	0.031	-
C35	0.364	0.656	0.305	0.226	0.177	0.092	0.016	0.017	0.014	0.021	-
C45	0.468	0.715	0.257	0.231	0.193	0.144	0.017	0.013	0.002	0.031	-
C60	0.66	0.69	0.30	0.17	0.19	0.09	0.02	-	-	0.03	0.14

Table 3.2. Volume fractions of the phases in the initial microstructure.

Alloy	Ferrite, %	Pearlite, %
C22	79	21
C35	44	56
C45	32	68
C60	7	93

3.2. Experimental techniques

3.2.1. Optical and scanning electron microscopy (OM and SEM)

Optical microscopy [11] is the simplest method for studying the formation of austenite from different initial microstructures. It gives information over the general view of the microstructure and its morphology.

Samples for metallographic examinations were ground, polished and etched with a 2 % Nital cleaning agent. Using optical microscopy, the phases present in the sample were identified; the grain size and volume fraction of each phase were measured using a commercial image analysis package “Qwin” from Leica. In order to get statistically reliable data, measurements were performed in 5 randomly selected fields, $700 \times 550 \mu\text{m}^2$ each, for every sample. The disadvantage of this technique is the image resolution, which is limited to $0.2 \mu\text{m}$. So, to reveal the internal pearlite structure with optical microscopy is quite difficult. To overcome this difficulty, scanning electron microscopy was used. Electron microscopes [12], which use beams of electrons instead of light, are designed for very high magnification usage. In the

current study, the secondary-electron images were produced with a LEO 438VP scanning electron microscope fitted with a Tungsten filament. Samples for SEM measurements were first mechanically polished to 1 μm and then electrolytically polished using electrolyte that contained 400 ml 99 % 2-Bytoxyethanol with 20 ml HClO_4 .

3.2.2. Electron probe microanalysis (EPMA)

Electron probe microanalysis (EPMA) is an analytical tool used to non-destructively determine the chemical composition of small volumes of solid material [13]. It works similarly to an electron microscope, in which the sample is bombarded with an electron beam. In EPMA, however, the resulting X-ray radiation is analyzed (as opposed to the reflected electrons analyzed in EM).

In the current study, the composition profiles of the samples were determined using EPMA. On the cross-sections prepared of the samples, 0.5 μm equidistant points were selected along lines defined in backscattered electron images. The measurements were performed with a JEOL JXA 8900R wavelength-dispersive/energy-dispersive (WD/ED) combined micro-analyzer, operated with a focused electron beam of 15 keV and 25 nA. These electron beam conditions were an optimum between sufficient spatial resolution and intensity of C-K α radiation (the spot size was less than 0.2 μm). Wavelength Dispersive Spectrometry (WDS) was employed to record the C-K α , Si-K α , Cr-K α , Mn-K α , and Cu-K α intensities simultaneously. A W/Si X-ray reflective multilayer with a $2d$ -spacing of 9.80 nm was used for selecting the C-K α radiation, a (100)-TAP was used for selecting Si-K α , (002)-PET for Cr-K α and a (200)-LiF crystal for Mn-K α and Cu-K α radiation. The peak intensity for a single spot on the specimen was determined from measuring the number of counts during 4 minutes. The background intensities for C-K α , Si-K α , Cr-K α , Mn-K α , and Cu-K α were determined similarly at the same location. The background intensity of C-K α was measured separately on a pure α -Fe reference. The surface of the specimen was decontaminated 30 seconds prior to and during each measurement using an air-jet. This procedure removes any carbonaceous surface contamination at the measurement location. The composition at each analysis location of the sample was determined using the X-ray intensities of the constituent elements after background correction relative to the corresponding intensities of reference materials, i.e. $\theta\text{-Fe}_3\text{C}$ [14] for C and the pure elements for Si, Cr, Mn and Cu. The thus obtained intensity ratios were processed with a matrix correction program CITZAF based on the $\Phi(\rho z)$ -method [15]. Fe was taken as balance to compute the composition with the matrix element. The carbon concentrations determined are accurate within 0.03 wt. % including the background error [14].

3.2.3. Dilatometry

The applicability of dilatometry [9] in studying transformation kinetics is based on the changes of the volume of a sample during a phase transformation. During this transformation the lattice structure of the existing phases is changing, which is leading to a change in the specific volume. The values for the lattice parameters of ferrite, austenite and cementite are given in Table 3.3.

Table 3.3. *Lattice parameters of ferrite (α), orthorhombic cementite (θ) and austenite (γ) as a function of temperature T and the atomic fraction carbon ξ [9].*

Phase	Lattice parameters (Å)
α	$a_{\alpha}=2.8863 \times (1+17.5 \times 10^{-6} \text{ K}^{-1} \times \{T-800 \text{ K}\})$ for $800 \text{ K} < T < 1200 \text{ K}$
θ	$a_{\theta}=4.5234 \times (1+\{5.311 \times 10^{-6} - 1.942 \times 10^{-9} \text{ K}^{-1} \times T + 9.655 \times 10^{-12} \text{ K}^{-2} \times T^2\} \times m)$ $b_{\theta}=5.0883 \times (1+\{5.311 \times 10^{-6} - 1.942 \times 10^{-9} \text{ K}^{-1} \times T + 9.655 \times 10^{-12} \text{ K}^{-2} \times T^2\} \times m)$ $c_{\theta}=6.7426 \times (1+\{5.311 \times 10^{-6} - 1.942 \times 10^{-9} \text{ K}^{-1} \times T + 9.655 \times 10^{-12} \text{ K}^{-2} \times T^2\} \times m)$ where $m= \text{K}^{-1} \{T-293 \text{ K}\}$ for $300 \text{ K} < T < 1000 \text{ K}$
γ	$a_{\gamma}=(3.6306+0.78 \times \xi) \times (1+\{24.9-50 \times \xi\} \times 10^{-6} \text{ K}^{-1} \times \{T-1000 \text{ K}\})$ for $1000 \text{ K} < T < 1250 \text{ K}; 0.0005 < \xi < 0.0365$

For the dilatometric measurements cylindrical samples, 5 mm in diameter and 10 mm in length, were prepared. The samples were heated by a high-frequency induction coil with different heating rates (the detailed description of applied heating rates will be given in relevant chapters). A thermocouple, spot welded on the sample, was used to control the temperature during the tests. During the testing the samples were protected from oxidation by a vacuum of order of 10^{-5} mPa.

The dilatation signal from the dilatometric measurements was recalculated into austenite volume fraction curves as a function of temperature in two steps. In the first step, the lever rule method was used to obtain the pearlite+ferrite-to-austenite fractions curves. The thermal expansion was determined by extrapolation of the linear regions of the dilatometer curve as shown in Fig. 3.2.

The lever-rule based austenite fraction (f_L^{γ}) at a certain temperature is calculated as:

$$f_L^{\gamma} = \frac{L3 - L1}{L2 - L1} \quad (3.1)$$

where $(L1-L2=L)$ is the hypothetical total length change of the sample at a certain temperature, $L1$ the length of the sample with the ferrite+pearlite microstructure and $L2$ the length of a 100 % austenitic sample at the same temperature, and $L3$ is the actual length of the sample at that temperature.

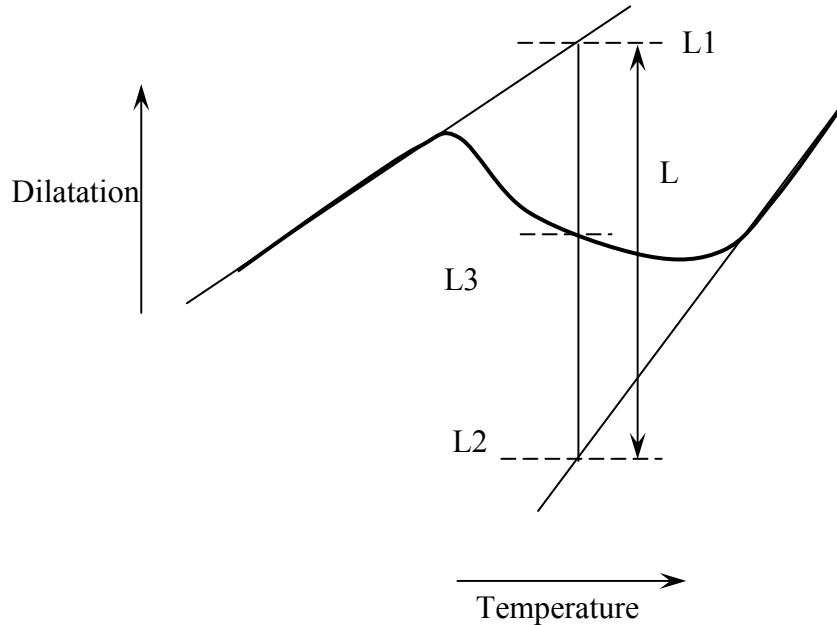


Figure 3.2. The scheme for the determination of the fraction transformed from a dilatometer signal using the lever rule method.

In the lever-rule method the fraction transformed is determined from the measured length change, without taking into account the differences between the specific volumes of different phases or the possible carbon enrichment of them. Errors of measurement result from the fact that more than one phase is involved in the transformation (the specific volume of ferrite is actually not equal to that of pearlite), and it is not taken into account that the dilatation (lattice parameter) of austenite is strongly dependent on its carbon content as well as on the temperature [9]. In reality, the pearlitic volume is much larger than the ferritic volume and so the effect of the pearlite-to-austenite transformation in the lever-rule approach is underestimated and the effect of ferrite-to-austenite transformation is overestimated (compare magnitudes a , measured, and b , equilibrium, in Fig. 3.3). This difference increases with decreasing carbon content in the alloy. To correct for this inconsistency, in the second analysis step, the estimated austenite transformation curves were recalculated using the information on the equilibrium austenite volume fraction development as obtained by MTDData[®] thermodynamic database. The transition point from pearlitic (steep) to

ferritic (gently sloping) part of the transformation curve from equilibrium calculations was taken as a reference point (see Fig. 3.3). On the next step, each point of the pearlitic part of the estimated transformation curve was shifted proportionally to the higher austenite volume fraction values according to Eq. (3.1a). In a similar way, each point on the ferritic part (gently sloping) was shifted proportionally to the higher values according to.

$$\text{for } T < T_R: \quad f^\gamma = f_L^\gamma \left(\frac{b}{a} \right), \quad (3.1a)$$

$$\text{for } T > T_R: \quad f^\gamma = 1 - (1 - b) \left(\frac{1 - f_L^\gamma}{1 - a} \right), \quad (3.1b)$$

where T_R is the reference temperature (see Fig. 3.3), a and b are the points on the austenite volume fraction curve, that indicate transition from steep (pearlite-to-austenite) to generally sloping (ferrite-to-austenite) part of the transformation (see Fig. 3.3).

In spite of some disadvantages and challenges in interpreting the data, dilatometry gives quick *in-situ* information about the overall transformation kinetics.

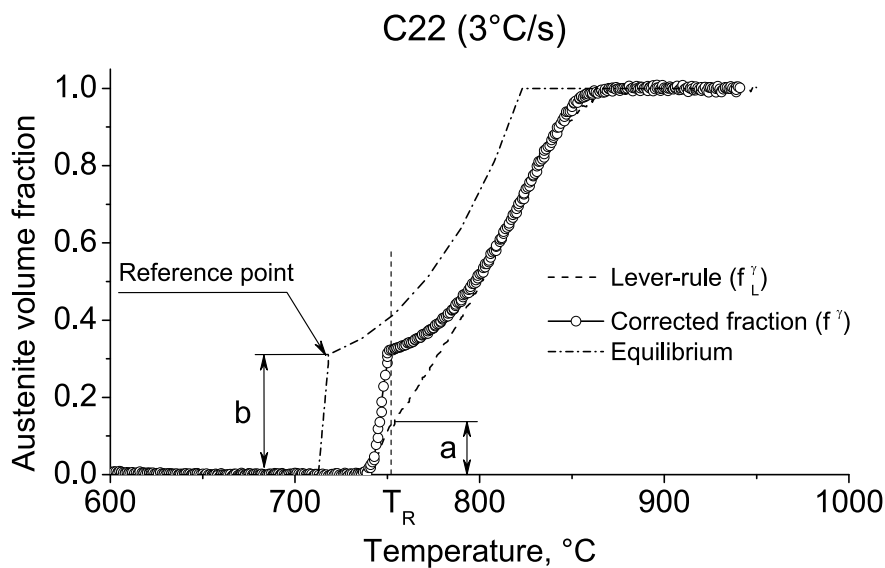


Figure 3.3. Example of the dilatometric-measurement correction of the austenite volume fraction curves as a function of temperature during continuous heating for C22 alloy at 3 °C/s heating rate. Measured data (solid triangles), corrected data (open circles) and equilibrium, as calculated with the thermo-dynamic databases (dash-dot). T_R is the reference temperature.

3.2.4. Three dimensional X-ray diffraction microscopy (3DXRD)

The three dimensional X-ray diffraction experiments described in this thesis were performed at beam line ID11 of the European Synchrotron Radiation Facility (ESRF) in Grenoble, France [10]. The schematic representation of the experimental set-up and a more detailed description can be found in [16]. In order to limit decarburization during the experiments, the samples were covered with a thin nickel coating and placed in a furnace with a helium flow. The samples were heated to 900 °C at a heating rate of 10 °C/min. In order to study the evolution of individual grains during the phase transformations, a small volume of the material was illuminated with a monochromatic beam of hard X-rays from the ESRF synchrotron source [16-18]. For this purpose the 3DXRD microscope is used in transmission geometry. The energy of the monochromatic X-rays is 80 keV (wavelength of 1.55×10^{-2} nm). The beam size is $63 \times 70 \mu\text{m}^2$ and the thickness of the samples is 400 μm for the C22 and 1 mm for the C35 samples. By rotating the sample around an axis perpendicular to the beam over an angle of 0.5° , a number of grains give rise to diffraction spots on a 2D-detector. The exposure time is 1 s. Studying the appearance and the change of intensity of these individual spots as a function of temperature during heating gives information about the austenite nucleation kinetics, the overall transformation behavior as well as the growth rates for individual grains. At the given experimental conditions the smallest radius of a detectable austenite grain is about 2 μm . Once every six exposures the beam size is expanded to $90 \times 90 \mu\text{m}^2$ in order to check if the total volume of the grain is illuminated. In order to check if the total integrated intensity from a specific grain is obtained by rotating the sample over a small angle $\Delta\omega_0$, additional exposures are taken during rotation over small angles of 0.5° just before and after the central rotation. The intensity of each individual spot is normalized with respect to the total intensity of the diffraction ring at the end of the transformation. By repeated acquisition of images the nucleation and growth of individual grains is studied with a typical resolution of a few seconds, or, equivalently, less than 1 K. The average austenite fraction during heating is obtained from the $\{200\}$ and $\{220\}$ powder rings obtained with the large beam size of $90 \times 90 \mu\text{m}^2$, in order to have better statistics. The nucleation data are derived by extrapolating the growth curves to the moment when nucleation takes place.

To determine the temperature during the experiments, a thermocouple was placed under the sample in close vicinity to it. This gave rise to a difference in the temperature of the sample and the temperature measured using the thermocouple. The measured start and end temperatures of the transformation (A_1 and A_3 temperatures respectively) were more than 100 °C lower than the equivalent temperatures from the para-equilibrium phase diagram calculated with MTDData[®]. In order to calibrate the temperature measurement obtained during the 3DXRD experiment, additional dilatometric measurements were made. The dilatometric samples, cut from the same materials, were heated with a 10 °C/min heating rate to 900 °C. On the basis of the dilatometry results the 3DXRD measurements were shifted in temperature, such that the start of the austenite formation measured by the dilatometer and using 3DXRD

microscope coincided. Even though a rather large difference between the measured thermocouple temperature and the sample temperature was present during the 3DXRD experiments, due to the quite small area that was illuminated during the experiments, the temperature gradient within the sample is not expected to be more than a few degrees.

References

- [1] G.R. Speich, A. Szirmae, *Trans. Metall. Society*, 1969, vol. 245, pp. 1063-1074.
- [2] R.R. Judd, H.W. Paxton, *Trans. Metall. Society*, 1968, vol. 242, p. 206.
- [3] A. Roósz, Z. Gácsi, E.G. Fuchs, *Acta Metall.*, 1983, vol. 31, no. 4, pp. 509-517.
- [4] D.P. Datta, A.M. Gokhale, *Metall. Trans. A*, 1981, vol. 12A, pp. 443-450.
- [5] G. Molinder, *Acta Metall.*, 1956, vol. 4, pp. 565-571.
- [6] C. Garcia de Andrés, F.G. Caballero, C. Capdevila, *Scripta Mater.*, 1998, vol. 39, no. 6, pp. 791-796.
- [7] F.G. Caballero, C. Capdevila, C. Garcia de Andrés, *Mater. Sci. and Tech.*, 2001, vol. 17, pp. 1114-1118.
- [8] C. Garcia de Andrés, F.G. Caballero, C. Capdevila, *Scripta Mater.*, 1998, vol. 38, no. 12, pp. 1835-1842.
- [9] T. A. Kop, *A dilatometric study of the austenite/ferrite interface mobility*, Ph.D. Thesis, TU Delft, the Netherlands, 2000, p.130.
- [10] H.F. Poulsen, *Three-dimensional X-ray diffraction microscopy: mapping polycrystals and their dynamics*, Springer, 2004, p. 156.
- [11] H.C. Sörby, *J. Iron Steel Ins. (London)*, 1886, pp. 140-144.
- [12] M. Knoll, E. Ruska, *Z. Phys.*, 1932, vol. 78, pp. 318-339
- [13] D.B. Wittry, *Electron Probe Microanalyzer*, US Patent No 2916621, Washington, DC: U.S. Patent and Trademark Office, 1958.
- [14] S. Saunders, P. Karduck, W.G. Sloof, *Microchim. Acta*, 2004, vol. 145, pp. 209-13.
- [15] J.T. Armstrong: in *Electron Probe Quantitation*, K.F.J. Heinrich and D.E. Newbury, eds., Plenum Press, New York, NY, 1991, pp. 261-315.
- [16] S.E. Offerman, N.H. van Dijk, J. Sietsma, E.M. Lauridsen, L. Margulies, S. Grigull, H.F. Poulsen, and S. van der Zwaag, *Nuclear Instruments and Methods in Physics Research*, 2006, vol. B246, pp.194-200.
- [17] S.E. Offerman, N.H. van Dijk, J. Sietsma, S. Grigull, E.M. Lauridsen, L. Margulies, H.F. Poulsen, M.Th. Rekveldt, and S. van der Zwaag, *Science*, 2002, vol. 298, pp. 1003-1005.
- [18] S.E. Offerman, N.H. van Dijk, J. Sietsma, E.M. Lauridsen, L. Margulies, S. Grigull, H. F. Poulsen, and S. van der Zwaag, *Acta Mater.*, 2004, vol. 52, pp. 4757-4766.

Chapter 4

Microstructural features of austenite formation in C35 and C45 alloys

V.I. Savran, Y. van Leeuwen, D.N. Hanlon, C. Kwakernaak, W.G. Sloof, J. Sietsma, *Metall. Mater. Trans. A*, 2007, vol. 38A, May, pp. 946-995.

Abstract

The microstructural evolution during continuous heating experiments has been studied using optical and scanning electron (SEM) microscopy and Electron probe microanalysis (EPMA). It is shown that the formation of the austenitic phase is possible in pearlite as well as in ferrite regions and a considerable overlap in time of ferrite-to-austenite and pearlite-to-austenite transformations is likely to be occurring.

Another observation that was made during the experiments is that depending on the heating rate, the pearlite-to-austenite transformation can proceed in either one or two steps. At low heating rates (0.05 °C/s) ferrite and cementite plates transform simultaneously. At higher heating rates (20 °C/s) it is a two-step process: first ferrite within pearlite grains transforms to austenite and then the dissolution of the cementite lamellae takes place.

Several types of growth morphologies were observed during the experiments. The formation of a finger-type austenite morphology was noticed only for low and intermediate heating rates (0.05 and 20 °C/s), but not for the heating rate of 300 °C/s. The formation of this finger-type austenite occurs on the pearlite-ferrite grain boundaries and coincides with the direction of cementite plates. The carbon inhomogeneities in the microstructure affect the formation of martensitic/bainitic structures on cooling.

4.1. Introduction

The major interest towards austenitization was drawn after Dual-Phase (DP) steels were developed. DP steels are most commonly used in structural applications where they have replaced more conventional High Strength Low Alloy (HSLA) steels. They were developed to provide high strength formable alloys and offered a significant weight reduction of the final products.

Speich *et al.* [1], who studied the intercritical annealing of DP steels, distinguished several stages in the ferrite-to-austenite transformation. According to ref. [1], the first step of ferrite-to-austenite transformation consists of the nucleation of austenite (γ) at the ferrite-pearlite interfaces and growth of austenite into pearlite ($\alpha+\theta$) until the pearlite dissolution is complete. The nucleation of austenite is argued to occur instantaneously, with essentially no nucleation barrier. The rate of growth in this stage is controlled primarily by the rate of carbon diffusion in austenite between adjacent pearlitic cementite (θ) lamellae, but may also be influenced by diffusion of substitutional elements at low temperatures [2]. At the end of this first step, a high-carbon austenite has been formed, which is not in equilibrium with ferrite (α). The second step of the transformation consists of the growth of this austenite into ferrite to achieve partial equilibrium with ferrite. The lower growth rate of austenite in this step is controlled either by the carbon diffusion in austenite over larger distances or by the manganese diffusion in ferrite. In the final step, very slow final equilibration of ferrite and austenite is achieved by manganese diffusion through austenite. Jayaswal and Gupta [3], who studied in detail the second and third stages of transformation in HSLA steel, observed that in addition to the growth of austenite from regions of prior pearlite, austenite was also observed to form at the α - α grain boundaries. They were not able to give explanations for this phenomenon, but indicated that the possible reason could be the presence of retained austenite in the starting microstructure. On the other side, Garcia de Andres *et al.* [4] in their study of the pearlite dissolution in Dual-Phase steel reported a clear differentiation between the pearlite dissolution process and the α - γ transformation.

An interesting observation that is often reported in relation to the ferrite-to-austenite transformation is the formation of acicular structures. Zel'dovich *et al.* [5] distinguished three different mechanisms of austenite formation depending on the heating rate. At a very low heating rate (a few degrees per minute) or at a very rapid heating (thousands degrees per second) newly formed austenite grains have an acicular structure, and a structural heredity (the original austenite grain is recovered both in size and crystallographic orientation) is present. It is said that the phenomenon of structural heredity must indicate an ordered mechanism of austenite formation, that is, diffusionless during rapid heating and what is known as the homogeneous mechanism of diffusional transformation during slow heating. Heating at a certain intermediate range results in loss of ordering and in grain refinement. The newly formed austenite grains have more of a rounded shape [5].

The formation of acicular structures during the ferrite-to-austenite transformation was also observed by Jayaswal and Gupta [3]. They noticed that the

austenite phase, instead of growing with a planar or nearly planar front, changed into a Widmanstätten structure on both the ferrite-ferrite grain boundaries and on well-advanced ferrite-pearlite (now austenite) interfaces. Law and Edmonds [6] performed studies of the morphology and crystallography of austenite precipitates in Fe-0.2%C-1%V alloy. They noticed that austenite formed on grain boundaries is idiomorphic or allotriomorphic, while that formed on lath boundaries can become acicular by inheriting the lath dimensions. Grain boundary austenite was proven to nucleate in low carbon ferrite with the Kurdjumow-Sachs orientation relationship with one ferrite grain, and to grow predominantly into an adjacent grain with which it was not related. Based on this observation and the general absence of planar facets or sideplate morphologies, they proposed that austenite grows by migration of incoherent interfaces.

This chapter presents experimental observations obtained during continuous heating experiments of C35 and C45 alloys, using optical and scanning electron (SEM) microscopy and Electron probe microanalysis (EPMA). The alloys were heated up with two different heating rates: 0.05 and 20 °C/s to different temperatures of the intercritical region and directly quenched. The effect of the extreme heating rates on the microstructure evolution was studied by heating the samples with 300 °C/s to different temperatures within and above the intercritical region. The results of experimental studies for different heating rates on the development of the microstructure during ferrite-to-austenite transformation focusing on austenite nucleation and growth morphologies are presented and analyzed in this paper. Experimental observations to support the idea of probable overlapping of pearlite-to-austenite and ferrite-to-austenite transformations as observed by Jayaswal and Gupta [3] are presented together with a possible explanation for this phenomenon.

4.2. Theoretical background

4.2.1. Driving force for nucleation in hypo-eutectoid steel

On heating a hypoeutectoid steel from room temperature to a single-phase region a phase transformation occurs, which consists of two stages, namely nucleation and growth. The essential driving force behind this transformation is the difference in the Gibbs free energy, ΔG , between the initial and final states [7]. For a transition from phase i to phase j to occur, the condition:

$$\Delta G = G^j - G^i < 0, \quad (4.1)$$

must be satisfied (G^i and G^j are the free energies of the parent and the new phase respectively).

A schematic representation of the Gibbs free energy G as a function of the carbon concentration is shown in Fig. 4.1a at a temperature above the eutectoid temperature of the Fe-C system. In this temperature range two phases: α (ferrite) with

composition $x_{\alpha\gamma}^{Ceq}$ (see also Fig. 4.1b point 1) and γ (austenite) with composition $x_{\gamma\alpha}^{Ceq}$ (point 2), are in equilibrium.

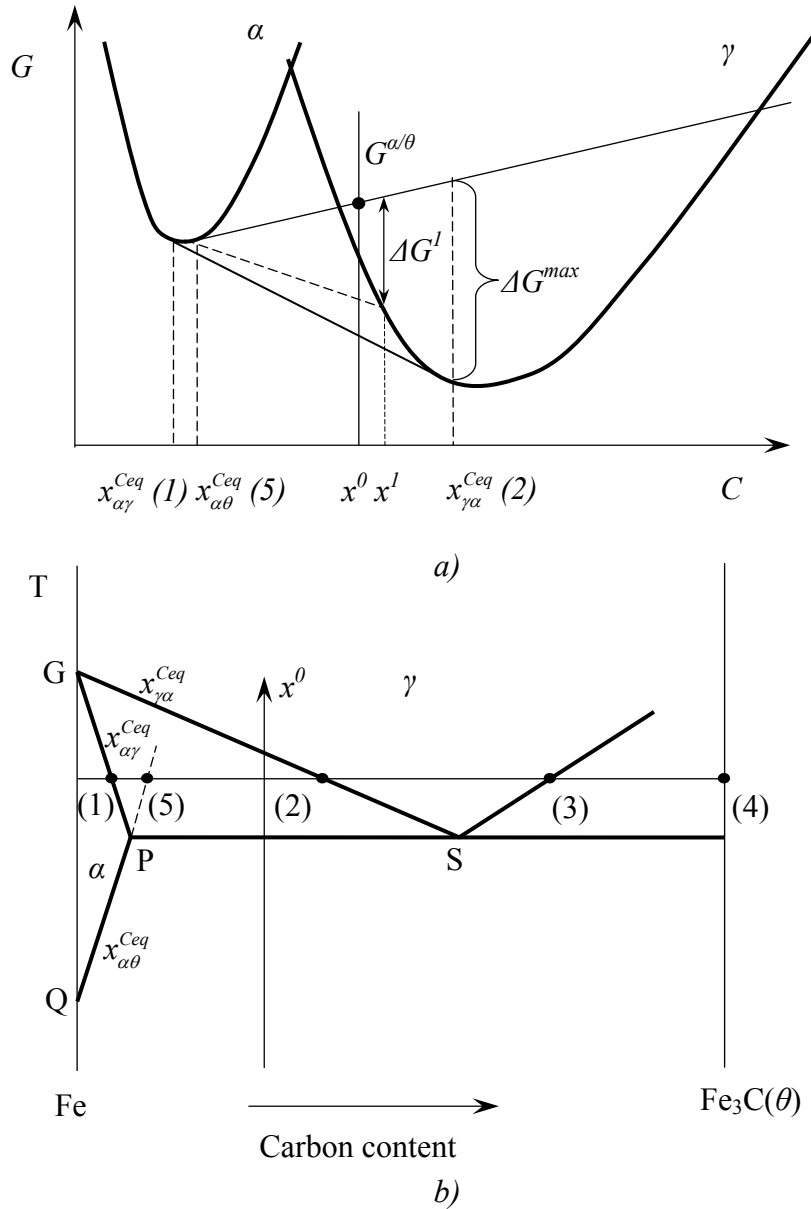
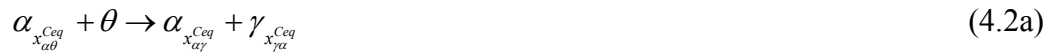


Figure 4.1. Schematic representation of the a) Gibbs free energy G as a function of the carbon concentration in ferrite (α), austenite (γ) and cementite (θ) at a temperature above A_1 and b) metastable Fe-C phase diagram, indicating notations for the carbon atomic fractions used throughout the text. Numbers in brackets correspond to figurative points (1)-(5) in Figs. 4.1, 4.2. The solid thin lines in Fig. 4.1a represent the common tangent lines between α - θ and α - γ .

The formation of the γ phase with the mentioned equilibrium composition leads to a maximum gain in Gibbs free energy (ΔG^{max}). In this case the newly formed austenite grains have a different composition from the original ferrite phase and a significant enrichment in carbon must take place. From Fig. 4.1a it also follows that even though the maximum gain in free energy is achieved for a large carbon enrichment of the γ phase (equilibrium condition), some decrease in the Gibbs free energy, even though of a smaller value, is also realized with the formation of the γ phase with lower carbon content (see for example ΔG^l , a situation in which the system departs from the thermodynamic equilibrium). Thus, even though with the formation of low-carbon austenite the gain in Gibbs free energy is smaller comparing to the equilibrium value ($\Delta G^l < \Delta G^{max}$), this process is nevertheless thermodynamically possible. By low-carbon austenite, the austenite with a carbon content less than equilibrium according to the phase diagram is understood, and not a carbon-free austenite. Some degree of enrichment does have to take place and the nucleation and growth will be stimulated in carbon-rich areas or in their vicinity.

4.2.2. Temperature range 1: $A_1 < T < A_3$

The changes in the microstructure of steel on heating can in part be understood in terms of the Fe-C phase diagram (see Fig. 4.1b). At room temperature and atmosphere pressure, the microstructure of carbon hypo-eutectoid steel after slow cooling consists of ferrite and pearlite. Upon heating the steel from room temperature to the A_3 temperature two different situations can be distinguished. The first one is related to the formation of austenite within the pearlite phase at the α/θ interface, as the one schematically represented in Fig. 4.2b, and is described as:



where $x_{\alpha\theta}^{Ceq}$ and $x_{\alpha\gamma}^{Ceq}$ are the equilibrium carbon concentrations in ferrite, changing with temperature according to lines QP and PG respectively (see Fig. 4.1b); $x_{\gamma\alpha}^{Ceq}$ is the equilibrium carbon concentration in austenite, changing according to line SG . θ is cementite and is considered to be of a constant composition.

It is known that the velocity of the phase boundary can be considered in first approximation inversely related to the carbon concentration difference on it [8]. For the value of this difference the concentration should change to form a new phase. The carbon difference on the α - γ grain boundaries is much less than on the γ - θ grain boundary, thus austenite can be expected to grow much faster in the ferrite phase than in the cementite phase.

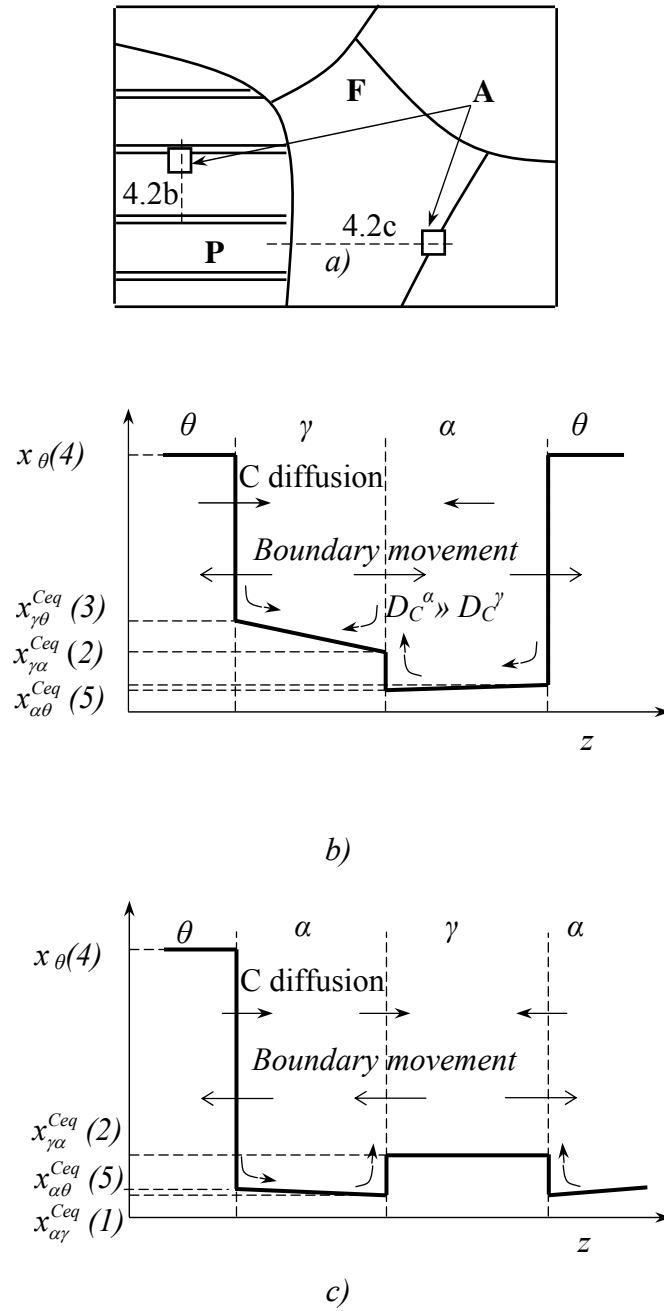


Figure 4.2. Schematic view of the microstructure (a) and variation of the carbon content across: (b) the cementite-austenite-ferrite and (c) the ferrite-austenite-ferrite boundaries. F = ferrite, A = austenite and P = pearlite.

Figure 4.2b is a 1D representation of the planar geometry. In this case the interface movement is controlled by the diffusion of carbon through the austenite phase. The situation at a triple line between cementite, ferrite and austenite is not considered as the diffusion distances become negligible and it will not be a limiting factor for the transformation.

The second situation is related to the possible formation of austenite on ferrite-ferrite grain boundaries, see Fig. 4.2c, and can be described as:



From the Fe-C phase diagram (as the one shown in Fig. 4.1b), it is seen that the maximum carbon concentration in ferrite decreases with increasing temperature. This will lead to austenite nucleation at the α - α grain boundaries. Thus, not only the carbon of cementite plays a role in the formation of austenite, but also the carbon rejected from the α -solid solution. On the other hand, due to the difference in carbon solubility at the α/θ and α/γ grain boundaries, a concentration gradient within the ferrite phase is present ($x_{\alpha\theta}^{Ceq} > x_{\alpha\gamma}^{Ceq}$, Fig. 4.2c). This creates the driving force for carbon diffusion towards the α - γ grain boundary. The subsequent growth of the austenite nuclei involves the removal of carbon from cementite with its diffusion into the not-transformed ferrite in order to “feed” carbon to austenite at the α/γ interface. The velocity of the α - γ grain boundary movement depends on how fast the carbon is supplied to it and consequently on the diffusion path length. This leads to the notion that ferrite within the pearlite will transform much faster than pro-eutectoid ferrite. Taking all the above-mentioned into account, it is possible to assume that the nucleation of austenite grains in pearlite and in pro-eutectoid ferrite can both occur, however the transformation will proceed at a much higher rate in the pearlite phase than in pro-eutectoid ferrite due to the shorter diffusion distances and the surplus of carbon that is available from the dissolving cementite plates.

4.2.3. Temperature range 2: $T > A_3$

The transformation that takes place at temperature $T > A_3$ can be described as:



where γ_{x^0} is the average carbon concentration in the alloy, and therefore also the austenite composition under equilibrium conditions after the transformation is completed (above A_3).

Upon further heating of the sample in the temperature range $A_1 < T < A_3$ the $\alpha \rightarrow \gamma$ transformation at conditions close to equilibrium proceeds most probably by

diffusional growth. The transformation completes above the A_3 temperature. In alloys with low carbon content and thus a low amount of pearlite present, nucleation on the ferrite-ferrite grain boundaries can take place. For the alloys with high pearlitic volume fractions, transformation proceeds via the growth from the already existing austenitic areas (mainly former pearlite grains) into pro-eutectoid ferrite.

4.3. Experimental procedure

In order to examine the evolution of the microstructure during continuous heating in C35 and C45 steels, a set of interrupted heating experiments was performed using a Bähr 805A/D dilatometer (a detailed description of the dilatometric measurements is given in chapter 3.2.3). Typical micrographs of the initial microstructures for C35 and C45 alloys are shown in Fig. 3.1. Chemical compositions of the experimental alloys are shown in Table 3.1. For the results that will be presented in this chapter, the differences in chemical compositions between studied alloys do not play a significant role.

The samples were heated with heating rates 0.05 and 20 °C/s to different temperatures within the ferrite+pearlite-to-austenite transformation region and directly quenched with cooling rates in the range of 700-750 °C/s. A detailed description of the sample preparation for metallographic studies using optical and scanning electron microscopes is given in chapter 3.2.1. The description of the EPMA analysis and sample preparation for it is given in chapter 3.2.2.

In order to study the effect of the extreme heating rate on the microstructure evolution, the samples were heated up with 300 °C/s heating rate to 770 °C, held at this temperature for 1, 10 and 60 s and to 900 °C for 1 s and quenched with gas with cooling rate app. 800 °C/s. In order to minimize the temperature gradients within the sample, a hole inside the cylindrical sample of C45 alloy of app. 3 mm in diameter was cut. The evolution of the microstructure was studied using optical microscopy as mentioned in chapter 3.2.2.

4.4. Results

4.4.1. Nucleation

Figures 4.3 and 4.4 show typical optical and SEM images from the interrupted heating experiments. In these down-quenched samples martensite islands reveal the locations of the austenite grains. Two interesting observations can be made. The first observation is related to the nucleation of the new austenite grains, which takes place predominantly in pearlite areas that are rich in carbon (see Fig. 4.3a, b). Depending on the heating rate this process can take place in one or two steps. At a very low heating rate, 0.05 °C/s, there is no essential delay between the ferrite-to-austenite transformation and the cementite dissolution within the pearlite grain. Figures 4.3a

and 4.4b show that no inhomogeneities are present in the martensite phase that was austenite prior to cooling.

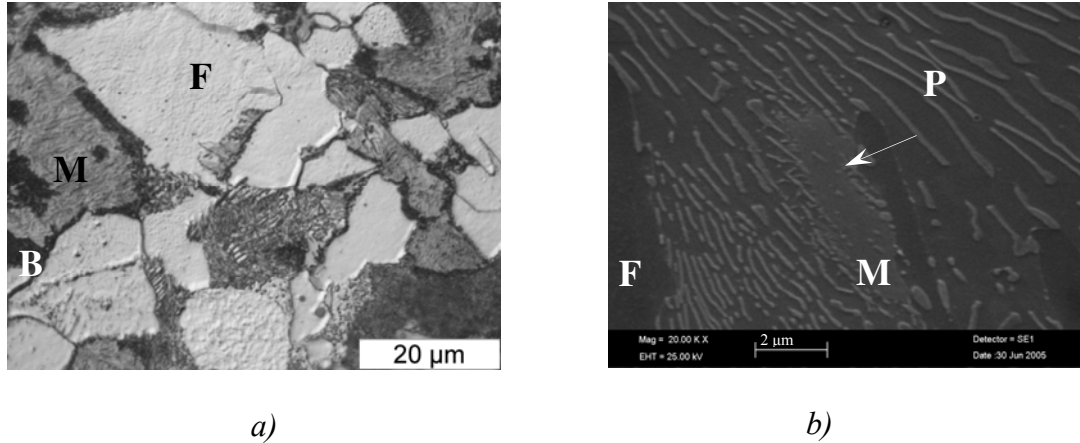


Figure 4.3. Typical micrographs from the interrupted heating experiments. a) Optical micrograph of the C35 alloy heated with the heating rate of 0.05 °C/s to 745 °C (close to the end of the pearlite-to-austenite transformation) and b) SEM micrograph of the C45 alloy heated with the heating rate of 20 °C/s to 765 °C (middle of the pearlite-to-austenite transformation). The arrow indicates the pearlite grain that was transformed into austenite on heating and subsequently into martensite on cooling. In this grain the cementite plates are still visible and in some cases partially dissolved. F = ferrite, M = martensite and P = pearlite.

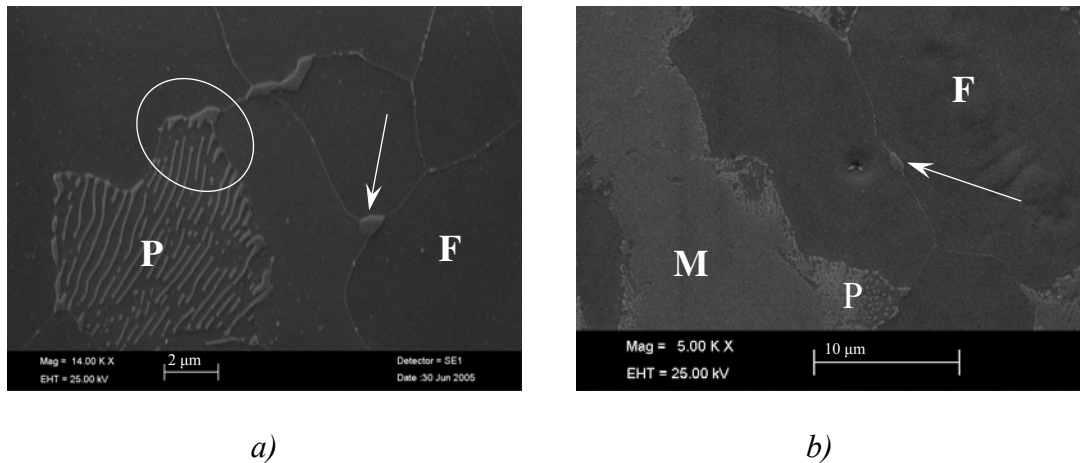


Figure 4.4. SEM micrographs of the C35 alloy, heated with 0.05 °C/s to: a) 740 °C (start of the pearlite-to-austenite transformation) and b) 745 °C (close to the end of the pearlite-to-austenite transformation). The arrows indicate the nucleation of austenite at the triple point (a) and the ferrite-ferrite grain boundary (b). F = ferrite, M = martensite and P = pearlite.

Figure 4.4a (see area marked with oval) shows an austenite grain nucleated on the ferrite-pearlite grain boundary. The growth of the newly formed austenite grain is not planar and the position of austenite “fingers” coincides with the direction and position of the cementite lamellae, which are rich in carbon.

A completely different situation was observed in the case when the heating rate was 20 °C/s. A clear delay in the cementite dissolution in comparison to the ferrite-to-austenite transformation resulted in a time-step difference between the two processes [4]. A closer look using SEM (see Fig. 4.3b) reveals a partially transformed pearlite grain in which the cementite is not completely dissolved in martensite, which was austenite at high temperatures prior to quenching.

The second interesting observation is related to the nucleation of austenite on the ferrite-ferrite grain boundaries: at a triple point (see arrow in Fig. 4.4a) and a grain boundary (see arrow in Fig. 4.4b). The austenite nuclei have a classical cup-like shape and appear at the very early stages of the transformation. Thus, two transformations, pearlite-to-austenite and ferrite-to-austenite, appear to overlap. The degree to which the two processes overlap cannot be established from the present experiments.

Figure 4.5 shows the distribution of the alloying elements across the austenite nuclei on the ferrite-ferrite grain boundary similar to the one shown in Fig. 4.4b. The carbon concentration across the austenite nucleus region varies significantly: from approximately 0.01 wt. % in the ferrite phase and up to 0.27 % in the austenite nucleus. Other alloying elements (Si, Cr, Mn, and Cu) do not show any significant variations in concentrations.

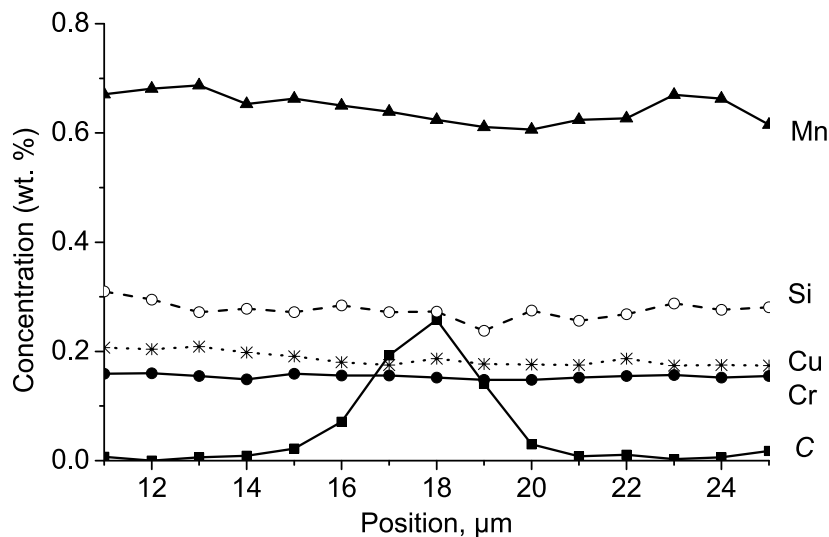


Figure 4.5. Alloying elements distribution across austenite nuclei formed on ferrite-ferrite grain boundary (C35 alloy). The maximum of the carbon concentration corresponds to the middle of austenite nuclei. The low level of the carbon concentration corresponds to the ferrite phase.

4.4.2. Growth morphologies

Several types of growth morphologies were observed during the experiments. Acicular (finger) type growth is spotted on the pearlite-ferrite grain boundaries (see Fig. 4.6). New austenite grains nucleate on the grain boundary and grow into the neighboring ferrite grain, most likely inheriting the lath dimensions. This type of growth is only detected on pearlite laths being perpendicular to the ferrite/pearlite grain boundary and is not present if the laths are parallel to it. In the latter case the formation of a bainitic structure on cooling takes place (see Figs. 4.6, 4.7). This bainite was austenite at higher temperatures prior to quenching. Bainite is clearly visible in the vicinity of former pearlite grains (martensite after quenching), is black in color and lies along the grain boundaries.

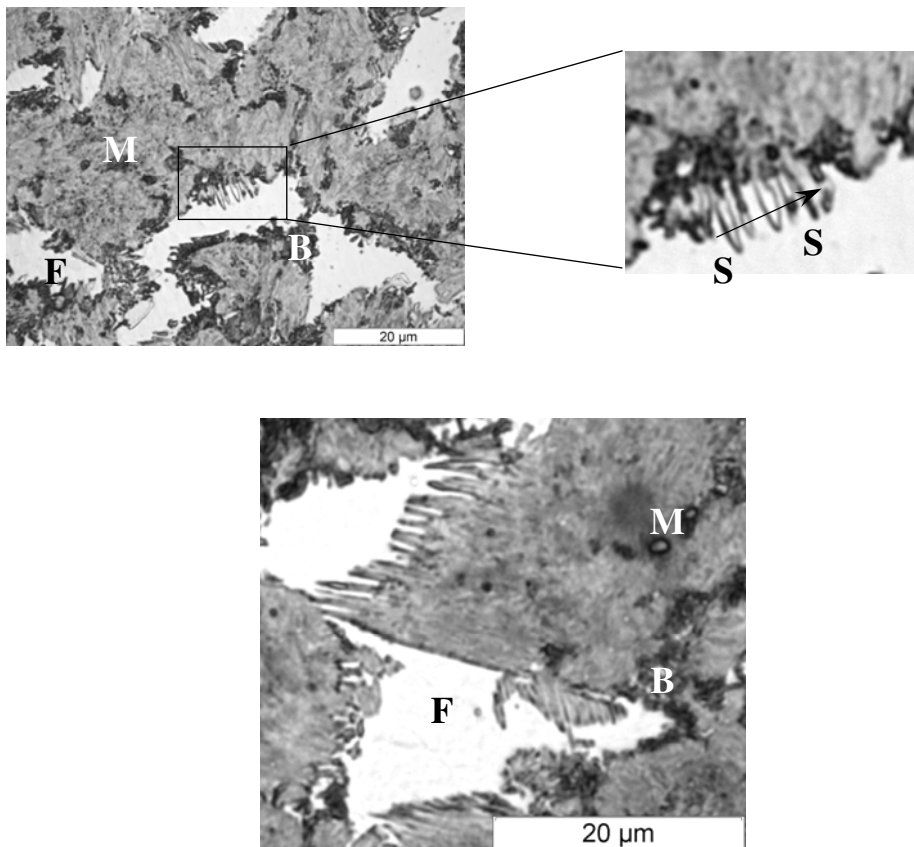


Figure 4.6. Examples of acicular growth morphologies as found in C35 and C45 alloys. The arrow (S-S) indicates the direction of EPMA measurement (see Fig. 4.8).

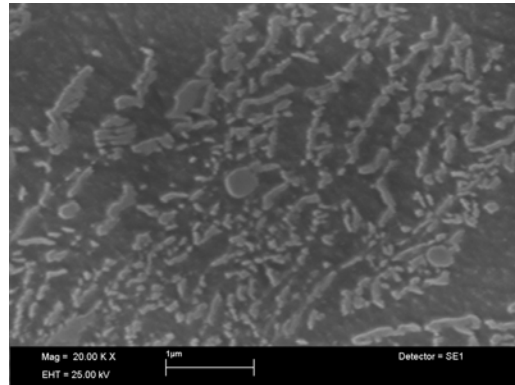


Figure 4.7. SEM micrograph of the bainite structure.

Figure 4.8 shows the distribution of the alloying elements across the fingers as determined by EPMA. Similar to Fig. 4.5, the only diffusing element is carbon, the other elements (Si, Cr, Mn, and Cu) show no or negligible variations in concentrations. The carbon content varies from app. 0.2 wt. % between the fingers till approximately 0.8 wt. % inside the finger.

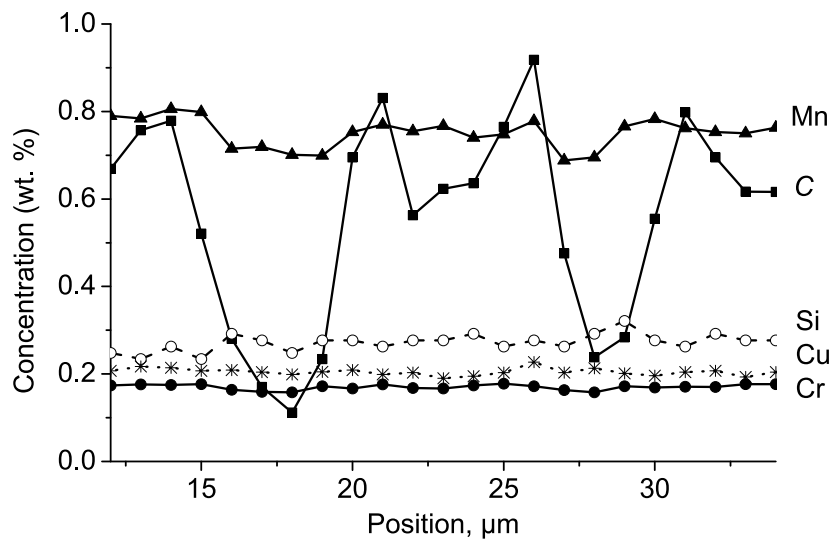


Figure 4.8. Alloying elements distribution across the “fingers” in C45 alloy (see Fig. 4.6). The maximum of the carbon concentration corresponds to the “fingers” and minimum between them.

The micrographs showing the effect of the extreme heating rate (300 °C/s) and different holding times on the microstructure evolution are shown in Fig. 4.9. At 770 °C and holding time 1 s the microstructure is highly inhomogeneous and consists of ferrite (white areas), bainite (black areas) and martensite matrix (grey areas). The black areas form a continuous network and reproduce the original grain size. The ferritic phase lies along these black lines, presumably the former grain boundaries.

Figure 4.10 shows the distribution of alloying elements along the line T-T (see Fig. 4.9a). Alloying elements (Si, Cr, Mn, and Cu) do not show significant variations in concentrations. In contrast, the carbon concentration in the black phase is remarkably low: around 0.2 wt. %. In the rest of the sample the carbon content is approximately 0.4 wt. %, which is about the average carbon content in the sample.

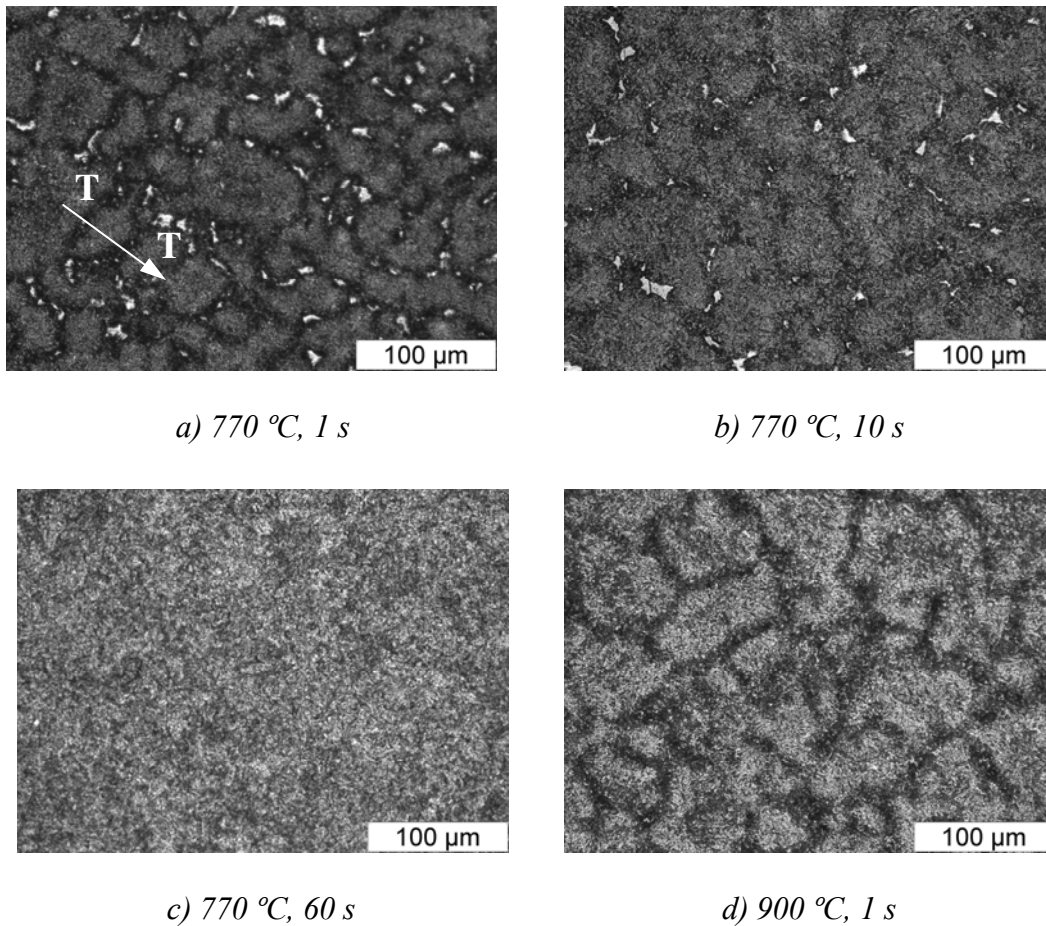


Figure 4.9. Typical micrographs from the interrupted heating experiments of the C45 alloy heated with 300 °C/s to a) 770 °C, 1 s; b) 770 °C, 10 s; c) 770 °C, 60 s; d) 900 °C, 1 s. The arrow (T-T) indicates the direction of EPMA measurement (see Fig. 4.10). Ferrite = white, Martensite = grey and Bainite = black.

With increasing the holding time to 10 s (Fig. 4.9b), the structure tends to become more homogeneous and the amount of ferritic phase first decreases and eventually almost disappears at holding time of 60 s (Fig. 4.9c). The temperature of 770 °C corresponds to the austenite area in the Fe-C phase diagram. At higher overheating (900 °C) and short holding time (1 s) the microstructure is as well highly inhomogeneous and consists of a martensitic matrix (grey areas) and bainite (black areas) forming a continuous network (Fig. 4.9d).

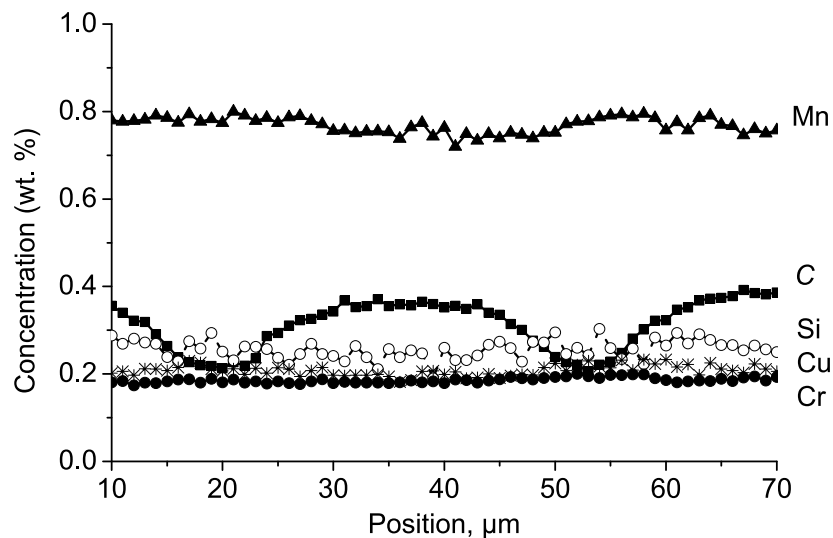


Figure 4.10. Alloying elements distribution along the line T-T in C45 alloy (see Fig. 4.9a). The minimum of the carbon concentration corresponds to the position of the black phase (bainite).

4.5. Discussion

It has been known for long that the situation during forming of austenite is much different from the transformation upon cooling. As the temperature is raised into the austenite region, the driving force for transformation increases (this is the difference in the free energy of the product, austenite, and the starting microstructure, such as pearlite or ferrite). Also, with increasing temperature the atomic mobility increases. Thus, the rate of austenite formation increases with increasing temperature. Since both the thermodynamic driving force for the formation of austenite and the atomic mobility become larger with higher temperatures, both the rate of nucleation and the rate of growth continually increase with increasing temperature.

4.5.1. Nucleation

Above the A_1 -temperature the ferrite+pearlite phase mixture, which was stable at lower temperatures, becomes unstable. The system will try to decrease its free energy by creating austenite, and consequently an austenite-ferrite interface is formed. The essential driving force behind this transition is the difference in the Gibbs free energy between the initial and final states. As was already shown in chapter 4.2, maximum gain in free energy is achieved for a large carbon enrichment of the γ phase. Some decrease in the Gibbs free energy, even though of a smaller value, is also possible with the formation of the γ phase with a lower than equilibrium carbon content (see for example ΔG_I in Fig 4.1a). In both cases nevertheless the nucleation and growth is stimulated in carbon-rich areas or their vicinity, as some enrichment of austenite phase has to take place. There are two possible sources of carbon. First of all these are the pearlitic areas, which have lamellar structures, consisting of alternating ferrite (low in carbon) and cementite (high in carbon) plates (see Fig. 4.2a, b). The second is the pro-eutectoid ferrite itself since $x_{\alpha\gamma}^{Ceq} (I) < x_{\alpha\theta}^{Ceq} (5)$ (see Fig. 4.2c). Hence, it follows that, for the austenitic nucleus formed on the boundary of ferrite grains, contact with cementite is not necessary. The decreasing equilibrium C-content with increasing temperature in the ferritic phase is in itself a direct source of carbon. After supplying carbon to austenite, ferrite is, in its turn, re-supplied with carbon by the dissolution of cementite plates, thus creating a constant driving force for the carbon diffusion towards the austenite-ferrite interface (see Fig. 4.2).

During the experiments both types of nucleation were observed for the 0.05 °C/s heating rate and only one type of nucleation (near the pearlitic areas) for the 20 °C/s heating rate. The EPMA measurements show a significant variation in carbon content in austenite nucleated on the ferrite-ferrite grain boundaries (about 0.27 wt. %, low-carbon austenite) and the one nucleated on pearlite-ferrite boundaries (around 0.8 wt. %, high-carbon austenite, which is close to the equilibrium value at temperature just above A_1). The possible presence of carbides on the ferrite-ferrite grain boundaries prior to transformation, which could stimulate the austenite nucleation, is doubtful. First of all, they were not observed in the initial microstructures and second, their presence on the ferrite-ferrite grain boundaries would lead to austenite nucleation on them for all heating rates, which was not the case. This observation indicates the importance of carbon diffusion during the transformation to the growing austenite phase. At the higher heating rates there is not enough time for carbon to diffuse so the austenite nucleation takes place only on the ferrite-pearlite boundaries, in the vicinity of the carbon source.

Obviously, the diffusion of carbon is not an infinitely fast process. The indication of the delay in cementite dissolution comparing to the austenite formation is clearly seen in Fig. 4.3b (see the grain indicated by an arrow). The pearlitic ferrite undergoes the transformation to austenite at higher temperatures and upon further quenching it transforms into martensite. At the same time the cementite plates are still visible within martensite. Similar observations were made by [9-12]. They noticed

that new grains of austenite grow along the plates of ferrite in a pearlite colony and expand to replace the ferrite in the colony. The cementite plates do dissolve in this austenite, but the austenite grains grow into ferrite at a faster rate than that at which the cementite plates dissolve. This residual cementite is eventually first thin, then spheroidizes and dissolves completely in austenite, depending on the carbon content and temperature. This points out the time difference between austenite formation and cementite dissolution. Thus the main difference between the pearlite formation on cooling and pearlite transformation on heating is that on cooling the ferrite and cementite plates grow together whereas on heating it is a two-step process and thus pearlite should be considered as consisting from two different phases – ferrite and cementite.

4.5.2. Growth morphologies

The carbon diffusion process, the rate of which increases with temperature, plays an important role in the occurrence of growth morphologies. As was indicated above, several types of growth morphologies were observed. The finger-type austenite growth morphologies (see Fig. 4.6) were spotted growing from the former pearlitic areas into neighboring proeutectoid ferrite grains. The average carbon concentration within the fingers is around 0.8 wt. % indicating that the fingers grow from the carbon-rich areas. Thus, it can be argued that the formation of the fingers coincides with the position of former cementite plates that were perpendicular to the grain boundary. After pearlite transformation to austenite is completed, the newly formed “pearlitic” austenite is inhomogeneous in composition, the carbon content being highest at the location of pre-existing cementite plates [9, 13]. Thus, the driving force at these grain boundaries is highly inhomogeneous. At low heating rates, which correspond to a low degree of overheating, the driving force for ferrite-to-austenite transformation is not high and it is energetically more favorable for austenite nuclei to grow with minimum surface energy. Minimal surface energy is secured by an orientation relationship between austenite and ferrite. In the case of finger-type growth the coherent broad sides should have a relatively low interfacial energy, whereas the incoherent tip would have a much higher interfacial energy. The presence of an orientation relationship between ferrite and austenite was shown by Law and Edmonds [6], who determined that the austenite was always within 15 ° of a Kurdjumow-Sachs orientation relationship:

$$(110)_{\text{bcc}} // (111)_{\text{fcc}}, [1\bar{1}1]_{\text{bcc}} // [0\bar{1}1]_{\text{fcc}}$$

For the bcc-fcc phase combination these are the only planes that are more or less identical in each crystal, and by choosing the correct orientation relationship it is possible for a low energy coherent or semicoherent interface to be formed. There are, however, no other sets of planes of good matching and the austenite plate is thus bounded by the incoherent interface. It is known that an incoherent interface has a

much higher mobility than a coherent one [14]. The incoherent interface will move as fast as diffusion allows and the growth will take place under diffusion-controlled mode. At the very fast heating rates, as the ones shown in Fig. 4.9, “fingers” of austenite were not formed. This can be explained by the lack of time for the diffusion to proceed because of the relatively high driving forces for ferrite-to-austenite transformation. In the places, where the cementite plate direction is not perpendicular to the grain boundary, the formation of a “black etching” structure on cooling was observed (see for example Figs. 4.6, 4.9). The EPMA measurements (see Fig. 4.10 and Fig. 4.9a line T-T) show that the black phase has lower carbon content (around 0.2 wt. %) comparing to the rest of the sample, which is around 0.4 wt. %, and is bainite (see Fig. 4.7). It is well known that steels with lower carbon content require higher cooling rates in order to obtain a martensitic structure. Thus in the structure with the carbon inhomogeneities, for the same cooling rate during the quenching of the sample it is possible to obtain martensite in the areas rich in carbon and bainite in the areas with lower carbon content. The formation of the “black” phase was noticed only on the former pearlite (which is austenite oversaturated with carbon) and proeutectoid ferrite (low in carbon) grain boundaries. Hence, the formation of bainite on cooling is possible.

4.6. Conclusions

1. Formation of the austenitic phase upon heating is possible in pearlite as well as in ferrite areas, however in the first one it proceeds at a much faster rate due to the shorter diffusion distances. The carbon content of the austenite nuclei formed on the ferrite-ferrite grain boundary is about 0.27 wt. %, which is much lower than the equilibrium value determined by the metastable phase diagram. A possible explanation is proposed based on thermodynamic considerations for the formation of low-carbon austenite (on the ferrite-ferrite grain boundaries) and high-carbon austenite (on the pearlite-ferrite grain boundaries).
2. Depending on the heating rate, the pearlite-to-austenite transformation can proceed in either one or two steps. At low heating rates (0.05 °C/s) the ferrite and cementite plates transform simultaneously. At higher heating rates (20 °C/s) a two-step process is observed: first ferrite within the pearlite grain transforms into austenite and then the dissolution of the cementite lamellae takes place.
3. Carbon inhomogeneities give rise to specific phenomena in the α/γ structure. The formation of finger-type austenite occurs on pearlite-ferrite grain boundaries and coincides with the position of cementite plates. In places where the direction of cementite lamellae is not perpendicular to the grain boundary, the formation of the “black” phase, which is believed to be bainite, takes place.

References

- [1] G.R. Speich, V.A. Demarest, R.L. Miller: *Metall. Trans. A*, 1981, vol. 12A, pp. 1419-28.
- [2] M. Hillert, K. Nilsson, L.E. Torndahl: *J. Iron Steel Inst. London*, 1971, vol. 209, pp. 49-66.
- [3] S.K. Jayaswal, S.P. Gupta: *Metallkd.*, 1992, vol. 83, pp.809-19.
- [4] C. Garcia de Andrés, F.G. Caballero, C. Capdevila: *Scripta Mater.*, 1998, vol. 38, no. 12, pp. 1835-42.
- [5] V.I. Zel'dovich, I.V. Khomskaya, O.S. Rinkevich: *The Physics of Metals and Metallography*, 1992, vol. 73, no. 3, pp. 250-65.
- [6] N.C. Law, D.V. Edmonds: *Metall. Mater. Trans. A*, 1980, vol. 11A, pp. 33-46.
- [7] J.W. Christian: *The theory of transformations in metals and alloys*, Amsterdam: Pergamon, 2002, 422-79.
- [8] I.I. Novikov: *Teoria termicheskoi obrabotki metallov {Theory of heat treatment of metals}*, Metallurgia, Moskow, 1986, pp. 154-62.
- [9] G.A. Roberts, R.F. Mehl, *Trans. of the ASM*, 1943, September, pp. 613-50.
- [10] G.R. Speich, A. Szirmae, M.J. Richards, *Trans. of Met. Soc. of AIME*, 1969, vol. 245, pp. 1063-1074.
- [11] C.R. Brooks: *Principles of The Austenitization of Steels*, Elsevier Applied Science, London, UK, 1992, pp. 81-144.
- [12] A. Jacot, M. Rappaz, R. C. Reed, *Acta Mater.*, 1998, vol. 46, pp. 3949-3962.
- [13] L. E. Samuels: *Optical Microscopy of Carbon Steels*, American Society for Metals, Metals Park, OH, USA, 1980, pp. 101-498.
- [14] D.A. Porter, K.E. Easterling: *Phase transformations in metals and alloys*, 2 nd ed., Nelson Thornes Ltd., Cheltenham, UK, 2001, pp. 171-80.

Chapter 5

Austenite nucleation and growth on the level of individual grains observed by 3DXRD microscopy

V.I. Savran, S.E. Offerman, J. Sietsma, *Metall. Mater. Trans. A*, (submitted)

Abstract

In this chapter austenite nucleation and growth during continuous heating was studied using three-dimensional X-ray diffraction (3DXRD) microscopy at beam line ID11 of the European Synchrotron Radiation Facility (ESRF) in Grenoble, France. Unique in-situ observations of austenite growth kinetics were made for two of the studied alloys: C22 and C35. The measured austenite volume fraction as a function of temperature shows a two-step behavior for both alloys: it starts with rather fast pearlite-to-austenite transformation, which is followed by a more gradual ferrite-to-austenite transformation. The austenite nucleus density exhibits similar behavior, with a sharp increase during the first stage of the transformation and a more gradual increase in nucleus density in the second stage for the C22 alloy. For the C35 alloy no new nuclei form during the second stage. Three different types of growth of austenite grains in the ferrite/pearlite matrix were observed. Together with the observed austenite nucleation behavior it gives detailed quantitative observations of the phase transformation kinetics during heating, i.e. austenite formation from ferrite and pearlite.

5.1. Introduction

As was already shown in the previous chapters, austenite formation from an initial microstructure of ferrite and pearlite consists, as most of the phase transformations, of two stages – *nucleation* and *growth*. Based on the previous work [1-4] it is possible to establish the sequence of events constituting the ferrite/pearlite-to-austenite phase transformation. Austenite nucleates first on the ferrite-pearlite grain boundaries and grows rapidly into the pearlite phase. Just above the A_1 temperature these austenite grains form with nearly the eutectoid carbon concentration, according to thermodynamic equilibrium. The formation of austenite on the ferrite-ferrite grain boundaries at the early stages of the transformation (when only pearlite is expected to transform to austenite) was described in chapter 4. In this case, austenite with a low carbon concentration compared to the equilibrium is formed. In the second stage of the phase transformation, when it is primarily ferrite that transforms to austenite, the transformation slows down. In both cases, the transformation of pearlite to austenite and of ferrite to austenite, the redistribution of carbon has to take place. There is however a distinct difference in the scale at which this takes place for the two transformations. Once the transformation of ferrite/pearlite-to-austenite is completed, carbon redistribution in austenite and austenite grain growth take place.

In this chapter the nucleation and growth of austenite from ferrite/pearlite structures is studied with the three-dimensional X-ray diffraction (3DXRD) microscope employing high-energy synchrotron radiation [5]. The advantage of this technique is that it offers the possibility of time-resolved measurements of the growth of individual austenite grains in the bulk of the material on a scale of micrometers at high temperatures, which is not possible with any other technique. The observation of individual grains provides a unique possibility of a quantitative in-situ measurement of the nucleation and growth rates in the bulk of the material.

5.2. Background

5.2.1. Nucleation

There are two main types of sites for austenite nucleation – near the areas rich in carbon, acting as a source of carbon (pearlite-pearlite and pearlite-ferrite grain boundaries or within the pearlite colonies) and away from them (on ferrite-ferrite grain boundaries). As was mentioned by several authors [6-9], in the areas rich in carbon, nucleation on the pearlite-pearlite and pearlite-ferrite grain boundaries is the most favored mechanism compared to nucleation on the ferrite-cementite interfaces within the pearlite grains. The interface energy is known to be a function of the lattice mismatch between two crystals, and high-angle boundaries favor nucleation. This appears to be the reason for the lack of nucleation on the ferrite-cementite interfaces within the pearlite colonies, which have a specific orientation relation and therefore are likely low-energy interfaces.

Among the two possible types of sites for austenite nucleation, the first type (pearlite-pearlite, pearlite-ferrite grain boundaries) comprises the most favorable places for austenite nucleation [1, 10, 11]. The presence of a high-carbon phase (pearlite) stimulates austenite nucleation, since a certain degree of enrichment of the austenite phase with respect to the ferrite phase has to take place to make the newly formed nucleus thermodynamically stable. In addition, the ferrite-pearlite interface will generally be a high-energy interface, and the ferrite-austenite interface can be a low-energy interface due to the possible specific orientation relations between ferrite and austenite. On the other hand, the presence of austenite nuclei on the ferrite-ferrite grain boundaries was observed in chapter 4. It was argued that the direct contact with a carbon-rich phase is advantageous, but not required for the formation of austenite nuclei. The decreasing equilibrium concentration of carbon in the ferritic phase with increasing temperature is in itself a source of carbon.

In the views on nucleation, the Classical Nucleation Theory (CNT) [12] is the most widely used approach to estimate the nucleation rate in terms of parameters like the activation energy for nucleation, ΔG^* , the Zeldovich non-equilibrium factor, Z , a frequency factor (the rate at which atoms are added to the sub-critical nucleus), β^* , and the density of available nucleation sites, N_n . It was widely used to describe the heterogeneous nucleation of ferrite grains in an austenite matrix [13-18]. The CNT predicts that the steady-state nucleation rate per unit of volume is given by:

$$\frac{dN_i}{dt} = (1 - f^\gamma) N_{n,i} Z_i \beta_i^* \cdot \exp\left[-\frac{\Delta G_i^*}{kT}\right], \quad (5.1)$$

where i indicates austenite nucleation from either pearlite or ferrite,

$(1 - f^\gamma)$ takes into account the decrease in the number of potential nucleation sites with increasing austenite volume fraction, with f^γ the austenite volume fraction;

N_n is the number of potential nucleation sites;

Z is the non-equilibrium Zeldovich factor. It takes into account the reduction in the equilibrium concentration of sub-critical nuclei due to the fact that some sub-critical nuclei become supercritical during the nucleation. In our analysis we assume Z to be constant.

T is the temperature;

k is the Boltzmann constant;

β^* is the frequency factor, expressing the rate at which single atoms are added to the critical nucleus, which is given by [19]:

$$\beta^* = \frac{6S^*}{a^4} D_0 \exp\left(-\frac{Q}{kT}\right), \quad (5.2)$$

where D_0 is the pre-exponential factor of the diffusion constant;

Q is the activation energy for atom transfer across the nucleus-matrix interface. It is approximated by the activation energy for diffusion of iron atoms in ferrite and is taken to be 3.93×10^{-19} J [20];

S^* is the area of the nucleus which can accept atoms.

a is the average lattice parameter of ferrite.

ΔG^* is the activation energy for nucleation. In general, it can be written as [13]:

$$\Delta G_i^* = \frac{\psi_i}{\Delta g_V^2}, \quad (5.3)$$

where ψ contains all the information about the shape of the nucleus (geometrical factors) and the energies, σ_i , of the interfaces that are involved in the nucleation process, i.e. the newly formed interfaces and matrix interfaces where the nucleation took place;

Δg_V is the difference in Gibbs free energy per unit volume between parent and forming phase (driving force for nucleation).

Among all the variables used to calculate the nucleation rate, the ψ -parameter is the most difficult to establish. This parameter contains the information on the shape of the critical nucleus as well as the interfacial energies; parameters that are difficult or even impossible to measure experimentally even with the modern techniques. Nevertheless, there have been several theoretical and experimental attempts to estimate them. Clemm and Fisher [21] proposed a model for the grain-corner nucleation of a nucleus that has an incoherent interface with the parent phase. In this model four spherical caps form the nucleus at a grain corner and grow simultaneously into four parent grains. The ψ value related to this type of grain-corner nucleation with incoherent phase boundaries between the nucleus and the matrix is predicted to be 3.3×10^{-3} J³/m⁶, with values for the interface energy taken from the literature. Another model, which was used by Lange *et al.* [18], assumes that ferrite nuclei mainly form on a grain face. In this case, the nucleus forms with coherent and partially coherent interfaces and thus requires smaller activation energy for nucleation. The ψ value found by Lange *et al.* for ferrite nucleation on austenite/austenite grain boundaries is 2.1×10^{-6} J³/m⁶, based on their experimentally deduced values for the energy of the interfaces involved in the nucleation process. In a recent study on ferrite nucleation in an austenite matrix performed by Offerman *et al.* [13], the value for ψ is experimentally found to be 5×10^{-8} J³/m⁶, which is much lower than the previously found model values. The underlying reason might be found in the formation of a nucleus that has a specific orientation relationship with one of the parent grains and that has nucleated at a grain corner, since Huang and Hillert [22] experimentally found that grain corners are the most effective places for nucleation in carbon steels. It should be noted that in the experiment of Offerman *et al.* the position of the ferrite nuclei was not determined, but the experimental results show that one

ferrite grain forms for each austenite grain, which suggests that the ferrite nuclei are likely appeared at austenite grain corners. According to van Dijk *et al.* [16], the steady-state assumption for the CNT holds only for certain conditions. An important criterion that has to be fulfilled is that the energy barrier for nucleation, ΔG^* , is larger than the kinetic energy of the atoms, kT . In case the activation energy for nucleation is smaller than kT , but larger than zero, the cluster size distribution of the sub-critical nuclei and the resulting nucleation rate are intrinsically time-dependent. The nucleation rate should then be described by the basics of the nucleation theorem, i.e. the cluster dynamics (CD). One of the important differences between the situation that ΔG^* is larger than kT (classical approach) and the situation that $0 < \Delta G^* < kT$ is in the values for n^* (the amount of atoms in a critical nucleus) and n^+ (the amount of atoms in a super-critical nucleus, i.e. a nucleus that is stable with respect to thermal re-dissolution). In the CNT the relative difference between n^* and n^+ is negligible, but in the case that $0 < \Delta G^* < kT$, the difference between n^* and n^+ can be large.

5.2.2. Growth

Once the austenite nucleus is formed on a pearlite-ferrite grain boundary, it starts to grow relatively rapidly into the pearlite grain. Pearlite is a phase that consists of two interpenetrating single crystals of ferrite and cementite (Fe_3C) that are locally ordered as alternating plates. Due to the peculiarity of its morphology (a high density of surface area) and the high carbon content the driving force for transformation into austenite is relatively large. Following Gaude-Fugarolas and Bhadeshia [23] it is possible to estimate the average velocity of the austenite interface within the pearlite colony under diffusion-controlled growth, assuming that the growth rate is determined by the diffusion of carbon in austenite. At 740 °C for Mn steel the para-equilibrium carbon concentrations in austenite on the austenite-cementite and the austenite-ferrite interfaces are $x_{\gamma\theta}^{Ceq} = 0.76$ wt.% and $x_{\gamma\alpha}^{Ceq} = 0.65$ wt% respectively; whereas the para-equilibrium carbon concentration in ferrite on the ferrite-austenite interface is $x_{\alpha\gamma}^{Ceq} = 0.011$ wt. %. The diffusivity of carbon in austenite is $D_\gamma = 6.24 \cdot 10^{-13}$ m²/s [24]. For a typical value of the interlamellar spacing in pearlite $L = 0.5$ μm, the growth rate is estimated to be 1.4 μm/s.

The other possible type of nucleation site, as was already mentioned earlier, is formed by the ferrite-ferrite grain boundaries. In this case there is no direct contact with the source of carbon, the pearlite phase, so during growth carbon will be supplied from areas that are rich in carbon (for instance austenite formed from pearlite) through the ferrite matrix (see Fig. 5.1). Under the assumption that the growth is controlled by the diffusion of carbon in ferrite, the flux of carbon atoms can be expressed as:

$$J^\alpha = -D_{C\alpha} \cdot \left(\frac{x_{\alpha\gamma'}^{Ceq} - x_{\alpha\gamma}^{Ceq}}{z_{\gamma\alpha}} \right) \quad (5.4)$$

where $D_{C\alpha}$ is the temperature dependent carbon diffusion coefficient in ferrite [25];

$x_{\alpha\gamma'}^C$ is the carbon concentration in ferrite on the grain boundary of ferrite with carbon-rich austenite (austenite formed in pearlite regions);

$z_{\gamma\alpha}$ is the position of the austenite-ferrite interface and is equal to the carbon diffusion distance from the source of carbon (former pearlite phase) to the austenite nucleus. For the estimation of the typical growth rate a value of 30 μm is taken.

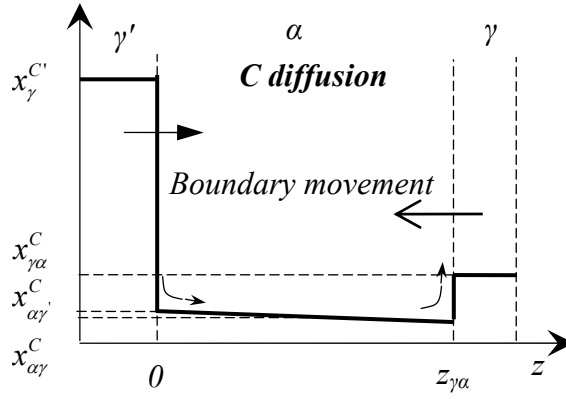


Figure 5.1. Variation of the carbon content across the austenite-ferrite boundary. α = ferrite, γ = austenite formed on ferrite-ferrite grain boundary, γ' = carbon-rich austenite formed in pearlite regions.

The interface movement for the austenite grain growth on the ferrite-ferrite grain boundary can then be calculated as:

$$\frac{dz_{\gamma\alpha}}{dt} = - \frac{J^\alpha}{(x_{\gamma\alpha}^{Ceq} - x_{\alpha\gamma}^{Ceq})} \quad (5.5)$$

Taking the average diffusion distance equal to 30 μm and solving Eqs. (5.4, 5.5), it is possible to estimate the austenite-ferrite interface velocity. The average velocity of the austenite-ferrite interface for C22 alloy at 750 $^\circ\text{C}$ is expected to be 0.03 $\mu\text{m/s}$.

5.3. Results and discussion

5.3.1. Volume fraction

Figure 5.2a, b shows the measured austenite volume fractions for the C22 and C35 alloys as a function of temperature compared to the para-equilibrium fractions as obtained from MTData[®]. There are remarkable similarities in the curves of Fig. 5.2.

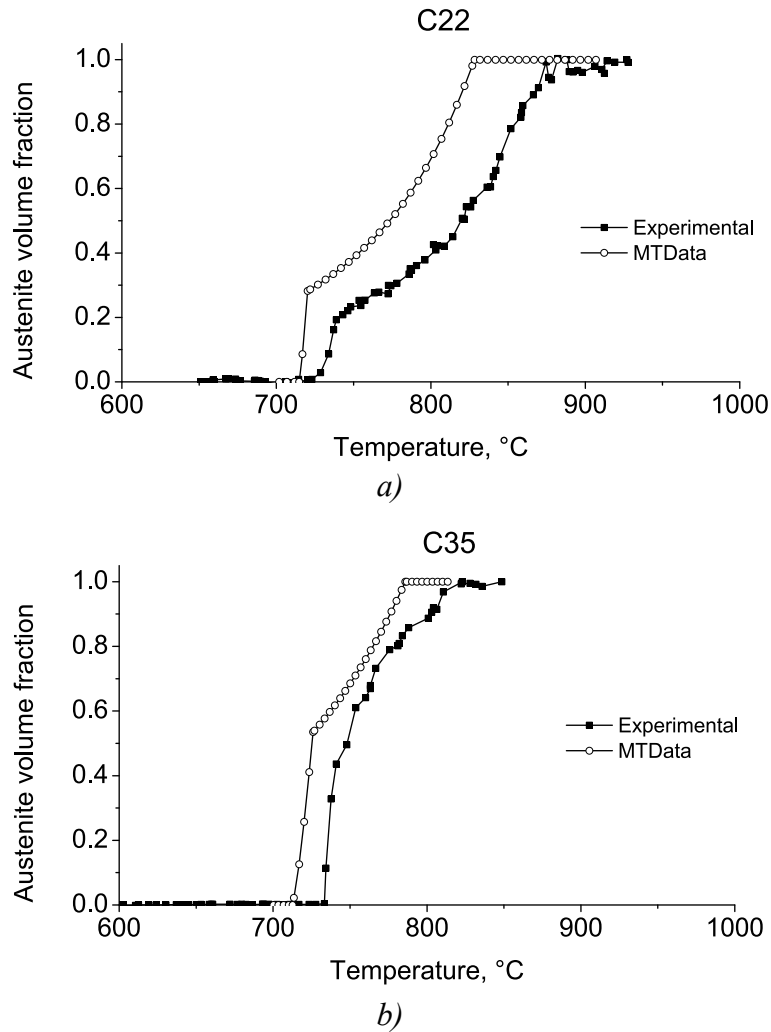


Figure 5.2. Austenite volume fraction as measured by 3DXRD (solid rectangles) and calculated using MTData[®] (open circles) for a) C22 and b) C35 alloys.

All curves initially display a fast increase in austenite fraction, which corresponds to the pearlite-to-austenite transformation, as was observed earlier [1, 2,

11]. It is then followed by a slower increase in austenite fraction, corresponding to the ferrite-to-austenite transformation. It is seen that the transition coincides with the austenite fraction as calculated by MTDData[®].

From Fig. 5.2 it can also be seen that the formation of austenite starts around 15°C higher for the C22 alloy and around 20°C higher for the C35 alloy compared to the A_1 temperature as calculated with MTDData[®]. This overheating can be due to two causes. First, it is necessary to keep in mind that there is an uncertainty in the measured start temperature (the austenite volume fraction curve that was measured using the 3DXRD microscope was shifted to a higher temperature to coincide with the start of the austenite formation as determined using dilatometry, see section 3.2.4). Dilatometry is a technique that measures the relative length change of the sample with respect to the temperature. A few percent of austenite has to be formed first in order to give rise to a signal on the dilatation curve.

On the other hand, the observed overheating can, to some extent, be explained by the incubation (or induction) time for nucleation. As was described by Kashchiev [26] after the initial supersaturation of the old phase, some time, called induction time, may elapse prior to the formation of an appreciable amount of the new phase. This time is experimentally observable. The different experimental techniques detect the first formation of the new phase with a different resolution. In the present case, as was mentioned earlier, the detection limit of 3DXRD microscopy is 2 μm . From the growth rate of the austenite nuclei in the initial stage (which is approximately 0.03 $\mu\text{m/s}$ as will be described later in section 5.3.3) the estimated time for the nuclei to be detected is approximately 70 s. For the given heating conditions (heating rate is 10°C/s) this will lead to a delay of about 12 °C.

5.3.2. Nucleation

Figure 5.3 shows the measured nucleus density for C22 and C35 alloys as a function of temperature during continuous heating to the one-phase austenite region. The number of nuclei is determined from the number of austenite spots on the 2D detector and is taken as an accumulative number. A more detailed description of the procedure can be found in [14]. Two different stages in the nucleation behavior are observed. Just after the beginning of the pearlite/ferrite-to-austenite transformation, there is a very fast increase in the number of austenite grains. Pearlite-ferrite (or pearlite-pearlite) grain boundaries are the most favorable places for the austenite nucleation for two reasons: the presence of the incoherent high-energy interface stimulates the heterogeneous nucleation, and the availability of carbon makes the newly formed nuclei stable. The nucleus density also depends on the number of potential nucleation sites. This is related to the density of the pearlite-pearlite or pearlite-ferrite grain boundary area and the shape and size of the grains. Taking into account that both studied alloys have approximately the same average grain size, for the C22 alloy the average pearlite volume fraction is lower than for the C35 alloy. Thus, even though both alloys feature a very sharp increase in the nucleus density in the initial stage of

the transformation, the C35 alloy in total has a higher nucleus density in comparison to the C22 alloy.

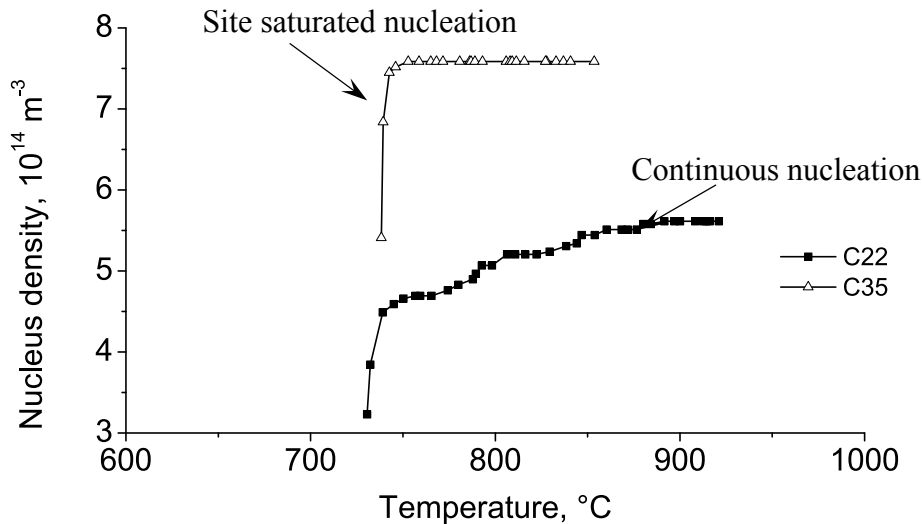


Figure 5.3. Austenite nucleus density as the function of temperature for C22 (solid rectangles) and C35 (open triangles) alloys.

After the first stage of very sharp increase, which is related to the nucleation at the pearlite-ferrite or pearlite-pearlite grain boundaries, in the second stage of the transformation, when nucleation at the ferrite-ferrite grain boundaries takes place, the nucleus density continues to increase more gradually for the C22 alloy. About 25% of the nuclei are formed in this range. For the C35 alloy no new nuclei appear to form, so the transformation proceeds further via the growth of already existing austenite grains into pro-eutectoid ferrite.

In order to apply Eqs. (5.1-5.3) to the experimental data and to characterize the nucleation behavior by the ψ value, the fraction of austenite nuclei formed on the ferrite-ferrite grain boundaries is taken from the measured data (see Fig. 5.4). This is only done for the C22 alloys, since the experimental data for nucleation on the ferrite grain boundaries in the C35 alloy is not enough to perform further analysis. The driving force for nucleation is calculated using MTDData[®] thermodynamic database. It is determined through the parallel-tangent construction under the assumption of the para-equilibrium condition (only carbon is considered to redistribute). The driving force for nucleation, Δg_V , which is the change in Gibbs free energy due to the formation of an austenite nucleus in the ferrite matrix, is not trivial to find. The major challenge here is that the exact carbon content of the parent transforming phase (ferrite) at the interface is not known. The equilibrium phase diagram gives only the average carbon content in ferrite in equilibrium with austenite. If two phases (like

ferrite and austenite) both have equilibrium carbon values there is no driving force for the transformation. In our analysis we assume that the transforming ferrite phase has the equilibrium concentration of carbon in ferrite at the eutectoid temperature and that it does not change during the transformation. This is a reasonable assumption since the change in the carbon concentration in ferrite is rather small during the whole transformation range. Although the resulting value for ψ can be affected by this choice, the direct influence of the choice for the carbon concentration in ferrite on ΔG^* is very small. The austenite fraction is determined from the 3DXRD measurements, as shown in Fig. 5.2a.

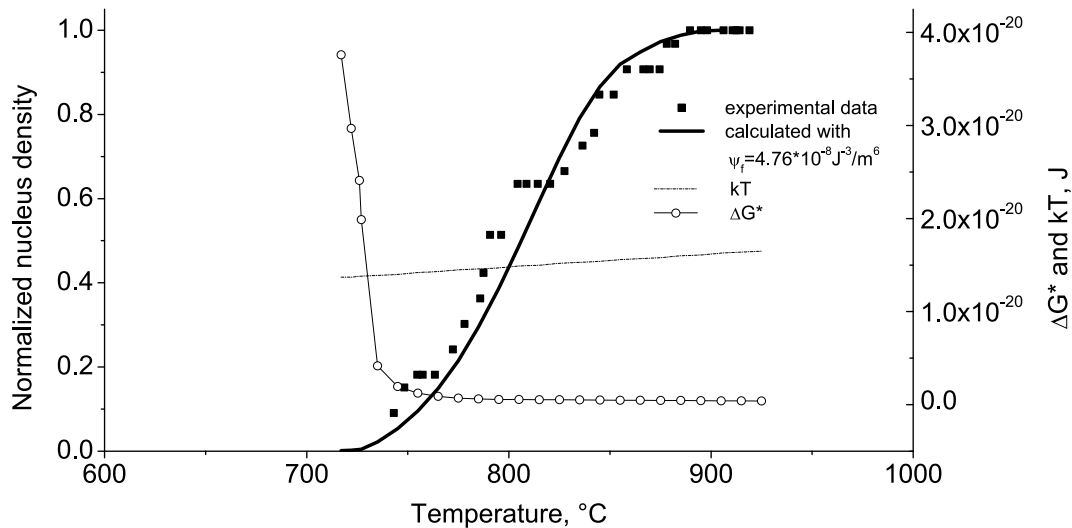


Figure 5.4. Experimental and calculated values for austenite nucleation density on the ferrite-ferrite grain boundaries and kT and ΔG^* values as a function of temperature for the C22 alloy. The ferrite nucleus density is scaled to the maximum in the experimental nucleation density.

The normalized austenite nucleus density is determined only for the second part (nucleation at ferrite) of the nucleus density curve, since there is insufficient data to perform the analysis for the first part (nucleation at pearlite). Figure 5.4 shows the measured austenite nucleus density normalized to the maximum nucleus density as a function of temperature. The best fit of the experimental data to Eq. (5.1) gives $\psi_f = 4.8 \pm 1.0 \times 10^{-8} \text{ J}^3/\text{m}^6$ for nucleation in the ferrite-to-austenite part of the transformation. In order to test the influence of the experimental uncertainty in the temperature scale, we also calculated ψ_f for the case, when the measured nucleus density was shifted to coincide with the A_1 temperature as calculated using thermodynamic databases. Then

we obtained a ψ_f value of $1.1 \pm 0.5 \times 10^{-8} \text{ J}^3/\text{m}^6$. The two ψ_f values are of the same order of magnitude as the value of ferrite nucleation from austenite determined by Offerman *et al.* ($5 \times 10^{-8} \text{ J}^3/\text{m}^6$ [13]) and much lower than the models predictions (see section 5.2.1). Such a low value gives information about the specific nucleation conditions, such as that nucleation occurs in places that are high in energy (for example, triple and quadruple points) and that austenite nuclei form with relatively low interfacial energy. For the nucleation near the pearlite phase, as was already mentioned before, we do not have sufficient data to quantify the parameter ψ_p . However qualitatively we can expect it to be even lower than ψ_f . It is worth to mention that by varying the activation energy of diffusion, Q , by a factor of 2 we get ψ_f of the same order of magnitude.

Figure 5.4 also shows that, except for the first several degrees, for most of the transformation range the calculated ΔG^* values lay below kT , since with the increasing temperature the driving force (Δg_V) increases and the energy barrier (ΔG^*) decreases. Regardless of the uncertainty in the value of ψ_f , it is clear that the activation energy for austenite nucleation is very small. The reason for the small activation energy for nucleation could be that the energy needed to form a new interface is largely compensated by the energy that is removed from the system by eliminating the grain boundary of the parent phase where nucleation takes place. Following [16] it is possible to establish that for the given ψ_f values we get into the regime in which the activation energy for nucleation is smaller than kT , but the critical nuclei are larger than a few atoms. Thus, only for the first several degrees of the transformation the CNT approach can be applied, but very little nucleation takes place in this regime. For most of the transformation range, however, application of the cluster dynamics approach (CD), as described by [16], is more appropriate. The derivation of the effective values for the activation energy enable the determination of the parameter γ^* , defined in ref. [16] by $\gamma^* = \Delta G^*/kT$, for which three different regimes can be identified:

- $\gamma^* > 1$. This regime corresponds to the small overheating values. The critical nucleus size n^* is then on the order of 10,000 atoms, including several hundred carbon atoms. If we assume a similar value for ψ_p as was found for ψ_f , it is clear that in this range only nucleation at pearlite colonies can take place.
- $\gamma^* \approx 1$. This regime corresponds to the intermediate range. For this regime the size of the critical nucleus is in the range of 300~800 atoms.
- $\gamma^* \ll 1$. This regime corresponds to the large overheating values, e.g. $\Delta T = 25^\circ\text{C}$ and higher, in which more than 90% of the nucleation takes place. The critical nucleus size is about 100~200 atoms. With such a size only a few carbon atoms are necessary to form the right composition. With increasing overheating the critical nucleus size as well as the required carbon atoms in a nucleus will decrease.

The rather large size of the critical nuclei in the first degrees of the transformation gives insight in the differences of nucleation behavior of austenite grains nucleated near the source of carbon (pearlite-pearlite or pearlite-ferrite grain boundaries, stage 1 in Fig. 5.3) and away from the source of carbon (ferrite-ferrite grain boundaries). In both cases the ψ values, and therefore the activation energy for nucleation, are very low, but the necessity of C atoms present in the nuclei makes the nucleation and further growth, necessary to observe the grains, near the source of carbon more favorable.

5.3.3. Growth types of individual grains

Figure 5.5 shows three types of austenite grain growth as observed during the experiments. Each individual growth type exhibits one or several of the following growth kinetics:

- I. fast growth (austenite growth in pearlite);
- II. slow growth (austenite growth in ferrite);
- III. extremely fast growth (massive growth).

The growth type A (see Fig. 5.5a) is similar to the overall transformation curves (compare with Fig. 5.2a, b). Due to this similarity it is possible to suggest that the transformation starts with the fast growth of austenite grains into the pearlite colonies (growth kinetics I) and continues as a slow ferrite-to-austenite transformation (growth kinetics II). The derived average pearlite-austenite interface (growth kinetics I) velocity, recalculated from the volume fraction of individual grains assuming that the austenite grains grow spherically, is about $0.03 \mu\text{m/s}$. This is more than an order of magnitude lower than the estimated value (see section 5.2.2). Two possible reasons for this deviation can be thought of. The first one is related to cementite decomposition. Molinder [27] estimated the activation energy for cementite decomposition to be about 838 kJ/mol . This is much higher than the activation energy for the carbon diffusion in austenite, which is about 147 kJ/mol . A consequence of this is that the rate at which cementite decomposes is not sufficient to keep the carbon content in austenite at the equilibrium value and this leads to strong carbon concentration gradients in the former pearlite (now austenite) areas. Indeed, a faster growth of austenite grains comparing to the cementite dissolution is often observed after etching [1, 2] (see also chapter 4) and obtained the name “pearlite ghosts”. The second possible explanation for the lower transformation rate can be related to the pearlite-to-austenite transformation not being a purely diffusion-controlled transformation, but having rather a mixed-mode character [28]. Diffusion-controlled transformation, the classical description of which is given by Zener [29], assumes that the diffusivity of an element (in this case carbon) is finite, whereas the rate of transformation of the crystallographic lattice, which is described by the interface

mobility [12], is infinitely large. In mixed-mode transformations both the diffusivity and the interface mobility are finite, which leads to slower transformation kinetics.

Once all pearlite has been consumed by austenite, the same austenite grains continue to grow further into the ferrite phase with the same crystallographic orientation, following growth kinetics II.

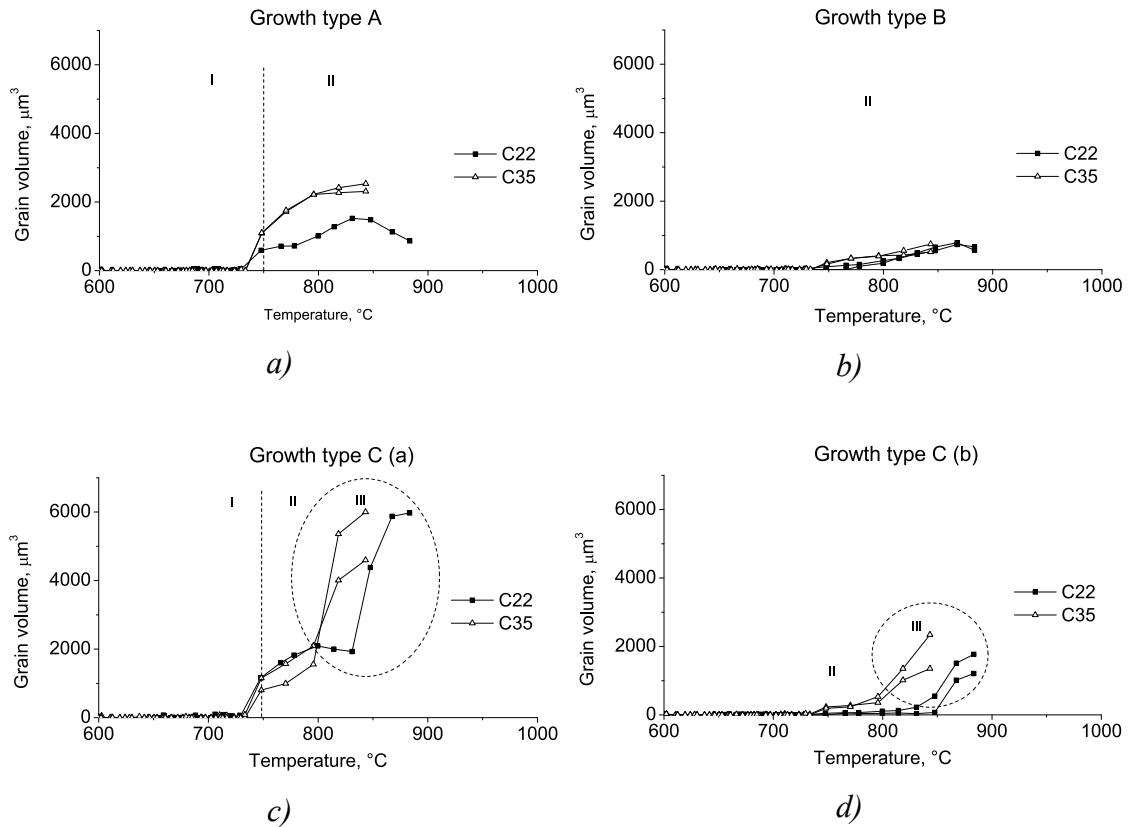


Figure 5.5. Growth types a) fast, possibly nucleated on pearlite-ferrite and b) slow, possibly nucleated on ferrite-ferrite grain boundaries; c) and d) are similar to a) and b) respectively, but with a growth acceleration in the last stages of the transformation. Open triangles are for C35 and solid rectangles for C22 alloys. I, II, and III indicate different growth kinetics.

Growth type B consists only of growth kinetics II, and is attributed to the nucleation and growth of new grains on the ferrite-ferrite grain boundaries (see Fig. 5.5b). It was shown earlier in chapter 4 that at the very early stages of the transformation the formation of austenite on the ferrite-ferrite grain boundaries (at quadruple points, grain edges and grain boundaries) can take place. In this case there is no direct contact with the source of carbon, the (former) cementite phase, so carbon

will be supplied from the areas rich in carbon through the ferrite matrix. The average austenite-ferrite interface (growth kinetics II) velocity derived from the 3DXRD measurement is approximately equal to $0.002 \mu\text{m/s}$. Similar to the austenite growth from pearlite, this is an order of magnitude lower than the estimated value (see section 5.2.2). The cause for the lower growth rate could be related to the change in the transformation mode from diffusion-controlled to mixed-mode transformation. The slow decrease in carbon content in the carbon-rich grains (austenite formed in the pearlite regions) due to slow carbon diffusion in austenite in combination with the longer diffusion distance slows down the transformation kinetics.

The peculiarity of the growth type C (see Fig. 5.5c, d) is that at the final stages of the transformation there is a strong acceleration of the process (growth kinetics III). The initial stages of the growth are similar to the growth types A and B – growth from the pearlite-ferrite grain boundaries (similar to the growth type A, growth kinetics I, II) or from the ferrite-ferrite grain boundaries (similar to the growth type B, growth kinetics II). However, the acceleration of the transformation at the last stage of the transformation is remarkable. A possible explanation for such a behavior is a change of transformation mode – from partitioning (below the T_0 temperature of the Fe-C system) to massive transformation (above T_0). In the latter type of transformation the original phase transforms to a new one with the same composition. In this case the transformation proceeds rather fast, since the redistribution of elements (in this case carbon) is not necessary. For the C22 alloy the observed transition in growth behavior occurs at $T = 850^\circ\text{C}$. At this temperature the carbon content in ferrite (x_α) and austenite (x_γ) for which both phases have the same Gibbs free energy, is equal to 0.022 wt.%. Correspondingly, for the C35 alloy at $T = 823^\circ\text{C}$ the equivalent carbon content is equal to 0.044 wt.%. These are values that are only slightly higher than the equilibrium carbon content of the ferrite. The ferrite phase can actually have a carbon content that is higher than the equilibrium value when it is in contact with austenite that also contains more carbon than the equilibrium [30, 31]. It is necessary to mention that acceleration of the growth is observed when both alloys are above the A_3 temperature. At this temperature the austenite phase has more carbon than the equilibrium value (see Fig. 5.6 where $x_{\gamma\alpha}^{C_{eq}}(2) < x^0(6)$). This leads to a higher carbon chemical potential in austenite in respect with equilibrium. In order to equilibrate the carbon chemical potential in both phases (ferrite and austenite), carbon will be pushed to the ferrite phase, enriching it to a higher (than equilibrium) values, thus creating necessary conditions for the massive transformation. Since austenite can form with the same carbon content as the parent ferrite phase, the character of the transformation then changes to the interface-controlled. The approximate interface velocity increases to $0.015 \mu\text{m/s}$ in the regime of growth kinetics III.

The change in transformation mode from diffusion-controlled to massive was observed by Schmidt *et al.* [32, 33], who studied the austenite formation from ferrite-pearlite microstructure during continuous heating using hot-stage confocal microscopy. During the experiments, under conditions above the T_0 temperature, the

growth rate increased drastically and the interface reaction-controlled growth mechanism was claimed to be responsible for the transformation.

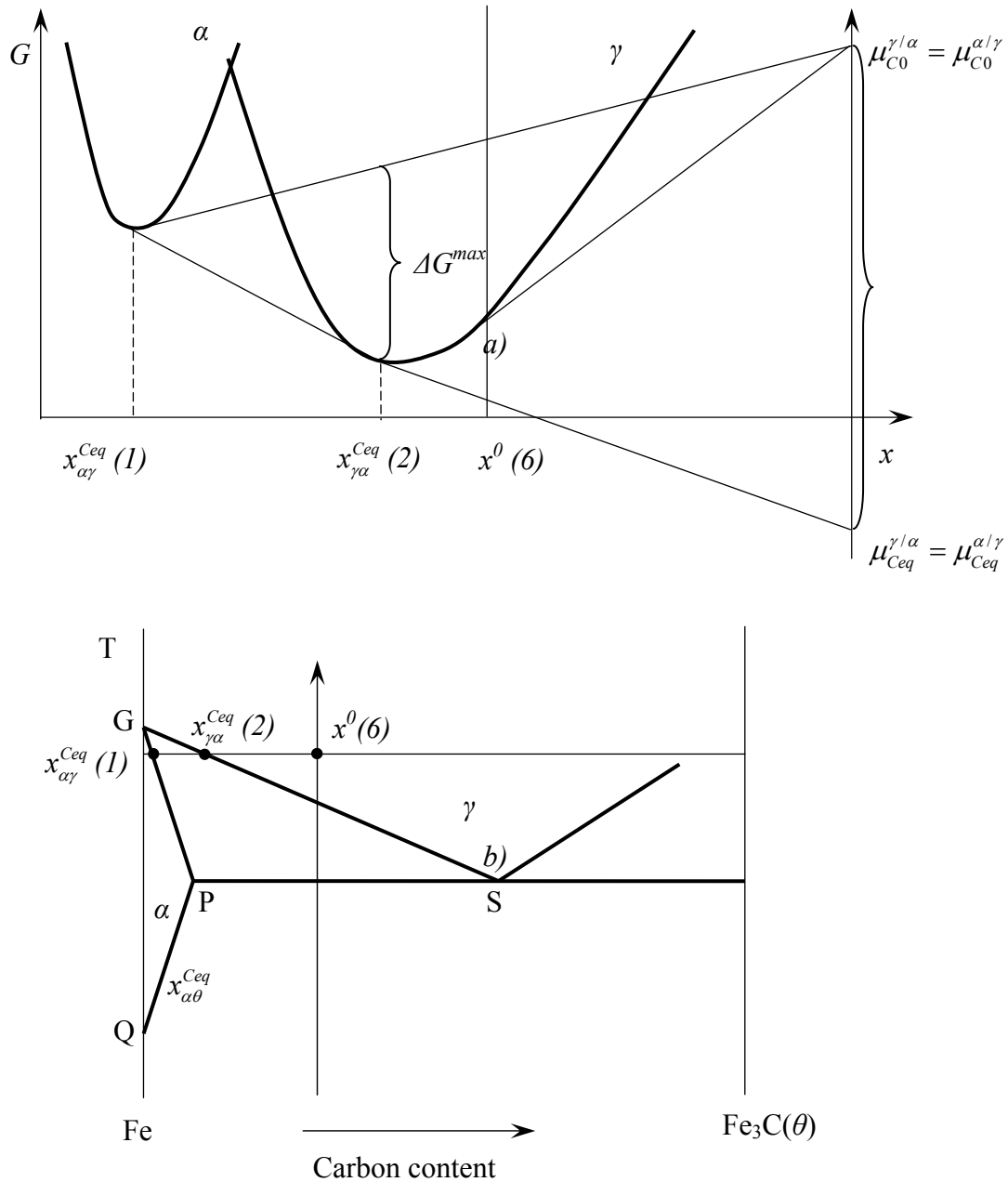


Figure 5.6. Schematic representation of the a) Gibbs free energy G as a function of the carbon concentration in ferrite (α), austenite (γ) and cementite (θ) at a temperature above A_3 and b) metastable Fe-C phase diagram, indicating notations for the carbon atomic fractions used throughout the text.

5.4. Conclusions

1. The austenite nucleus density as a function of temperature exhibits a two-stage behavior. It starts with very sharp increase during the first degrees of the transformation, which is likely related to the austenite nucleation on the pearlite-ferrite grain boundaries. In the second stage, there is a more gradual increase in the austenite nucleus density for the C22 alloy and no increase for the C35 alloy. This stage is likely related to austenite nucleation on the ferrite-ferrite grain boundaries. It is found that within the framework of the classical nucleation theory the ψ_f value, which represents the balance between the energy that is released by the elimination of the interfaces and the energy that is required for the formation of new interfaces, is much lower than literature models predict, and the resulting activation energy for nucleation is actually smaller than kT . This shows the need for the further development of theory describing nucleation for $\Delta G^* < kT$, which is beyond the scope of the current work.

2. Three different austenite grain-growth types were observed. Type A is similar to the overall transformation behavior, with fast pearlite decomposition into austenite and slow ferrite-to-austenite transformation. In this case, once an austenite grain consumed all pearlite, it continues to grow further into pro-eutectoid ferrite with the same crystallographic orientation. Growth type B is related to austenite nucleation and growth on ferrite-ferrite grain boundaries, away from the source of carbon. In this case, the formation of low-carbon austenite, compared to the growth type A, as was observed in chapter 4, can be expected. For growth type C, an acceleration of the transformation at the last stages of the transformation is likely to be related to a change in transformation mode – from partitioning to massive.

References

- [1] G.A. Roberts, R.F. Mehl, *Trans. ASM*, 1943, vol. 31, p.613-650.
- [2] G. R. Speich, V. A. Damarest, R.L. Miller, *Metall. Trans.*, 1981, vol. 12A, p. 1419-1428.
- [3] A. Jacot, M. Rappaz, *Acta Mater.*, 1999, vol. 47, no. 5, pp. 1645-1651.
- [4] T.A. Palmer, J.W. Elmer, *Scripta Mater.*, 2005, vol. 53, pp. 535-540.
- [5] H.F. Poulsen, *Three-dimensional X-ray diffraction microscopy: mapping polycrystals and their dynamics*, Springer, 2004, p. 156.
- [6] G. R. Speich, A. Szirmae, *Trans. Metall. Society*, 1969, vol. 245, p. 1063-74.
- [7] R. F. Mehl, *Trans. Amer. Society for Metals*, 1941, vol. 29, p. 813.
- [8] C. Garcia de Andrés, F.G. Caballero, C. Capdevila, *Scripta Mater.*, 1998, vol. 38, no. 12, pp. 1835-1842.
- [9] A. Roósz, Z. Gácsi, E.G. Fuchs, *Acta Metall.*, 1983, vol. 31, no. 4, pp. 509-517.
- [10] D.P. Datta, A.M. Gokhale, *Metall. Trans. A*, 1981, vol. 12A, pp. 443-450.

-
- [11] C.R. Brooks: *Principles of The Austenitization of Steels*, Elsevier Applied Science, London, UK, 1992, pp. 81-144.
- [12] J.W. Christian: *The theory of transformations in metals and alloys*, Oxford: Pergamon Press, 2002.
- [13] S.E. Offerman, N.H. van Dijk, J. Sietsma, S. Grigull, E.M. Lauridsen, L. Margulies, H.F. Poulsen, M.Th. Rekvelde, and S. van der Zwaag, *Science*, 2002, vol. 298, pp. 1003-1005.
- [14] S.E. Offerman, N.H. van Dijk, J. Sietsma, E.M. Lauridsen, L. Margulies, S. Grigull, H.F. Poulsen, and S. van der Zwaag, *Nuclear Instruments and Methods in Physics Research*, 2006, vol. B246, pp. 194-200.
- [15] S.E. Offerman, N.H. van Dijk, J. Sietsma, E.M. Lauridsen, L. Margulies, S. Grigull, H. F. Poulsen, and S. van der Zwaag, *Acta Mater.*, 2004, vol. 52, pp. 4757-4766.
- [16] N.H. van Dijk, S.E. Offerman, J. Sietsma, S. van der Zwaag, *Acta Mater.*, 2007, vol. 55, pp. 4489-4498.
- [17] K.C. Russel, *Acta Metal.*, 1969, vol. 17, pp. 1123-1131.
- [18] W.F. Lange III, M. Enomoto, H.I. Aaronson, *Metall. Trans. A*, 1988, vol. 19A, p. 427.
- [19] H.I. Aaronson and J.K. Lee, In: *Lectures on the Theory of Phase Transformations*, 2nd edition, Edt. H.I. Aaronson, TMS, Warrendale 1999.
- [20] J. Kučera, K. Stránský, *Mater. Sci. Eng.*, 1952, vol. 52, pp. 1-38.
- [21] P.C. Clemm, J.C. Fisher, *Acta Metall.*, 1955, vol. 3, p. 70.
- [22] W. Huang, M. Hillert, *Metall. Mater. Trans. A*, 1996, vol. 27A, pp. 480-483.
- [23] D. Gaude-Fugarolas, H.K.D.H. Bhadeshia, *J. Mater. Sci*, 2003, vol. 38, pp. 1195-1201.
- [24] J. Ågren, *Scripta Metall.*, 1986, vol. 20, pp. 1507-1510.
- [25] Handbook of chemistry and physics. Boca Raton (FL): CRC Press; 1989.
- [26] D. Kashchiev, Nucleation: basic theory with applications, Butterworth-Heinemann, 2000, p.530.
- [27] G. Molinder, *Acta Metall.*, 1956, vol. 4, pp. 565-571.
- [28] J. Sietsma, S. van der Zwaag, *Acta Mater.*, 2004, vol. 52, pp. 4143-4152.
- [29] C.J. Zener, *J Appl. Phys.*, 1949, vol. 20, pp. 950-953.
- [30] J.G. Speer, R.E. Hackenberg, B.C. Decooman, D.K. Matlock, *Philos. Mag. Lett.*, 2007, vol. 87, pp. 379-382.
- [31] M.J. Santofimia, L. Zhao, J. Sietsma, *Scripta Mater.*, 2008, vol. 59, pp. 159-162.
- [32] E. Schmidt, Y. Wang, S. Sridhar, *Metall. Mater. Trans. A*, 2006, vol. 37A, pp. 1799-1810.
- [33] E. D. Schmidt, E. B. Damm, S. Sridhar, *Metall. Mater. Trans. A*, 2007, vol. 38A, pp. 244-260.

Chapter 6

Two-dimensional phase field model for the pearlite+ferrite-to-austenite transformation during continuous heating

Abstract

In this chapter a model to describe the pearlite+ferrite-to-austenite transformation is built using the phase-field approach. The model is tested and validated for two heating rates: 0.05 and 3 °C/s. The model provides qualitative information on the microstructure that develops during continuous heating, and quantitative data on pearlite, ferrite and austenite volume fractions as well as carbon redistribution during the transformation. Pearlite phase is considered to be one phase with a uniform composition. Nucleation is described by the Classical Nucleation theory (CNT). Interface mobility is used as a fitting parameter to fit the experimental and the simulated austenite volume fraction curve. A rather good agreement in the development of the simulated and experimental microstructure is observed.

6.1. Introduction

In the recent years there have been numerous efforts in developing various microstructural models to describe the microstructural evolution during the heat treatment process [1, 2]. One of the models, which has received great attention, is the phase-field approach [3-9]. The phase-field method describes a microstructure using one or more field parameters, which are continuous functions of space. The big advantage of the phase-field method is that it is able to model the evolution of an arbitrary morphology without explicitly tracking the position of the interface.

Very few studies are presented in the literature to simulate transformation on heating using the phase-field approach. Thiessen *et al.* [10] simulated phase transformation of ferrite to austenite and the reversion back to ferrite during welding of low-carbon steel. The heating rates used during the welding are hundreds to thousands degrees per second, which is much higher comparing to the heating rates used during the convectional heat treatment process of low-carbon steels (a few degrees per second). During such fast heating carbon does not have time to redistribute, so a highly inhomogeneous austenitic structure is formed.

In this chapter a model to describe the ferrite+pearlite-to-austenite transformation during austenitization is formulated on the basis of the phase-field approach. The model is validated against the dilatometric measurements for two different heating rates: 0.05 and 3 °C/s and for four studied alloys. The interface mobility was used to fit the experimental results. A good agreement between the actual and the modeled microstructures as well as austenite fraction curves was obtained.

6.2. Model formulation

Modeling transformation on heating from the ferrite-pearlite initial microstructure using a phase-field approach is not a trivial task. A distinct difficulty in tackling this problem is the representation of the pearlite, which has a layered structure, consisting of alternating ferrite (low in carbon) and cementite (high in carbon) plates. To model pearlite lamellae explicitly will require a very fine grid, in the order of 10^{-7} m depending on the interlamellar spacing. On the other hand, the grid necessary to represent the microstructure on the micro scale is in the order of 10^{-5} - 10^{-4} m. Such a variation in grid sizes would require not only significant calculation times, but due to the memory size limitations of computers, it would be difficult or even impossible to carry out calculations. To overcome this difficulty, in the current approach pearlite is assumed to be one uniform phase with eutectoid composition.

6.2.1. Phase field concept

In the present work, the multi-phase formulation proposed by Steinbach *et al.* [3, 11] is employed to describe the ferrite (α) plus pearlite (p) to austenite (γ) on-heating transformation kinetics. The α/p to γ transformation kinetics can be described by an appropriate phase field parameter $\phi_i (i=1, \dots, N)$. Inside the grain i , ϕ_i is equal to 1 and outside the grain it is equal to 0. Within an interface between two grains i and j , $\phi_i + \phi_j = 1$ and $\phi_i < 1$, $\phi_j < 1$. In general, the requirement must be fulfilled everywhere:

$$\sum_{i=1}^N \phi_i(r, t) = 1, \quad (6.1)$$

where N is the total number of grains involved in the simulation,
 i is the grain number.

The rate of change of each phase field parameter with time is given by pairwise interaction with neighboring grains [4]:

$$\frac{d\phi_i}{dt} = \sum_j \mu_{ij} \left[\sigma_{ij} \left(\phi_i \nabla^2 \phi_j - \phi_j \nabla^2 \phi_i + \frac{\pi^2}{2\eta_{ij}^2} (\phi_i - \phi_j) \right) + \frac{\pi}{\eta_{ij}} \sqrt{\phi_i \phi_j} \Delta G_{ij} \right] \quad (6.2)$$

where μ_{ij} is the interfacial mobility,

σ_{ij} is the interfacial energy,

η_{ij} is the interfacial thickness,

ΔG_{ij} is the driving pressure,

i and j are the numbers of the neighboring grains.

The interface mobility μ_{ij} is temperature dependent, according to [12]:

$$\mu_{ij} = \mu_{ij}^0 \exp\left(-\frac{Q_{ij}}{kT}\right), \quad (6.3)$$

where μ_{ij}^0 is the pre-exponential factor describing the mobility of the interface,

Q_{ij} is the activation energy,

k is the Boltzmann constant,

T is the temperature.

The pre-exponential factor can be expressed as [10]:

$$\mu_{ij}^0 = \frac{d_{ij}^4 \cdot \nu_D}{kT}, \quad (6.3a)$$

where ν_D is the Debye frequency,
 d_{ij} is the jump distance of an atom, which can be expressed as an average interatomic distance as:

$$d_{ij} = \frac{1}{2}(V_i^{1/3} + V_j^{1/3}), \quad (6.3b)$$

V_i and V_j are the atomic volumes of two grains in contact.

The driving pressure ΔG_{ij} is a function of temperature and local composition x at location r and time t is calculated as:

$$\Delta G_{ij} = \Delta S_{ij} \Delta T, \quad (6.4)$$

where ΔS_{ij} is the difference of entropy between two phases and can be calculated using thermodynamic databases [13].

The simplifications applied to the formulation of pearlite in the current approach have their consequences for the thermodynamics. In deriving the relationship between pearlite and ferrite and between pearlite and austenite phases, the line of 0.7 wt. % C is taken to represent the simplified uniform pearlite (see Fig. 6.1). 0.7 wt. % C is chosen because it is the eutectoid (pearlite) composition for the studied alloy. The position of the horizontal line that separates α/p and α/γ regions is chosen to coincide with the A_1^+ temperature. The lines separating $\gamma/p-\gamma$, $\alpha-\alpha/\gamma$ and $\alpha-\alpha/p$ regions are chosen as the best fit to the existing lines that separate $\gamma/\theta-\gamma$, $\alpha-\alpha/\gamma$ and $\alpha-\alpha/\theta$ regions on the phase diagram calculated with thermodynamic databases respectively. The position of the last line, that separates $\gamma-\alpha/\gamma$ region, is chosen such that it passes through the A_3 temperature for the studied alloy on one side and through the intersection of horizontal line with the line that separates $\gamma/p-\gamma$ region on the other side of the diagram. Similar to the meta-stable extension of the line separating α and γ regions, which is commonly used in modeling the transformations on cooling, the equilibrium lines are also extended past the eutectoid temperature (see Fig. 6.2). It is necessary to mention that the extension of the lines above 0.7 wt. % carbon values are not important as the system never reaches those values.

In the current model the driving pressure for the transformation is calculated using linearized phase diagram (see Fig. 6.1 thick dash-dot lines) as:

$$\Delta G_{ij}(x^C, T) = \Delta S_{ij} \left(T^R + 0.5 \left[m_i^{Fe-C} (x_i^C - x_i^{CR}) + m_j^{Fe-C} (x_j^C - x_j^{CR}) \right] - T \right), \quad (6.4a)$$

T^R is the reference temperature,
 m_i^{Fe-C} , m_j^{Fe-C} are the slopes of lines separating two regions on the equilibrium phase diagram for the grains i and j accordingly (see Fig. 6.1),
 x_i^C , x_j^C are the local carbon content in the grains i and j ,
 x_i^{CR} , x_j^{CR} are the equilibrium carbon content in the grains i and j at the reference temperature.

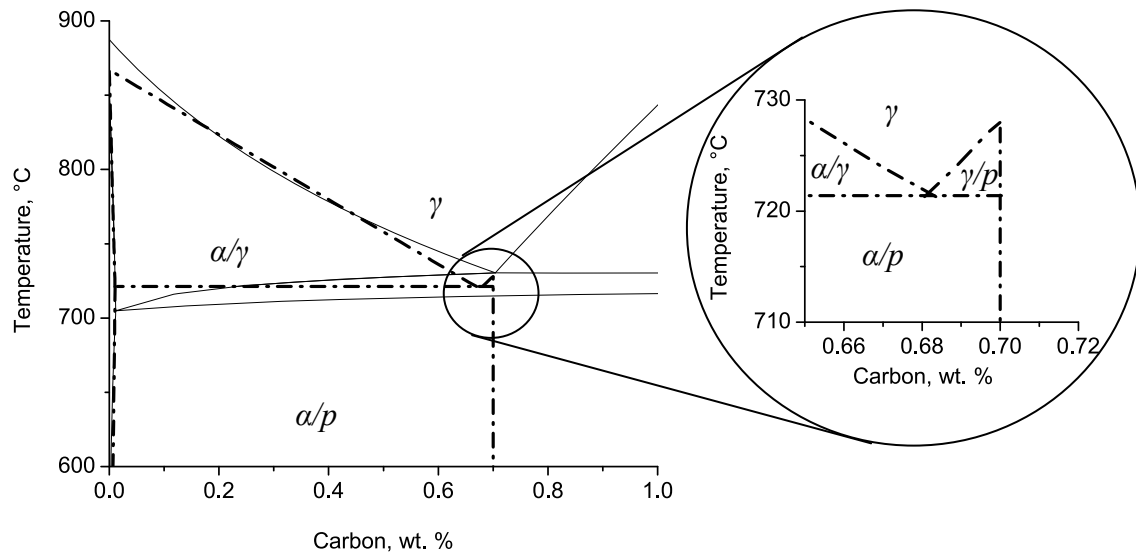


Figure 6.1. Phase diagram for C22 alloy as calculated using Thermo-Calc software [13] (solid thin lines) and linearized diagram as used in calculations (thick dash-dot line).

If two neighboring grains belong to the same phase and have the same composition, for example austenite, then $\Delta G_{ij} = 0$ and the grain growth is governed by the respective grain boundary energy and the curvature (see Eq. (6.2) the term in round brackets).

Besides the phase field equation, the diffusion equations are incorporated in the model and coupled with Eq. (6.2). As was shown experimentally in chapter 4, the only redistributing element during the phase transformation is carbon. Thus, only the carbon fluxes are calculated from the composition gradient and the diffusivity in each grain. The time dependence of the local concentration of carbon in a phase is given by:

$$\frac{\partial x_i}{\partial t} = \nabla \left[\phi_i D_i^C \nabla x_i^C + \phi_j D_j^C \nabla x_j^C \right], \quad (6.5)$$

D_i^C and D_j^C are the diffusivities of carbon in two grains in contact.

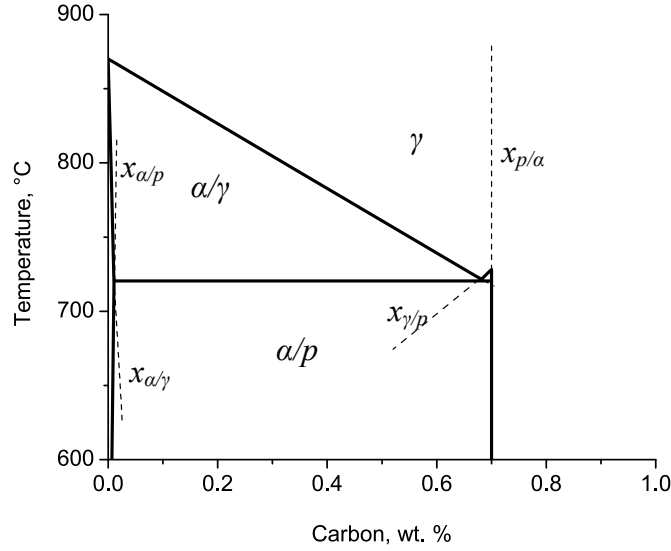


Figure 6.2. Extension of the equilibrium lines (thin dashed lines) as used during the simulations.

In the interface between two grains carbon atoms are assumed to redistribute according to the equilibrium partitioning ratio. The local composition $x^C(r, t)$, which is a continuous variable in r at the interface, splits into the austenite and ferrite compositions, $x_k^C(r, t)$ and $x_m^C(r, t)$ as:

$$x^C(r, t) = \phi_i(r, t) x_k^C(r, t) + \phi_j(r, t) x_m^C(r, t), \quad (6.6)$$

where k and m indicate phases (ferrite, austenite or pearlite).

In the further description for the simplicity reason the dependence of all the variables on r and t will be omitted. At the interface only the phase field parameters ϕ_i and ϕ_j are not zero and related by $\phi_j = 1 - \phi_i$. Eq. (6.6) then becomes:

$$x^C = \phi_i x_k^C + (1 - \phi_i) x_m^C. \quad (6.7)$$

An example for the carbon redistribution in the interface is given for two grains in contact that belong to ferrite ($k=\alpha$) and austenite phases ($m=\gamma$) (see Fig.6.3). For the other interfaces the principle described below and in Fig. 6.2 holds.

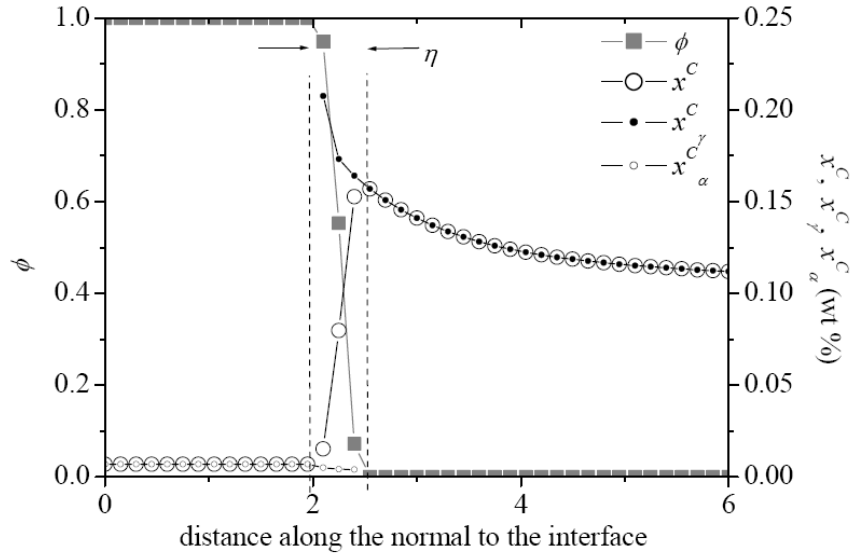


Figure 6.3. Carbon distribution in austenite, x_γ^C , in ferrite x_α^C , and overall carbon concentration, x^C [14].

In the bulk of α and γ grains the carbon concentration x^C reduces to x_α^C and x_γ^C respectively, while in the interface carbon is assumed to redistribute according to the partitioning ratio which is taken to be equal to the equilibrium partitioning ratio:

$$k^C = \frac{x_\alpha^C}{x_\gamma^C} = \frac{x_\alpha^{Ceq}}{x_\gamma^{Ceq}} = k^{Ceq}, \quad (6.8)$$

where k^C is the partitioning ratio;

k^{Ceq} is the partitioning ratio at equilibrium;

x_α^{Ceq} , x_γ^{Ceq} are the equilibrium carbon content in the grains α and γ respectively.

A more detailed description of carbon partitioning in the interface can be found in Chapter 2.3 of the thesis of Mecozzi [14].

Equations (6.1) and (6.5) allow to calculate the evolution of x and ϕ with location r and time t , thus describing the ferrite+pearlite-to-austenite transformation kinetics.

6.2.2. Nucleation

It was already shown in chapter 2 and the experimental part of the thesis, that once a suitable temperature has been reached, and this needs to be only slightly above the A_1 temperature, austenitization proceeds in two steps, namely nucleation and growth in pearlite and in pro-eutectoid ferrite areas. Pearlite phase is the one that transforms first to austenite. As an austenite region grows into pearlite, at the ferrite-pearlite interface, the eutectoid reaction of ferrite+carbide to austenite occurs. Nucleation of austenite in the pearlitic structure occurs preferentially at the intersection of pearlite colonies or the pearlite-ferrite grain boundaries (see chapters 2 and 5). New grains of austenite nucleate at the boundaries and one pearlite grain can contain more than one new austenite grains.

In the present model the Classical Nucleation Theory (CNT) is used to calculate the austenite nucleation rate [12] and is expressed (similarly to Eq. 5.1) as:

$$\dot{N} = N_n \beta^* Z \exp\left(-\frac{\Delta G^*}{kT}\right), \quad (6.9)$$

where N_n is the density of potential nucleation sites,

β^* is the frequency factor (the rate at which single atoms are added to the critical nucleus),

Z is the Zeldovich non-equilibrium factor, which corrects the equilibrium nucleation rate for nuclei that grow beyond the critical size,

ΔG^* is the activation barrier.

ΔG^* is related to the chemical Gibbs free energy (Δg_V from the Gibbs free energy curves) as (see Eq. (5.3)):

$$\Delta G_i^* = \frac{\psi_i}{\Delta g_V^2}$$

where ψ contains all the information about the shape of the nucleus (geometrical factors) and the energies, σ_i , of the interfaces that are involved in the nucleation process, i.e. the newly formed interfaces and matrix interfaces where the nucleation took place;

Δg_V is the difference in Gibbs free energy per unit volume between parent and forming phase (driving force for nucleation).

A more detailed description of each of the parameters can be found in chapter 5 section 5.2.1.

6.3. Experimental and simulation conditions

6.3.1. Materials and dilatometric measurements

In order to examine the effect of heating rate on the evolution of the microstructure during continuous heating, the phase transformations in C22, C35, C45 and C60 alloys were analyzed using a Bähr 805A/D dilatometer. Chemical compositions of studied alloys are shown in Table 3.1 and the initial microstructures are presented in Fig. 3.1a-d. The samples were heated by a high-frequency induction coil with two different heating rates: 0.05 and 3 °C/s. The detailed description of the dilatometric measurements as well as the analysis of the dilatation curves is given in chapter 3.2.3.

Apart from the continuous heating tests mentioned above, a set of interrupted heating experiments was performed to study the evolution of the microstructure. The experimental alloys were heated up with 0.05 °C/s and 3 °C/s heating rates to different temperatures within the ferrite+pearlite-to-austenite transformation region and directly quenched with cooling rates in the range of 750-850 °C/s. Samples for metallographic examinations were ground, polished, etched and examined in optical and scanning electron microscopes, as described in chapter 3.2.1.

6.3.2. Simulation conditions

Two-dimensional phase-field simulations of the ferrite+pearlite-to-austenite transformation during continuous heating were performed using the MICRESS code [15]. The initial microstructures of the simulated alloys, which were derived from the original micrographs (see Fig. 3.1), are given in Fig. 6.4a-d. The calculation domain size is $139 \times 104 \mu\text{m}^2$. The system is considered to be in para-equilibrium, where the only diffusing element is carbon (see section 6.2.1). The diffusivity values for carbon are listed in Table 6.1. The diffusion parameters for the pearlite phase are not that important since the pearlite phase has constant composition. The thermodynamic data for the driving-force calculation were taken from the linearized phase diagrams for given alloys calculated by means of Thermo-Calc software [13] (see Fig. 6.1).

The mobilities of different interfaces were treated individually as temperature dependent based on the lattice dimensions and calculated according to Eq. (6.3) and Tables 3.3 and 6.2 for the α/α' - and γ/γ' -interfaces. The other activation energies are determined from the comparison of simulation and experimental fraction curves, as will be presented in section 6.4. Interfacial energies were derived from [16].

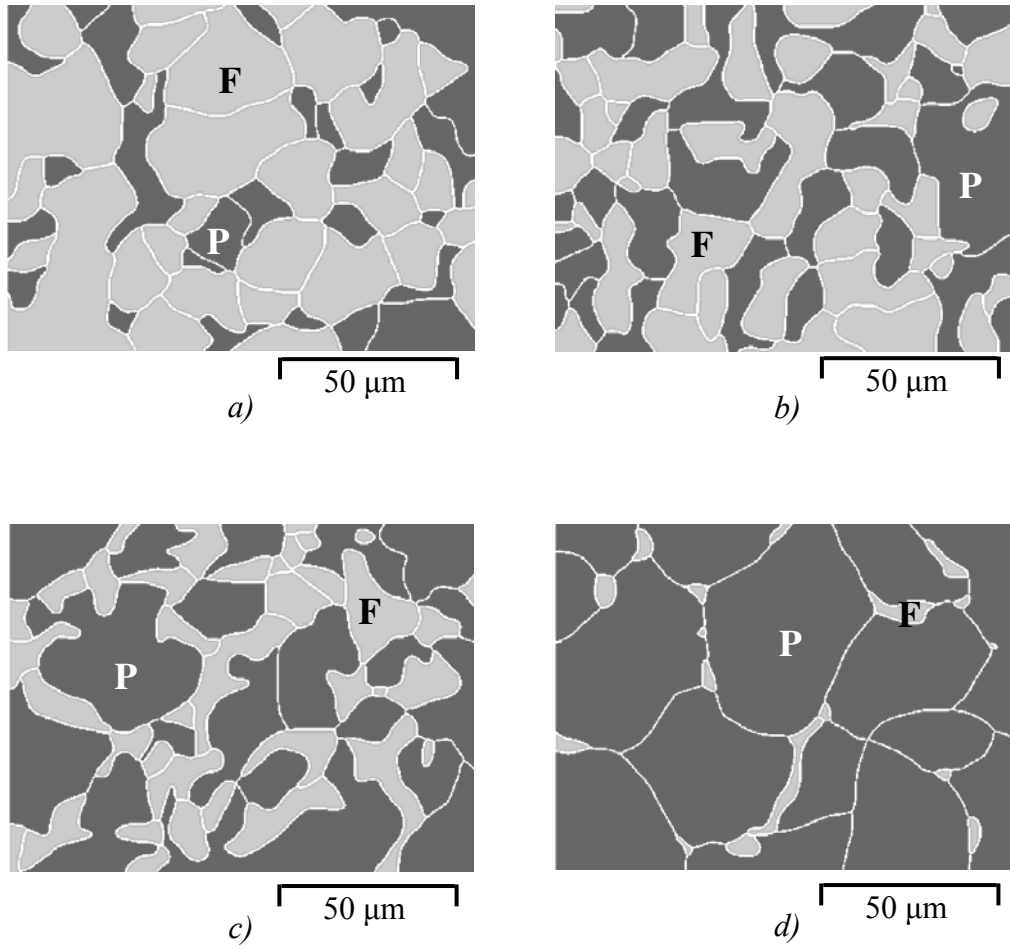


Figure 6.4. Initial simulated microstructures for a) C22; b) C35, c) C45 and d) C60 alloys. (Compare with equivalent initial microstructure from Fig. 3.1). P = pearlite, F = ferrite.

Table 6.1. Diffusion parameters used for the calculations [17].

$D_{0\alpha}^C$	$D_{0\gamma}^C$	Q_α^C	Q_γ^C
(m ² /s)		(kJ/mol)	
2.2×10^{-4}	1.5×10^{-5}	122.5	142.1

Table 6.2. Activation energy for mobility and interfacial energy [16] for C22, C35, C45 and C60 alloys (literature values).

	$\gamma:\gamma$	$\alpha:\alpha$	$\gamma:\alpha$	$\gamma:p$	$\alpha:p$	$p:p$
Q_{ij} (kJ mol ⁻¹)	185 [10]	150 [10]	to be determined			
σ_{ij} (J m ⁻²)	0.76	0.5	0.39	0.94	1.05	1.25

The atomic volumes were related to the lattice parameters (see Table 3.3) by:

$$V_{\alpha} = \frac{1}{2}a_{\alpha}^3, \quad V_{\gamma} = \frac{1}{4}a_{\gamma}^3, \quad V_{\alpha+\theta} = (1-\rho)V_{\alpha} + \rho V_{\theta}, \quad V_{\theta} = \frac{1}{12}a_{\theta}b_{\theta}c_{\theta} \quad (6.10)$$

where ρ is the cementite fraction in pearlite and is taken to be 0.1 for all the studied alloys.

Nucleation is assumed to take place on grain boundaries: corners for 0.05 °C/s and corners and edges for 3 °C/s heating rate. The nucleation density was estimated from the optical micrographs. The temperature of the start of nucleation was set equal to the eutectoid temperature determined from the linearized equilibrium phase diagram. The frequency factor β^* is calculated according to Eq. (5.2). The ψ -values are taken based on the previously reported findings (see Chapter 5): $\psi_{\alpha} = 4.76 \times 10^{-8}$ and $\psi_p = 1.0 \times 10^{-10}$ J³/m⁶. Z is taken to be 0.05.

The Gibbs free energy (Δg_V , see Eq. (5.3) and (6.9)) as a function of the carbon concentration is calculated using Thermo-Calc software and is schematically represented in Fig. 4.1a at a temperature above the eutectoid temperature. The maximum driving force for the transformation is determined as the difference between $G^{\alpha/\theta}$ and G^{γ} values (see Fig. 4.1a). It is necessary to point out that for the nucleation rate estimation the real situation, with pearlite as a ferrite-cementite mixture and not the simplified pearlite, was used for the calculations, since the Gibbs free energy curves cannot be calculated using thermodynamic databases for pearlite as a single phase. In addition, this gives a more realistic representation of the nucleation process without effects on the computation time.

In addition to the physical parameters, there are a number of numerical parameters that have to be chosen to ensure the stability and convergence of the calculations as well as give a reasonable compromise between the time for the calculation and accuracy. Those are the node size $\Delta x = 0.33$ μm and interfacial thickness η . For the above mentioned parameters, the interfacial thickness is the most important and is taken to be $\eta = 4\Delta x$, which allows to avoid numerical instability problems [18].

6.4. Results and Discussion

6.4.1. Volume fractions

6.4.1.1. Overall austenite volume fraction

Figure 6.5 shows the austenite volume fraction as measured with dilatometry (solid triangles), calculated using the phase-field approach (open circles) and as calculated using thermo-dynamic databases (dashed-dot line). As was mentioned earlier in this chapter, the mobilities of different interfaces were treated individually as temperature dependent, based on the lattice dimensions and calculated according to Eq. (6.3) and Tables 3.3, 6.2 and 6.3. The values for the activation energies for the mobility of the $\gamma:\alpha$, $\gamma:p$ interfaces from Table 6.3 are the fitted values: they give the best agreement between the calculated and the experimentally measured austenite volume fraction curves.

The values for the activation energies for $\alpha:p$, $p:p$ are taken to be larger than the other values to ascertain the stability of the ferrite-pearlite and pearlite-pearlite interfaces.

There is a good agreement between the experimental and simulated austenite volume fraction transformed curves for the four compositions and the two heating rates (see Fig 6.5). For the 0.05 °C/s heating rate the pre-exponential factor ($\mu_{p\gamma}^0$) for the pearlite-austenite interface is taken to be 10 times smaller than calculated with Eq. 6.3a, but is the same for all the studied alloys.

For 3 °C/s no adjustment (for the pearlite-austenite as well as for the ferrite-austenite interfaces) to the as-calculated interface mobility values was done. The possible reason for the retardation in the interface mobility for the lower heating rate can be related to two factors. First of all, pearlite, which has a lamellar structure, has a tendency to spheroidize at elevated temperatures. The spheroidization is only observed at rather low heating rates (like 0.05 °C/s) and was detected during experiments for all the studied alloys (see as an example Fig. 6.6). No spheroidization was observed at higher heating rates. The movement of the interface in a lamellar structure is quite different from the spheroidized one. In the first case, the interface moves rather quickly due to the short carbon diffusion distances (carbon is already present at the reaction point). In the second case, the spheroidized cementite particles will serve as a pinning factor for the propagation of the interface. In addition, carbon will have to diffuse through the austenite phase, thus the pearlite-to-austenite transformation will be retarded.

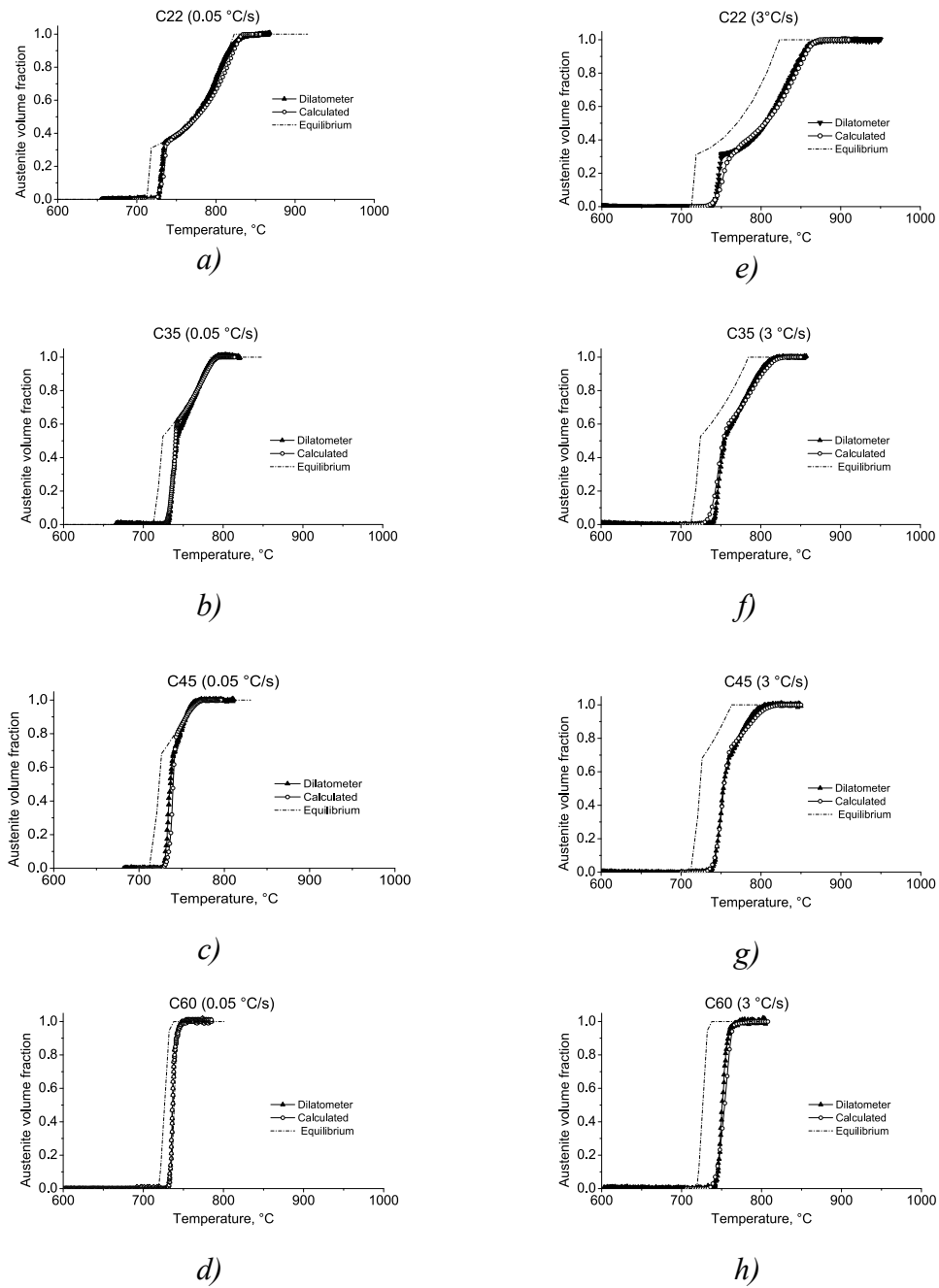


Figure 6.5. Measured with dilatometer (solid triangles), calculated (open circles) and para-equilibrium values as calculated used thermo-dynamic databases (dash-dot) austenite volume fraction transformed as a function of temperature during continuous heating of a), e) C22; b), f) C35; c), g) C45 and d) and h) C60 alloys. a)-d) 0.05 °C/s and e)-h) 3 °C/s heating rate.

Table 6.3. Activation energy for mobility for C22, C35, C45 and C60 alloys (fitted values).

	$\gamma:\alpha$	$\gamma:p$	$\alpha:p$	$p:p$
Q_{ij} (kJ mol ⁻¹)	150	150	215	215

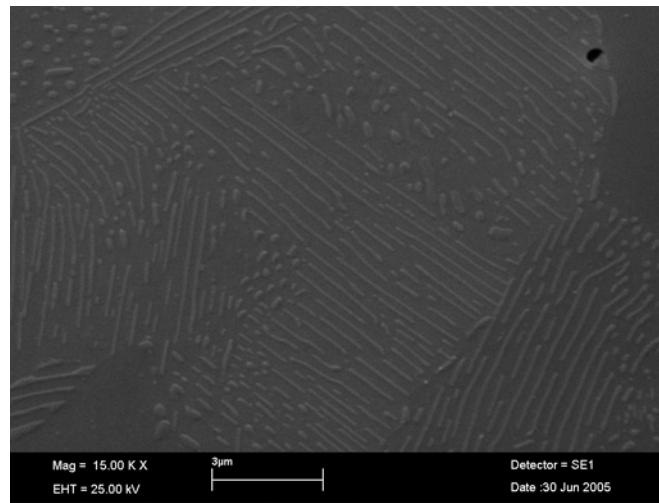


Figure 6.6. A scanning electron microscope micrograph showing the spheroidization of the pearlitic structure in C35 alloy at 720 °C heated with 0.05 °C/s heating rate.

The second possible reason may be due to the solute-drag effect of substitutional solutes (in this case mainly Mn). Pearlite in comparison to pro-eutectoid ferrite is very inhomogeneous both in carbon and Mn. For C35 alloy at 670 °C the microstructure consists of two phases – pearlite (which is the mixture of ferrite and cementite) and pro-eutectoid ferrite. The typical Mn content of those phases is 0.6 wt. % of Mn in the ferrite phase and 6.7 wt. % of Mn in the cementite phase. With increasing temperature there will be a slight decrease of Mn content in ferrite and above the eutectoid temperature (in the two-phase ferrite-austenite region) the typical composition of phases will be: 0.4 wt. % of Mn in the ferrite phase and 1 wt. % in the austenite phase. Thus, when austenite is formed not only the carbon has to redistribute between the phases but also Mn. In general, due to rather low Mn diffusion (at 700 °C the Mn diffusivity in ferrite is $6 \cdot 10^{-17}$ m²/s, compare with the carbon diffusivity in ferrite at the same temperature, being equal to $6 \cdot 10^{-11}$ m²/s), it would not be expected to redistribute completely and ortho-equilibrium will not be maintained. Instead, the transformation can be expected to proceed under para-equilibrium conditions and the forming austenite phase would inherit the chemical composition (substitutional

elements but not carbon) from the parent ferrite-pearlite phases (see also chapter 4, where it was shown that carbon was the only element that redistributed between the phases). On the other hand, the uniqueness of pearlite is that diffusion distances are very small and excess (comparing to the Mn content in austenite) of Mn is already present at the ferrite-pearlite interfaces. Once austenite is nucleated on the pearlite-pearlite or pearlite-ferrite grain boundary, there will be a driving force for Mn diffusion into austenite and due to short diffusion distance it is likely that Mn would have the possibility to redistribute locally. It is reasonable to assume, that this effect will be more pronounced at lower heating rate, as there will be more time and thus possibility for the diffusion process to take place. When the ferrite-austenite boundary moves Mn atoms will migrate along with the boundary and therefore exerting a solute drag that will, thus, reduce the boundary velocity. This process dissipates some of the Gibbs energy and will consume some of the driving force for the grain boundary migration. As was shown in [19] when the growth rate approaches zero, partitioning of substitutional elements will increasingly take place, such that deviations from assuming para-equilibrium conditions to determine the driving pressure are expected (if Mn partitions then the decrease in the driving force can be expected). With increasing heating rate there will be hardly any time available for Mn redistribution so the para-equilibrium conditions will be maintained.

The situation with pro-eutectoid ferrite-to-austenite transformation is slightly different. First of all, the diffusion distances are much large so it is unlikely that Mn would have the possibility to redistribute from places reach in Mn (former pearlite grains) towards the propagating ferrite-austenite interface during the transformation even at relatively low heating rates. Secondly, austenite formation from ferrite on heating is not the same as the ferrite formation from austenite on cooling. In the second case, the newly formed ferrite phase has lower Mn content in comparison to austenite. Ferrite is not able to contain as much Mn so during the austenite-to-ferrite-transformation a spike of Mn in front of the moving interface will be formed [20]. This accumulated Mn will try to move with the interface thus retarding the austenite-to-ferrite transformation. It is likely that the gradual transition from kinetics controlled by the diffusion of substitutional elements at higher temperatures to a kinetics controlled by the diffusion of carbon at lower temperatures will take place. Situation upon heating is different. When the austenite-ferrite interface migrates there will be a lack (not excess) of Mn, so no spike will be formed and austenite phase would inherit the Mn composition from the parent ferrite phase.

Unfortunately, at the current stage of the technology it is impossible to measure directly the evidence of Mn segregation at the cementite-austenite and ferrite-austenite grain boundaries during the phase transformation. However, as was indirectly shown earlier [19-22], the consideration of solute drag by Mn in Fe-C-Mn alloys leads to a better fit between experimental data and the models.

In the current model the effect of Mn as well as the internal lamellar structure of pearlite is not incorporated. In addition, the assumption of the para-equilibrium condition during the whole transformation range, even though justified, might not be true and may result in a stronger solute drag effect. Instead, as it was proposed in [19,

23] a gradual transition from para-equilibrium at high heating rates to negligible-partition local equilibrium (LENP) at low heating rates must be considered in pearlite-to-austenite transformation. At lower heating rates substitutional elements will be able to redistribute more in the vicinity of the interface, thus promoting the solute drag effect.

To summaries, the consideration of solute drag by Mn as well as pinning of the grain boundary movement by spheroidized cementite particles and change in the carbon diffusion pattern gives a reasonable good explanation for the retardation of the pearlite-to-austenite transformation at slow heating rates (0.05 °C/s), which is taken into account by reducing the pre-exponential mobility factor for pearlite-to-austenite transformation by a factor of 10. For higher heating rates due to the shortage of time necessary for diffusion to take place, the pearlite-to-austenite transformation would most probably proceed under the para-equilibrium considerations. Pro-eutectoid ferrite-to-austenite transformation for all heating rates as well as all temperatures is more likely to proceed under the para-equilibrium conditions.

6.4.1.2. Ferrite and pearlite volume fractions

Besides the overall austenite volume fraction curves additional information that can be easily extracted from the simulations but is much more difficult to do with dilatometric measurements is on the ferrite and pearlite volume fractions as a function of temperature and heating rate (see Figs. 6.7-6.8). The general tendency clearly seen from the figures is that with increasing heating rate the transformation shifts to the higher temperatures and the transformation range itself increases for both pearlite and ferrite parts of the transformation. This indicates that the transformation kinetics is most probably a diffusion-controlled process (carbon or interface diffusion). With increasing the heating rate there is less time available for the diffusion process to take place, which is the essential step in austenite formation, thus pearlite and ferrite phases survive to higher temperatures and consequently less austenite is formed.

It is interesting to note that the effect of the pearlite dissolution on the overall austenitization kinetics is limited. The maximum effect is obtained at lower overheating values - with increasing heating rate the transformation is delayed to higher temperatures. As the austenite formation proceeds with increasing temperature the effect of pearlite dissolution vanishes and there is no effect on the temperature at which austenitization finishes.

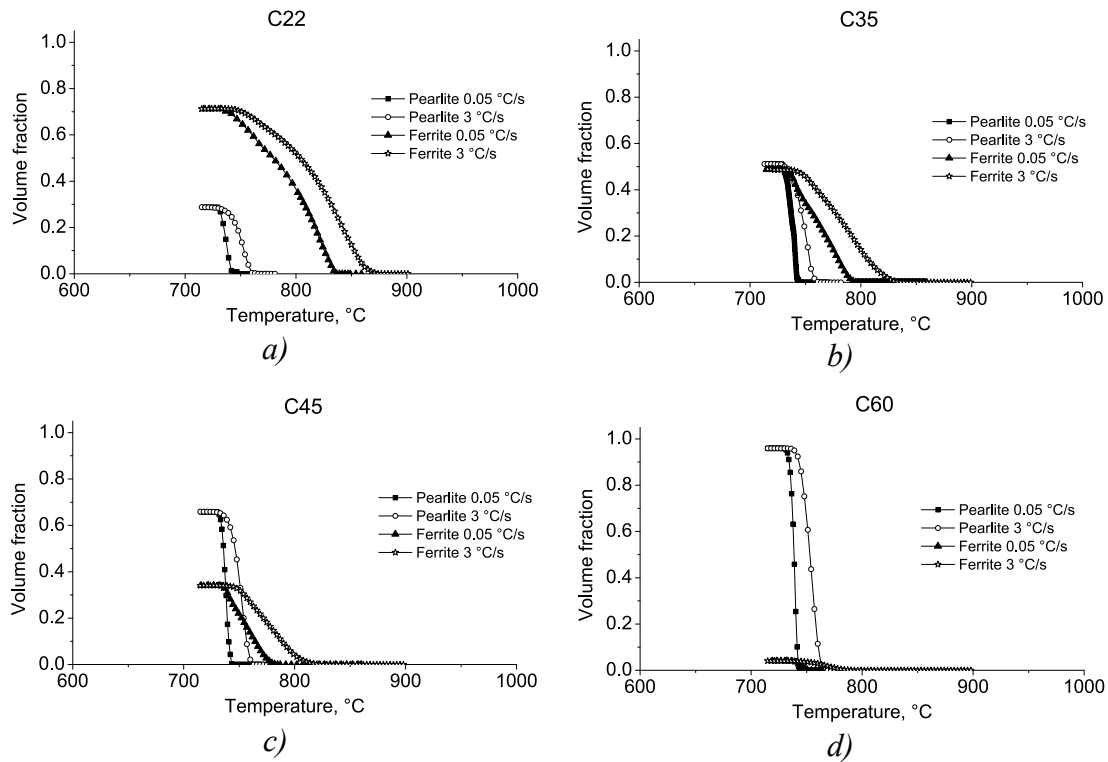


Figure 6.7. Ferrite and pearlite volume fractions as the function of temperature for a) C22, b) C35, c) C45 and d) C60 alloys and for two different heating rates: 0.05 °C/s - solid rectangle/triangle lines and 3 °C/s open circle/start lines.

The effect of the different carbon content on the transformation kinetics is obvious: with the decreasing carbon content the transformation range increases and mainly due to the ferrite part. The pearlite-to-austenite transformation part is almost unaffected by the change in carbon concentration. This is related to the increase in the ferrite phase present in the sample, which is a more stable phase comparing to pearlite and agrees well with the phase diagram, as the one presented in Fig. 6.1. In addition, the carbon diffusion distances decrease with the increasing of carbon content due to the increase of pearlite volume fraction present in the microstructure.

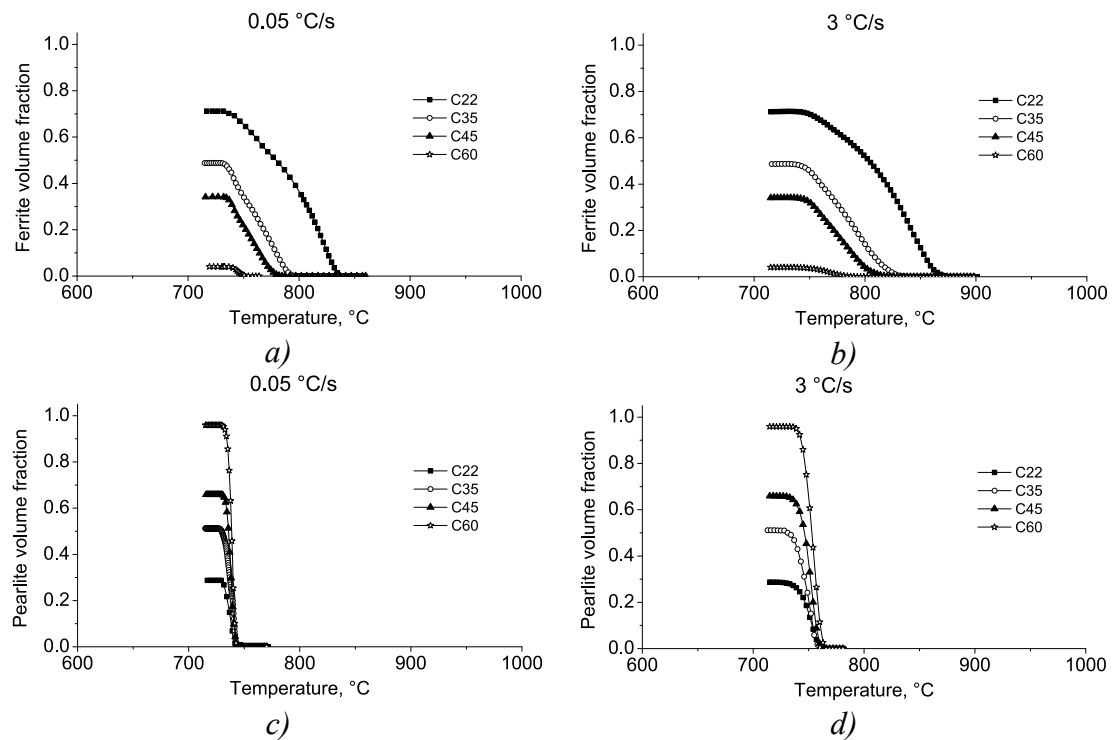


Figure 6.8. a), b) “ferritic” and c), d) “pearlitic” austenite volume fractions as a function of temperature for: C22 (solid rectangle), C35 (open circle), C45 (solid triangle) and C60 (open star) alloys.

6.4.2. Evolution of the microstructure and carbon content

Figures 6.9, 6.10 show the evolution of the microstructure for the C35 alloy during continuous heating with 0.05 and 3 °C/s heating rates respectively. The simulated microstructures are compared to the optical micrographs. C35 alloy is chosen as an example. The other alloys show similar tendencies and are not presented here.

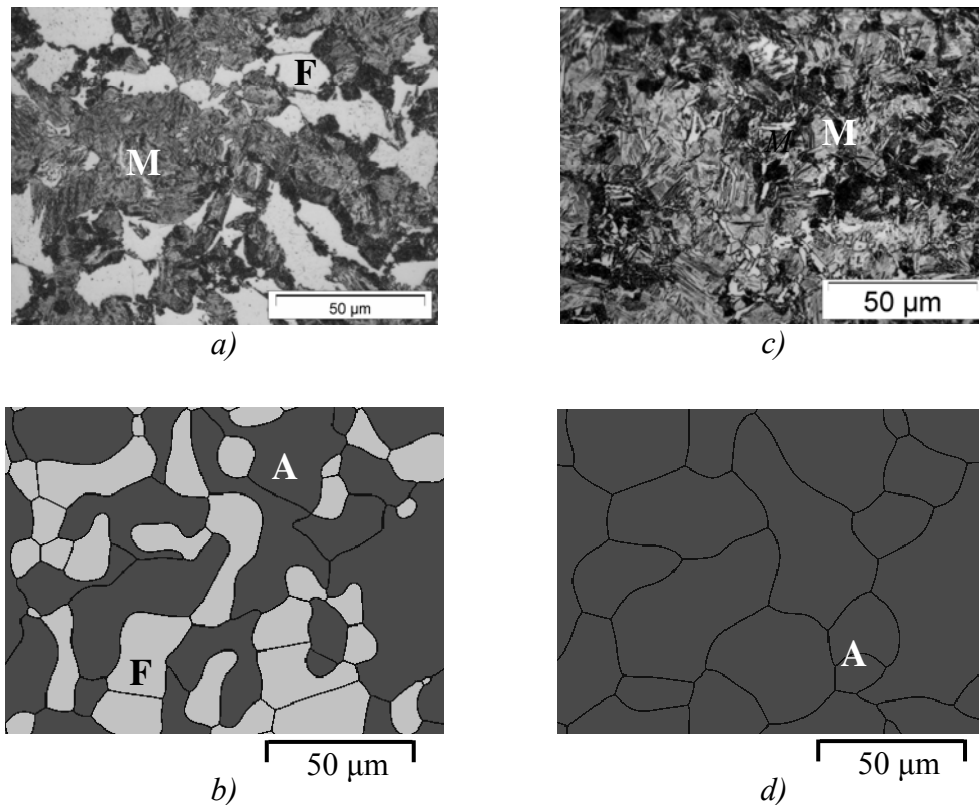


Figure 6.9. The evolution of the microstructure for C35 alloy heated with 0.05 °C/s heating rate to a), b) 745 °C and c), d) 805 °C and directly quenched. a), c) optical micrographs and b), d) equivalent simulated microstructure.

A = austenite, F = ferrite, M = martensite.

Figures 6.9-6.10 correctly represent the overall tendencies – first pearlite transforms to austenite and then ferrite-to-austenite transformation takes place. After some time, which is different for each heating rate, there will be no pearlite present in the microstructure (see Fig. 6.9a,b and 6.10a,b) and the microstructure will consist of a ferrite-austenite mixture (on quenching austenite will transform to martensite). With increasing heating rate the size of the final austenite grain decreases. The increase in a heating rate results in an increase of the driving force for the transformation, thus resulting in a higher nucleus density.

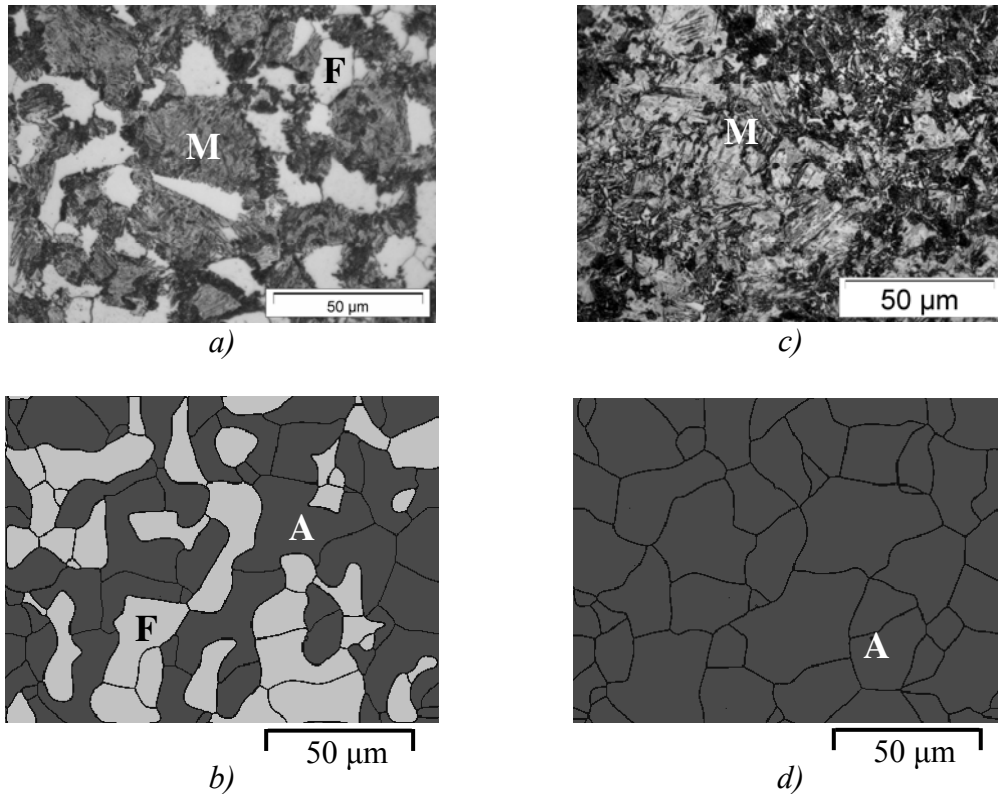


Figure 6.10. The evolution of the microstructure for C35 alloy heated with 3 °C/s heating rate to a), b) 760 °C and c), d) 835 °C and directly quenched. a), c) optical micrographs and b), d) equivalent simulated microstructure.

A = austenite, F = ferrite, M = martensite.

Figures 6.11, 6.12 show the carbon concentration maps at different temperatures and at different scales. It is clearly seen that at 0.05 °C/s uniform carbon redistribution structure develops, where as at 3 °C/s carbon gradients are present after the transformation is completed (compare Fig. 6.11c and 6.12c). This is true not only for the austenite phase but for the ferrite phase as well (compare Fig. 6.11b and 6.12b). Stronger concentration gradients at higher heating rate are according to the expectations. At higher heating rates there is no time for carbon to redistribute, so a more inhomogeneous structure is formed.

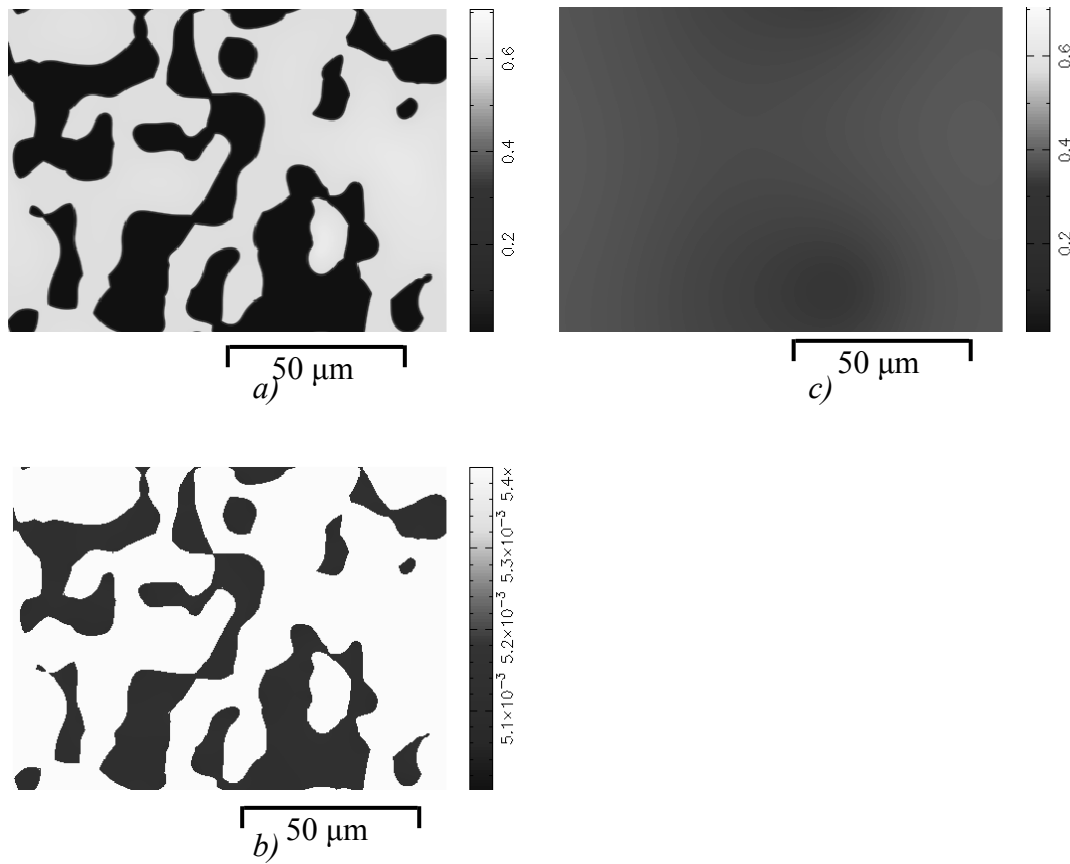


Figure 6.11. Carbon concentration maps for C35 alloy heated with $0.05 \text{ }^\circ\text{C/s}$ to a), b) $745 \text{ }^\circ\text{C}$ and c) $805 \text{ }^\circ\text{C}$. b) shows the carbon gradients in the ferrite phase. For the color version refer to the appendix.

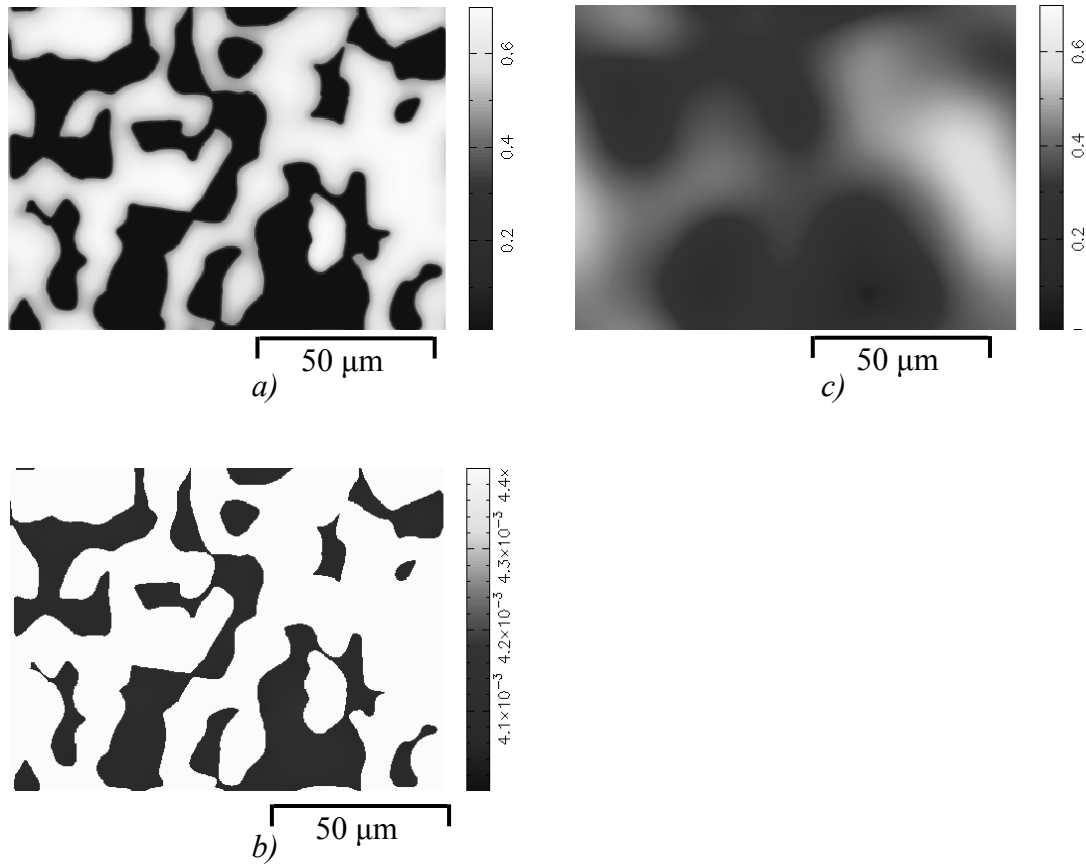


Figure 6.12. Carbon concentration maps for C35 alloy heated with $3\text{ }^{\circ}\text{C/s}$ to a), b) $760\text{ }^{\circ}\text{C}$ and c) $835\text{ }^{\circ}\text{C}$. b) shows the carbon gradients in the ferrite phase. For the color version refer to the appendix.

6.4.3. Growth types of individual grains

Another outcome of the simulations that can be deduced is the growth type of individual grains. The experimentally measured different growth types of individual austenite grains were already discussed in chapter 5. During the simulations only growth type A with growth kinetics I and II was reproduced (see Fig. 6.13.).

Indeed, as it was proposed in chapter 5, this type of growth corresponds to the grains that nucleated on the pearlite-pearlite or pearlite-ferrite grain boundaries. Newly formed austenite grains consumed first rather quickly pearlite grains (growth kinetics I) and later grew further rather slowly into pro-eutectoid ferrite (growth kinetics II).

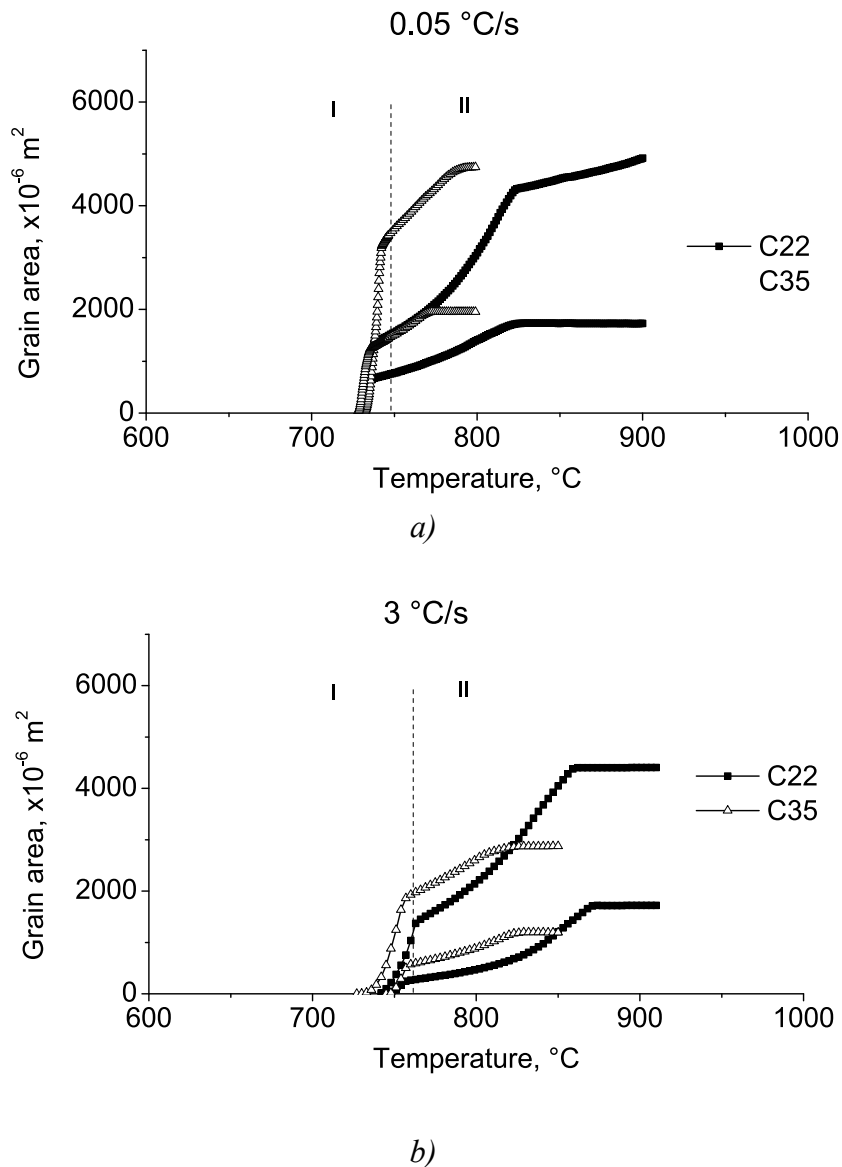


Figure 6.13. Growth type A: fast, nucleated on pearlite-pearlite or pearlite-ferrite grain boundaries. Open triangles are for C35 and solid rectangles for C22 alloys. I and II indicate different growth kinetics. The heating rates are: a) 0.05 and b) 3 °C/s. Individual lines correspond to different austenite grains.

Figure 6.14 shows the corresponding average carbon content in the austenite grains. During the entire transformation range the average carbon content in different grains follows the same line for lower heating rate (0.05 °C/s). For higher heating rate (3 °C/s), however, some deviations in carbon content between different grains is observed. These deviations are absent at the beginning of the austenite formation

(temperature range where pearlite transforms to austenite) and increase after all the pearlite grains are consumed by the austenite grains and transformation proceeds further into the pro-eutectoid ferrite phase. This effect is related to the increased diffusion distances which is necessary for carbon to travel from the areas rich in carbon (former pearlite grains) to the ferrite-austenite interface.

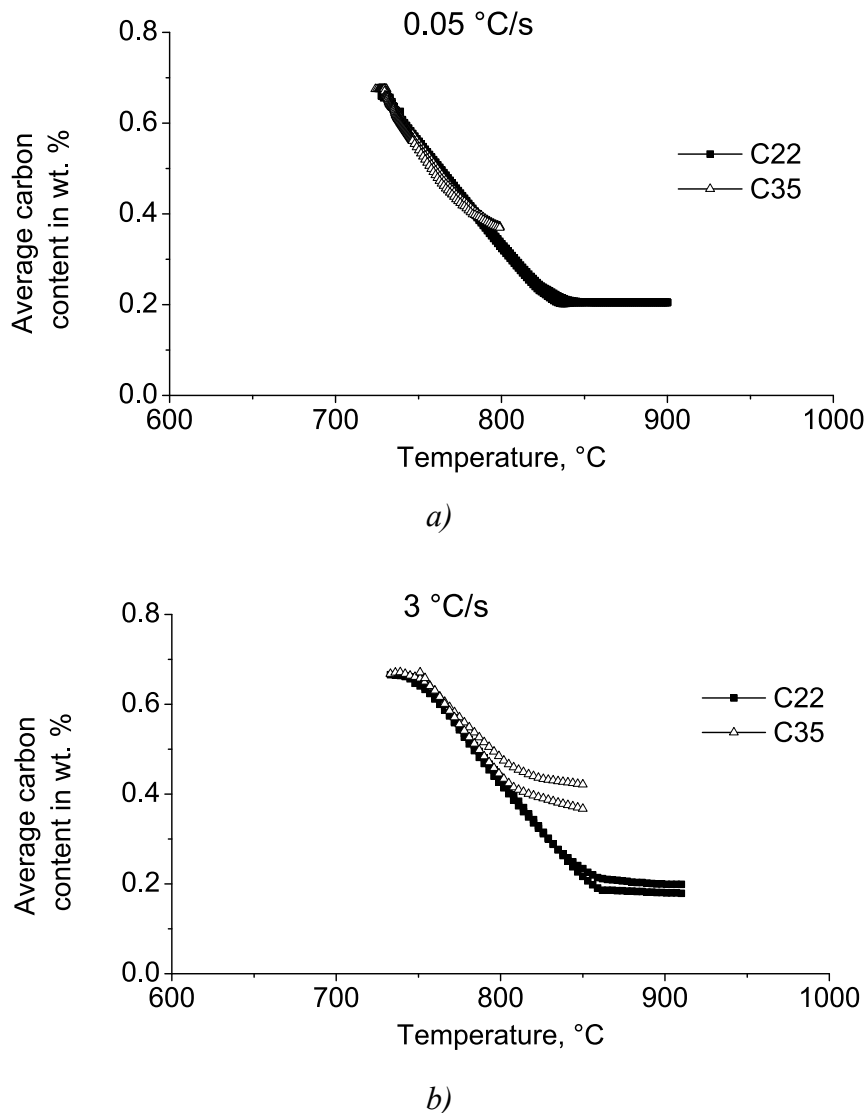


Figure 6.14. Average carbon content in austenite grains with growth type A. Open triangles are for C35 and solid rectangles for C22 alloys. The heating rates are: a) 0.05 and b) 3 °C/s. Individual lines correspond to different austenite grains.

As was already mentioned, growth type B (with growth kinetics II, slow, possible austenite nucleation on ferrite-ferrite grain boundaries) as well as the growth

type C (with growth kinetics III, massive growth) were not reproduced during the simulations. This is probably related to the following reasons. First of all, as will be described later in detail in chapter 8, on a smaller scale (nucleus size) the effect of curvature (the term in round brackets in Eq. (6.2)) is overestimated. Within the current formulation it was chosen to correct the effect of the curvature is through reduction of the interfacial energies (see chapter 8). After some critical curvature radius is exceeded the curvature term is not critical anymore, and no correction is necessary. As during the simulations a constant value for interfacial energies was used, this could lead to the disappearance of austenite nuclei formed on the ferrite-ferrite grain boundaries. Secondly, the phase-field model is a simplified representation of the real microstructure. Effects like internal lamellar structure of pearlite, orientation of different grains, chemical inhomogeneities, grain boundary diffusion, defects, such as dislocations, as well as the redistribution of other than carbon alloying elements are not represented in the simulations. This can lead:

- to an insufficient carbon flow. Diffusion is proportional to the carbon gradient. In case of the simplified pearlite, the average carbon content of pearlite grain is 0.7 wt. %, where as in a real microstructure the carbon content of cementite phase is 6.7 wt. %. In addition, the grain boundary diffusion is not present in the current model, which is usually a factor of 10 faster than bulk diffusion.

- to a lower driving force for the transformation. Mn stabilizes the austenite phase, so less carbon is necessary to form stable nuclei.

Thirdly, the massive transformation cannot be reproduced in phase field model used in the current simulations. Massive transformation is closely related to the T_0 -temperature (the temperature at which the free energies of both phases at a given concentration, x_0 , are equal). If the concentration in the phase (ferrite) becomes higher than the x_0 -concentration, a massive transformation becomes possible in the real material. In phase-field modeling, however, the forming phase grows by increasing its weight in the interface volume elements, and the carbon concentration of the forming phase is given by the carbon concentration profile of the grain that is growing. The formation of a volume element of the growing grain with a completely “new” concentration is not possible, and therefore massive transformation will not take place.

6.5. Conclusions

The current model is able to describe qualitatively and quantitatively the pearlite+ferrite-to-austenite transformation during continuous heating. The representation of the pearlitic structure as one uniform phase with average carbon content equal to the eutectoid composition as well as the assumption of para-equilibrium condition during the whole transformation range is a justifiable approximation for 3 °C/s heating rate. For low heating rate (0.05 °C/s) such an assumption leads to the discrepancy between the experimental and simulated curve for the pearlite-to-austenite part of the transformation, which is corrected by the lower

value of the pre-exponential mobility factor (μ_0). The derived carbon profiles show a transition from a homogeneous to inhomogeneous carbon redistribution with increasing heating rate. The refinement of the microstructure with increasing the heating rate is also well captured by the model. Not all from the experimentally observed single grain growth types were reproduced in the simulations. This can be related to the simplification implied in the current model as well as some limitations of the phase-field approach.

References

- [1] D. Raabe, F. Roters, F. Barlat, L.Q. Chen, 2004, *Continuum scale simulation of engineering materials*, Wiley-VCH Verlag GmbH & Co. KgaA, Weinheim.
- [2] L.Q. Chen, C. Wolverton, V. Vaithyanathan, Z.K. Liu, *Mrs Bulletin*, 2001, vol. 26, no. 3, pp. 197-202.
- [3] I. Steinbach, F. Pezolla, B. Nestler, M. Seeßelberg, R. Pieler, G. J. Schmitz *et al.*, *Physica D*, 1996, vol. 94 pp. 135-147.
- [4] I. Steinbach, In: *Advances in materials theory and modelling: bridging over multiple length and time scales*. San Francisco (CA): MRS; 2001. p. AA7.14.
- [5] L.Q. Chen, Y.Z. Wang, *J. Minerals Metal. & Mater Soc.*, 1998, vol. 108, n. 2-3, pp. 13-18.
- [6] A. Karma, Phase field methods, *Encyclopedia of Materials Science and Technology*. B. K. H. J., R. W. Cahn, M. C. Flemings *et al.*, Oxford, Elsevier, 2001, vol. 7, pp. 6873-86.
- [7] S.G. Kim, W.T. Kim, T. Suzuki, *Physical Review E*, 1999, vol. 60, n. 6, pp. 7186-7197.
- [8] A.A. Wheeler, W.J. Boettinger, G.B. McFadden, *Physical Review A*, 1992, vol. 45, no. 10, pp. 7424-7440.
- [9] L.Q. Chen, *Annu. Rev. Mater. Res.*, 2002, vol. 32, pp. 113-140.
- [10] R.G. Thiessen, I.M. Richardson, J. Sietsma, *Mater. Sci. and Eng. A*, 2006, v. 427, pp. 223-231.
- [11] J. Tieden, B. Nestler, H. J. Diepers, I. Steinbach, *Physica D*, 1998, vol. 115, pp. 73-86.
- [12] J.W. Christian, *The theory of transformations in metals and alloys*, Amsterdam: Pergamon, 2002.
- [13] B. Sundman, B. Jansson, J.-O. Andrésson, The Thermo-Calc databank system, *CALPHAD* 9, 1985, pp. 153-190.
- [14] M. G. Mecozzi, Phase-field modeling of the austenite to ferrite transformation in steels, Thesis, 2006, p. 161.
- [15] MICRESS®, Software developed in ACCESS is an independent research center associated with the Technical University of Aachen.
- [16] L. Murr, *Interfacial phenomena in metals and alloys*, Addison-Wesley, Reading, Massachusetts, 1975.

- [17] *Handbook of chemistry and physics*. Boca Raton (FL): CRC Press; 1989.
- [18] M. Militzer, M.G. Meozzi, J. Sietsma, S. van der Zwaag, *Acta Mater.*, 2006, vol. 54, pp. 3961-3972.
- [19] F. Fazeli, M. Militzer, *Metal. Mater. Trans.*, 2005, vol. 36A, pp. 1395-1405.
- [20] M. Hillert, *Phase equilibria, phase diagrams and phase transformations, Their thermodynamic bases*, Second addition, Cambridge University press, Cambridge, UK, 2008, p. 510.
- [21] M. Enomoto, *Acta Mater.*, 1999, vol. 47, no. 13, pp. 3533-3540.
- [22] K. Oi, C. Lux, G.R. Purdy, *Acta Mater.*, 2000, vol. 48, pp. 2147-2155.
- [23] M. Hillert, *Scripta Mater.*, 2002, vol. 46, pp. 447-453.

Chapter 7

Carbon redistribution during continuous heating of the pearlite-ferrite microstructure

Abstract

In this chapter the model that was built in chapter 6 is extended to a higher heating rate (50 °C/s) for the C22 and C35 alloys and the carbon redistribution during continuous heating is analyzed in more detail. It is shown that with increasing heating rate carbon is more inhomogeneously distributed in the austenite phase that is formed. The amount of carbon in austenite grains at high heating rates can vary from approximately 0.7 wt. % (former pearlite areas) to almost 0 wt. % (former pro-eutectoid ferrite areas). The overlap in the pearlite-to-austenite and ferrite-to-austenite transformations is also more pronounced at higher heating rates. The evolution of the carbon content on the austenite-ferrite interface during the transformation shows a change in the transformation mode with increasing heating rate. At low heating rates the diffusion-controlled mode can best describe the transformation kinetics. With increasing heating rate the amount of carbon on the austenite-ferrite interface shifts towards the interface-controlled mode and the transformation kinetics can be best described with the mixed-mode approach.

7.1. Introduction

As was shown in the previous chapters, after pearlite-to-austenite transformation is completed austenite will proceed to grow further into pro-eutectoid ferrite. In order for the interface to stay at equilibrium, long-range diffusion of carbon has to take place [1, 2]. Thus, the kinetics of ferrite-to-austenite transformation will be controlled by the diffusion of carbon; in other words, the diffusion process is the rate determining and the “local equilibrium” will prevail at the moving interface [3]. Schmidt *et al.* [4, 5] who studied the austenite formation from a ferrite-pearlite microstructure during continuous heating using hot-stage confocal microscopy, indeed observed that at low heating rates the formation of austenite is controlled by long-range diffusion of carbon. However, at higher heating rates under certain condition (above T_0 temperature) the growth rate increased drastically and the interface reaction-controlled growth mechanism is claimed to be responsible for the transformation. Thus, results appear to suggest that just the use of the mechanism of long-range diffusion of carbon for different heating conditions might not be accurate and the change from diffusion-controlled to interface-controlled transformation can be expected during austenitization of steels with the pearlite-ferrite microstructure. The conservative motion of interface under partitionless condition (the interface reaction-controlled growth) will result in a formation of austenite with lower (than equilibrium) carbon content.

So far, austenitization was studied using metallography [1, 6-8], electron microscopy [4], dilatometry [9-13], X-ray diffraction microscopy [14], neutron diffraction [15], hot-stage confocal microscopy [4, 5]. Using the above-mentioned techniques it is possible to study the microstructural evolution and kinetics of the austenite formation, the average amount of carbon in the forming austenite phase or the movement of the different boundaries (pearlite-austenite and ferrite-austenite). However, none of the techniques gives an answer over the amount of carbon on the ferrite-austenite interfaces during continuous heating, which is indicative of the character of the transformation.

Different models of austenitization [11, 16-21] that have been proposed in the literature are also not able to predict the amount of carbon on the moving interface during continuous heating of the pearlite+ferrite microstructure. By knowing the amount of carbon on the interface during the transformation it is possible to make conclusions on the governing mechanism of austenite formation (diffusion-controlled, interface-controlled or mixed-mode).

This chapter presents the results on the modeled carbon redistribution during continuous heating of the pearlite-ferrite initial microstructure. The model for austenite formation using the phase-field approach was already described in chapter 6. In the current chapter, the carbon redistribution during the continuous heating of C35 alloy is analyzed for 0.05, 3 and 50 °C/s heating rates. A clear shift from the diffusion-controlled character of the transformation at low heating rates to a mixed-mode character at high heating rates is obtained.

7.2. Simulation conditions

A two-dimensional phase-field simulation of the continuous heating of the C22 and C35 alloys were performed using the MICRESS[®] code [22]. The detailed description of the model as well as the input parameters were already described in chapter 6. The chemical composition of the studied alloy as well as the initial optical microstructure and the equivalent simulated microstructures are given in chapters 3 and 6. In addition to the simulations described in chapter 6, where alloys were continuously heated with 0.05 and 3 °C/s heating rates, in this chapter the studied heating rates were extended to 50 °C/s.

The carbon content on the austenite-ferrite grain boundary is determined as the average carbon content over all the ferrite-austenite interface volume elements. The concentration of carbon in austenite on the ferrite-austenite interface, x_γ , was calculated for $0.35 < \varphi_i < 0.65$, as described in chapter 6, section 6.2.1 (see Fig. 6.2).

7.3. Results and discussion

Figure 7.1 shows the evolution of the microstructure at approximately half of the transformation (when all pearlite is transformed to austenite, *a*, *b* and *c*) and at the end of the transformation (when only austenite phase is present, *d* and *e*) for 50 °C/s heating rate. For 0.05 and 3 °C/s the equivalent figures were already presented in chapter 6 (see Figs. 6.9-6.12). Pearlite, due to a very short carbon diffusion distances and a lot of ferrite-cementite surface area, feels large driving force to transform to austenite. It transforms to austenite rather quickly in comparison to the pro-eutectoid ferrite phase. It is in a good agreement with the previous work [1, 6, 7, 11, 15, 23].

Figure 7.2 shows an example of an austenite grain that grows into the pearlite and ferrite grains. The example is given for 3 °C/s heating rate, for 0.05 and 50 °C/s the tendencies will hold, however the overlap between the pearlite-to-austenite and ferrite-to-austenite transformations will be bigger for the higher heating rates (see also Fig. 7.3).

When austenite nucleus is formed on the ferrite-pearlite grain boundary, two interfaces are created: pearlite-austenite and ferrite-austenite. Both interfaces will move as the transformation proceeds, however, with different velocities. As the rate at which each interface moves will be determined by how quickly carbon can be supplied to the moving boundary, the pearlite-austenite interface, in general, will move much faster in comparison to the ferrite-austenite interface. Pearlite grains are the sources of carbon, so no diffusion is required towards the pearlite-austenite interface as it is already present there.

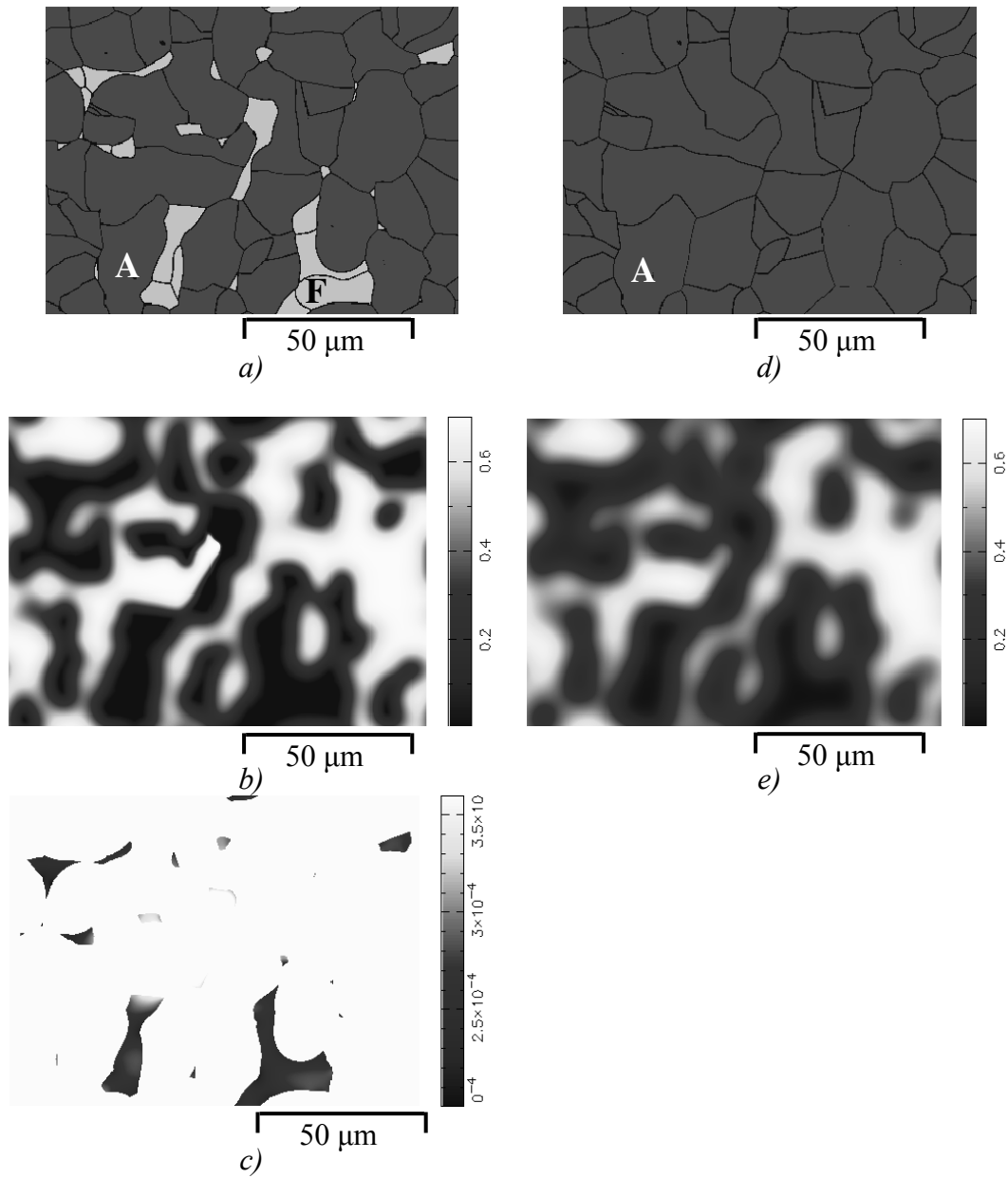


Figure 7.1. The evolution of the microstructure for the C35 alloy heated with 50 °C/s heating rate to a)-c) 850 °C and d)-e) 900 °C.

a), d) show microstructures; b), e) show carbon profiles; c) shows carbon gradients in the ferrite phase. A = austenite, F = ferrite.

For the color version refer to the appendix.

For the ferrite-austenite interface, on contrary, carbon has to diffuse through the austenite phase, thus the transformation will mostly be controlled by how quickly

carbon can reach the moving interface. At low heating rate (0.05 °C/s) the pearlite-austenite interface will move about 50 times faster than the ferrite-austenite interface. As the pearlite-austenite interface moves significantly faster, the growing austenite grains will first consume the pearlite grains. After some time, this will lead to the formation of a two-phase ferrite-austenite structure, where the carbon distribution in austenite is homogeneous, since it is inherited from pearlite.

At higher heating rates, 3 and 50 °C/s, the ratio in interface velocities (v_p/v_a) will decrease to about 20 and 5 times, respectively. This indicates that, especially for 50 °C/s, both interfaces, pearlite-austenite and ferrite-austenite, will move almost with the same velocities and the newly formed austenite grains will grow simultaneously into two grains – pearlite and ferrite. This leads to more pronounced carbon gradients in austenite (see Figs. 6.11 a,c, 6.12 a,c and 7.1 b,e). At such a high heating rate the diffusion of carbon cannot keep up with the movement of the ferrite-austenite interface, so a more inhomogeneous austenite is formed.

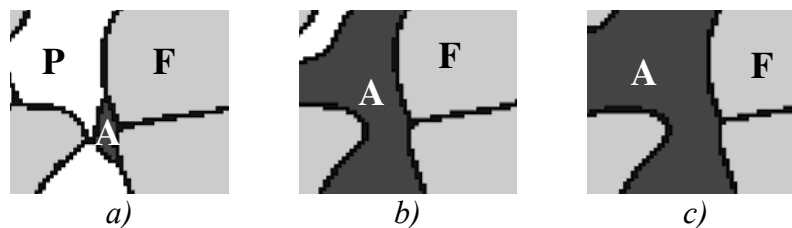


Figure 7.2. Austenite grain growth at different time steps: a) t_1 , b) t_2 , c) t_3 ($t_1 < t_2 < t_3$).

The carbon content in ferrite also shows some variations in the concentration, which are more pronounced at higher heating rate (50 °C/s), compare Figs. 6.11 b, 6.12 b, 7.1c. As the driving force for the transformation depends on the local composition, the ferrite-austenite interfaces with higher carbon content will feel higher driving force and will move faster thus promoting further formation of austenite that is inhomogeneous in terms of its carbon content. At the end of the transformation (see Fig. 7.1d, e) strongly inhomogeneous austenitic phase is formed in which carbon varies from approximately 0.7 wt. % (former pearlite regions) to almost 0.004 wt. % (former pro-eutectoid ferrite regions). This is an important observation as such strong carbon fluctuations can lead to the formation of different phases upon cooling (martensite, bainite, ferrite *etc.*, see also chapter 4).

Figure 7.4 shows the carbon concentration profiles for C35 alloy for three different heating rates: 0.05, 3 and 50 °C/s and at three different temperatures. The chosen temperatures correspond to the temperatures at which the slope of austenite fraction curve changes from steep (pearlite-to-austenite part of the transformation) to

generally sloping (ferrite-to-austenite part of the transformation). A remarkable change in the behavior of the carbon concentration profile is observed.

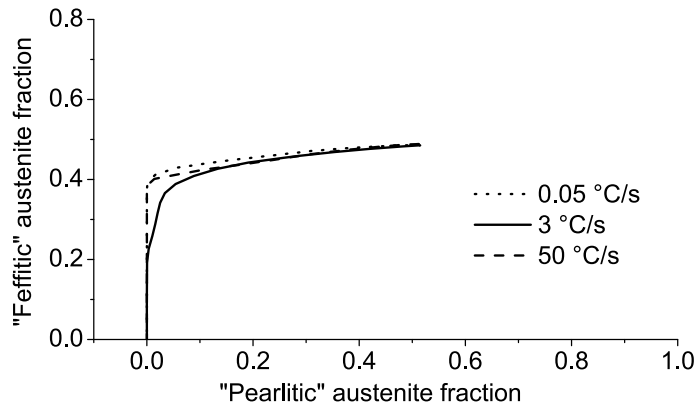


Figure 7.3. Overlap between pearlite-to-austenite and ferrite-to-austenite volume fractions for C35 alloy. Dot line is for 0.05 °C/s, Solid line is for 3 °C/s and dash line is for 50 °C/s heating rates.

At 0.05 °C/s there is hardly any concentration gradient present in the austenite phase. The situation changes with increasing the heating rate. At 3 °C/s heating rate there is already a carbon concentration gradient developed in the microstructure: there is more carbon in the center of the austenite grain and less at the interface. At 50 °C/s heating rate the carbon concentration gradient is even more pronounced and austenite with a highly inhomogeneous carbon content is formed.

Figure 7.5 shows the average carbon content at the ferrite-austenite grain boundary as a function of temperature for three different heating rates. The curves show the steady decrease in the amount of carbon at the ferrite-austenite interface with the progress of the transformation. This decrease is related both to the increase in the austenite volume fraction and the increase in the temperature. The equilibrium value of carbon for each temperature (which is described by the diffusion controlled mode) is also presented in Fig. 7.5 (solid triangles). Diffusion-controlled transformations imply that the mobility of the interface is infinite, local equilibrium at the interface is present at all times and the transformation is controlled purely by the rate of carbon diffusion, e.g. the interface moves as fast as diffusion of carbon allows. Along with the equilibrium values, the carbon concentration values as calculated by Eq. 7.1 are also shown in Fig. 7.5 (stars). In this case the austenite phase is allowed to grow as fast as the iron atoms can cross the ferrite-austenite interface.

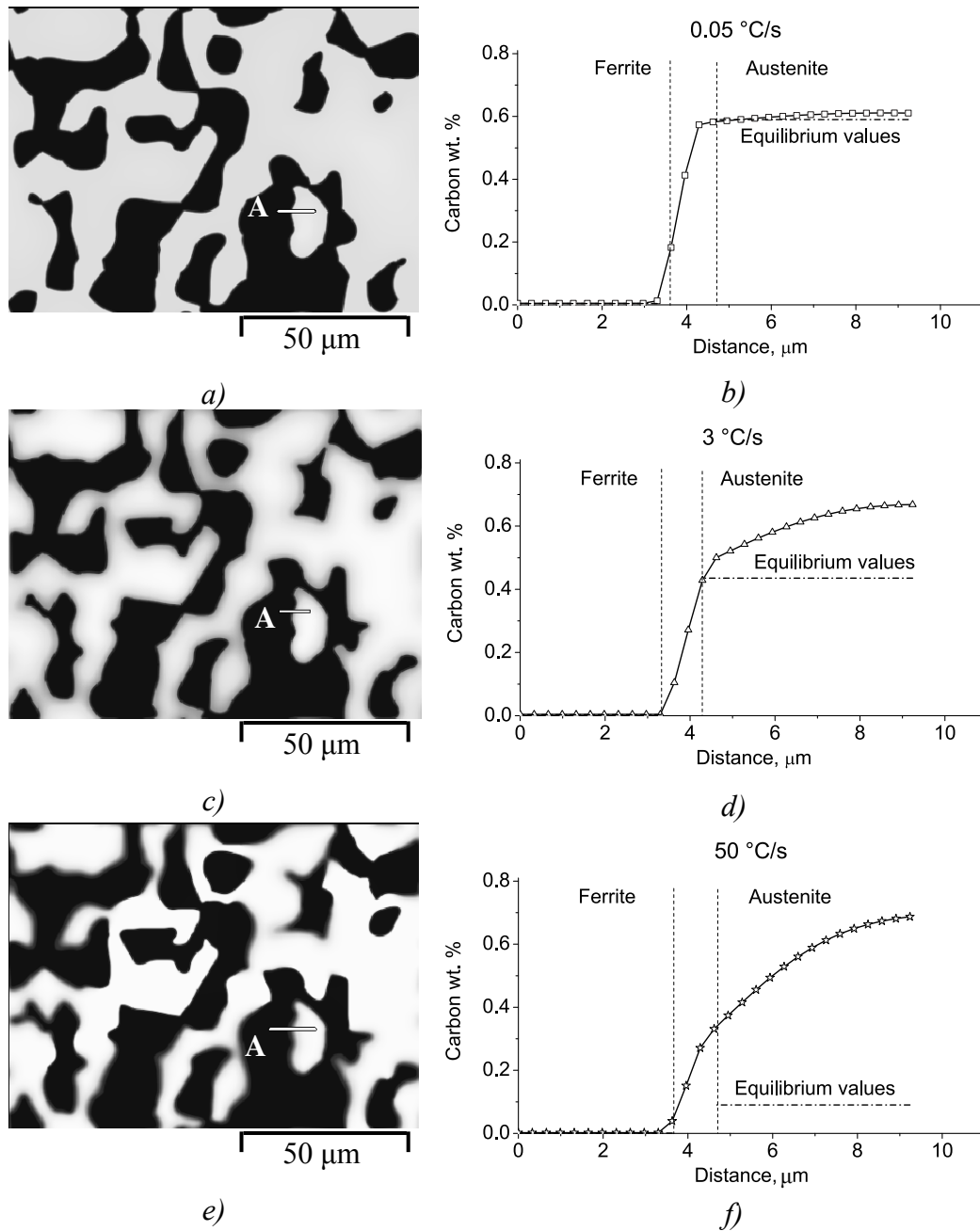


Figure 7.4. Carbon concentration maps a), c), e) and carbon profiles along the line A b), d), f) for C35 alloy at a), b) 745 °C; c), d) 762 °C and e), f) 812 °C. In a), b) alloy was heated with 0.05 °C/s; c), d) 3 °C/s and e), f) 50 °C/s heating rate. For the color version refer to the appendix.

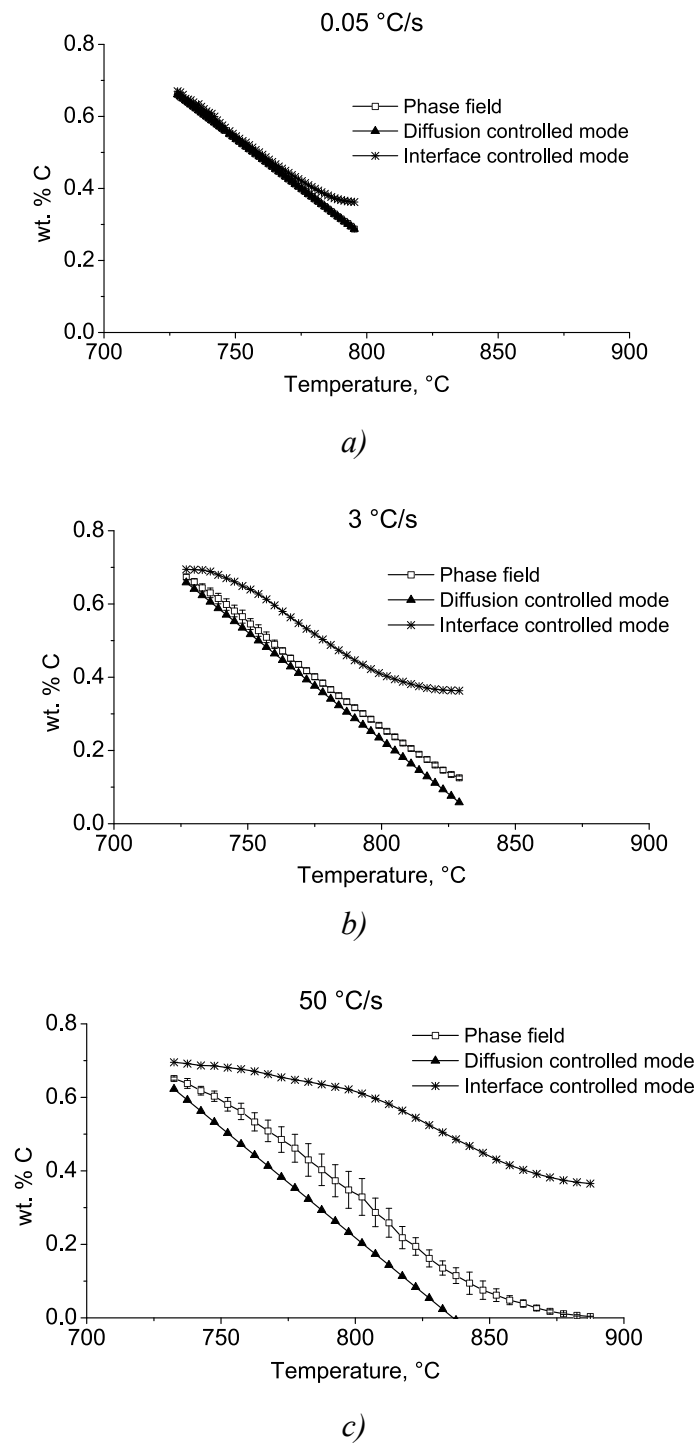


Figure 7.5. Carbon distribution on the ferrite-austenite grain boundary at different heating rates: a) 0.05, b) 3 and c) 50 °C/s; phase-field simulations (open rectangles), and carbon content at the interface as calculated by the diffusion controlled (solid triangles) and interface controlled models (stars).

The carbon concentration in austenite at the ferrite-austenite interface as predicted by the interface-controlled model is given by:

$$x_{\gamma\alpha}^{IC} = \frac{x_0 - (f^\alpha x_{\alpha\gamma}^{Ceq} + f^P x_{p\gamma}^{Ceq})}{1 - (f^\alpha + f^P)}, \quad (7.1)$$

where x_0 is the average carbon content in the alloy,

f^α and f^P are the ferrite and pearlite fractions from the phase-field simulations,
 $x_{\alpha\gamma}^{Ceq}$ and $x_{p\gamma}^{Ceq}$ are the carbon content in ferrite and pearlite in equilibrium with γ
as determined from the equilibrium phase diagram. The carbon content in pearlite is taken to be 0.7 wt. % and does not change during the transformation.

At low heating rate (0.05 °C/s) the amount of carbon at the austenite-ferrite interface follows the diffusion- and interface-controlled model during almost the whole transformation range, which means that the transformation evolves practically in equilibrium. For 3 °C/s heating rate the amount of carbon in austenite at the ferrite-austenite interface fairly closely follows the diffusion-controlled mode, at 50 °C/s heating rate, however, there is a clear shift from the diffusion-controlled towards the interface-controlled mode with increasing temperature. As the austenite grains grow the transformation evolves towards the mixed-mode character. The error bars in Fig. 7.5 also show that at 0.05 and 3 °C/s heating rates the variation in carbon concentration in austenite on the austenite-ferrite interface is small. For 50 °C/s heating rate, especially in the middle temperature range, there is a strong variation in carbon concentration on the interface. This will result in a variation in the interface velocities as the velocity of the interface is directly related to the carbon content through the driving force. It is interesting to notice, that such a change in transformation kinetics (from diffusion-controlled to mixed-mode) is different from the movement of the same ferrite-austenite interface but upon cooling. As was shown by Mecozzi *et al.* [24], at low cooling rate (0.05 °C/s) the movement of the ferrite-austenite interface follows the interface-controlled model. At high cooling rate (10 °C/s), however, the actual carbon content at the initial stages is quite close to the interface-controlled model, but shifts towards the mixed-mode as the transformation proceeds. The change in transformation mode is related to the ability of carbon to diffuse: at early stage, the small amount of carbon atoms rejected from the ferrite phase can easily diffuse into the bulk of austenite and the lattice transformation is rate-determining. As the ferrite grains grow, the amount of carbon rejected from ferrite increases and the carbon diffusivity in the bulk becomes also important, so the transformation has more of a mixed-mode character.

The situation upon heating is somewhat different. It is complicated by the presence of two phases in the initial microstructure – ferrite and pearlite with different carbon concentrations. Upon heating such a microstructure above the eutectoid temperature, austenite grains are formed on the pearlite-ferrite grain boundaries and

the ferrite-austenite and pearlite-austenite interfaces are created. The first austenite nuclei have eutectoid composition as the diffusion distances are rather small (see Fig. 7.6a). Upon further heating depending on the heating rate two scenarios are possible:

- at low heating rate it can be assumed that the pearlite-austenite interface will move first and the pearlite phase will be consumed before the ferrite-to-austenite transformation starts. This assumption is based on a much higher velocity of the pearlite-austenite interface which was estimated to be 50 times higher comparing to the ferrite-austenite interface (see section 7.3). Austenite will inherit the carbon content from the pearlite phase ($x_{\gamma p}^{Ceq} = x_p^C$, see Fig. 7.6b). The position of the austenite-ferrite interface will not change ($z_{\gamma\alpha}^0$). After this transformation is completed, the ferrite-to-austenite transformation will start. Due to low heating rates, and thus relatively long time that alloy spends on each temperature the distribution of carbon will have enough time to homogenize and reach the equilibrium value (at the interface and inside the grain).

- at high heating rate, due to smaller differences in interfacial velocities, it can be assumed that both the pearlite-austenite and ferrite-austenite interfaces will start to move simultaneously, though with different velocities ($z_{\gamma p}^1 \neq z_{\gamma p}^0$ and $z_{\gamma\alpha}^1 \neq z_{\gamma\alpha}^0$, see Fig. 7.6c). The amount of carbon necessary to create a new volume of austenite (area *C* on Fig. 7.6c) has to be removed from the areas rich in carbon (area *B*). Due to high heating rates the system will not have enough time to homogenize carbon within the austenite grain, thus a carbon gradient will develop. This gradient will be directly proportional to the heating rate and temperature, e.g. with increasing heating rate as well as going to higher temperatures the carbon differences within the austenite phase will increase. The higher differences in the carbon concentrations will promote diffusion as the flux of diffusing element is directly proportional to the concentration difference. This will accelerate carbon diffusion, thus reducing the effect of carbon redistribution on the transformation kinetics (diffusion control) and the system will shift into the mixed-mode.

The change in the transformation mode from the diffusion-controlled into mixed-mode (i.e. towards the interface-controlled mode) with increasing heating rate is an interesting outcome of this work. It implies that most of the models that were developed to describe the ferrite-to-austenite transformation upon continuous heating under the assumption that the transformation is controlled by the diffusion of carbon in austenite are not valid for relatively high heating rates, which are of interest for the practical point of view for the industry.

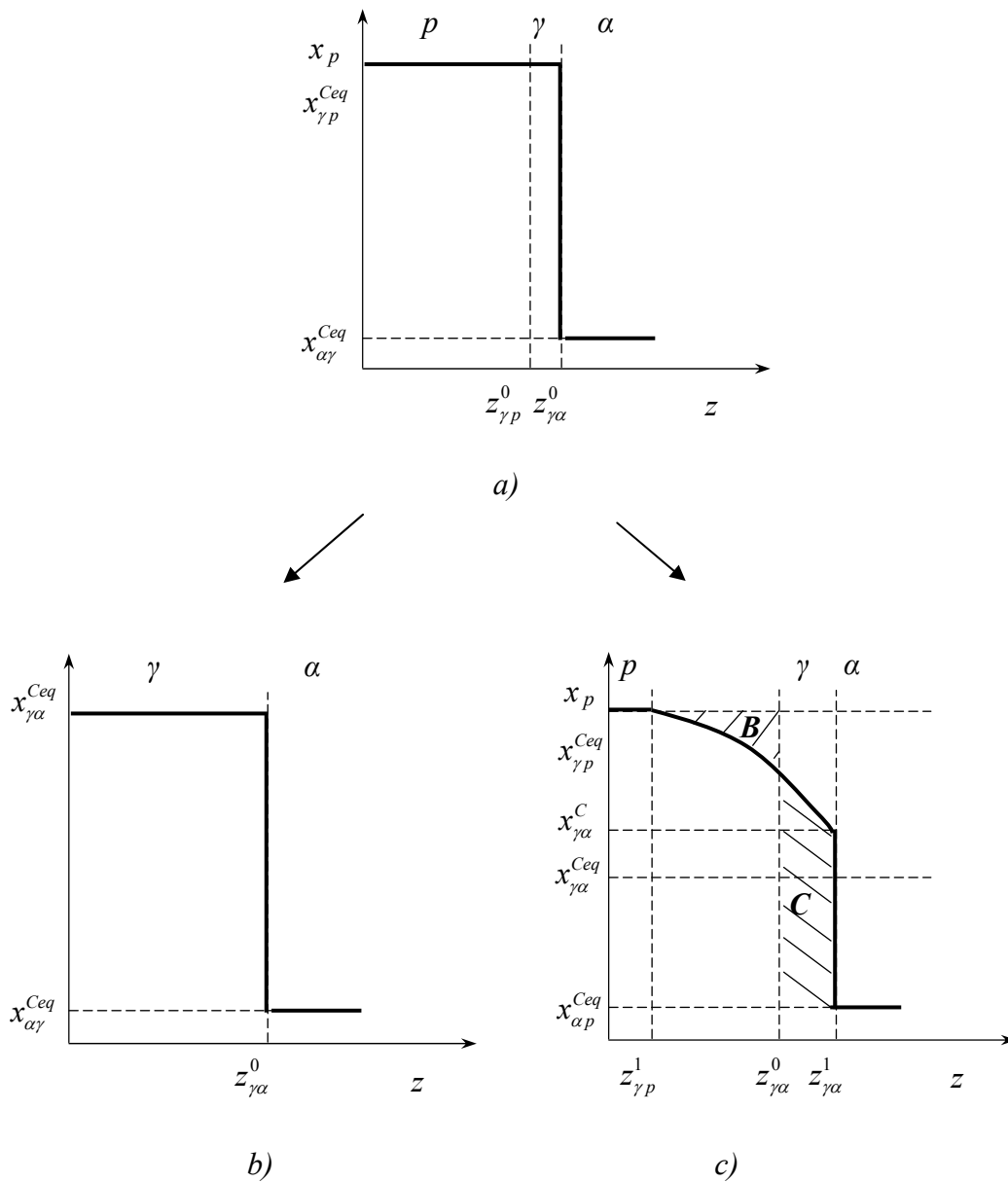


Figure 7.6. Schematic view of the variation of the carbon content across the pearlite-austenite-ferrite boundary for the alloy heated with b) low and c) high heating rate. a) shows austenite nucleus on pearlite-ferrite interface (starting situation). α = ferrite, γ = austenite and p = pearlite.

7.4. Conclusions

It was shown that at low heating rates the ferrite-to-austenite transformation kinetics can be described by the diffusion-controlled model. At higher heating rate (50 ° C/s) there is a clear shift in the direction of the interface-controlled mode. This is related to first of all less time available for carbon redistribution and secondly, to the sharper concentration gradients, which intensify the flux of carbon atoms. Thus the assumption of the local equilibrium condition at the interface, as assumed by the diffusion-controlled model, cannot be justified for all the heating rates.

The overlap in the pearlite-to-austenite and ferrite-to-austenite is more pronounced at higher heating rates. The degree of overlap is directly proportional to the heating rate.

References

- [1] G. R. Speich, V. A. Damarest, R.L. Miller, *Metall. Trans.*, 1981, vol. 12A, p. 1419-1428.
- [2] F.G. Caballero, D. San Martin, C. Capdevila, A. Garcia-Junceda, C. Garcia de Andres, *Solid-to-Solid Phase Transformations in Inorganic Materials*, 2005, vol. 1: *Diffusional Transformations*. vol. 1, pp. 707-712.
- [3] C.J. Zener, *J. Appl. Phys.*, 1949, vol. 20, pp. 950-953.
- [4] E. Schmidt, Y. Wang, S. Sridhar, *Metall. Mater. Trans. A*, 2006, vol. 37A, pp. 1799-1810.
- [5] E. D. Schmidt, E. B. Damm, S. Sridhar, *Metall. Mater. Trans. A*, 2007, vol. 38A, pp. 244-260.
- [6] G.A. Roberts, R.F. Mehl, *Trans. ASM*, 1943, vol. 31, p.613-650.
- [7] D.P. Datta, A.M. Gokhale, *Metall. Trans. A*, 1981, vol. 12A, pp. 443-450.
- [8] C.I. Garcia, A.J. DeArdo, *Metall. Mater. Trans. A*, 1984, vol. 12A, pp. 521-530.
- [9] R.C. Dykhuizen, C.V. Robino, G.A. Knorovsky, *Metall. Mater. Trans. B*, 1999, vol. 30B, pp. 107-117.
- [10] C. Garcia de Andrés, F.G. Caballero, C. Capdevila, *Scripta Mater.*, 1998, vol. 39, no. 6, pp. 791-796.
- [11] F.G. Caballero, C. Capdevila, C. Garcia de Andrés, *ISIJ Intern.*, 2001, vol. 41, no. 10, pp. 1093-1102.
- [12] F.G. Caballero, C. Capdevila, C. Garcia de Andrés, *Mater. Sci. and Tech.*, 2001, vol. 17, pp. 1114-1118.
- [13] C. Garcia de Andrés, F.G. Caballero, C. Capdevila, *Scripta Mater.*, 1998, vol. 38, no. 12, pp. 1835-1842.
- [14] T.A. Palmer, J.W. Elmer, *Scripta Mater.*, 2005, vol. 53, pp. 535-540.
- [15] R.C. Reed, T. Akbay, Z. Shen, J.M. Robinson, J.H. Root, *Mater. Sci. Eng. A*, 1998, vol. 256, pp. 152-165.
- [16] A. Jacot, M. Rappaz, *Acta Mater.*, 1999, vol. 47, no. 5, pp. 1645-1651.
- [17] T. Akbay, R.C. Reed, C. Atkinson, *Acta Metall.*, 1994, vol. 47, pp. 1469.

- [18] C. Atkinson, T. Akbay, R.C. Reed, *Acta Metall.*, 1995, vol. 43, pp. 2013.
- [19] D. Gaude-Fugarolas, H.K.D.H. Bhadeshia, *J. Mater. Sci.*, 2003, vol. 38, pp.1195-1201.
- [24] J.W. Elmer, T.A. Palmer, W. Zhang, B. Wood, T. Debroy, *Acta Mater.*, 2003, vol. 51, pp. 3333-3349.
- [20] L. Gavard, H.K.D.H. Bhadeshia, D.J.C. Mackay, S. Suzuki, *Mater. Sci and Techn.*, 1996, vol. 12, pp. 453-463.
- [21] C.A.L. Bailer-Jones, H.K.D.H. Bhadeshia, D.J.C. Mackay, *Mater. Sci and Techn.*, 2001, vol. 15, pp. 287-294.
- [22] MICRESS[®], Software developed in ACCESS is an independent research center associated with the Technical University of Aachen.
- [23] C.R. Brooks: *Principles of The Austenitization of Steels*, Elsevier Applied Science, London, UK, 1992, pp. 81-144.
- [24] M.G. Mecozzi, J. Sietsma, S. van der Zwaag, M. Apel, P. Schaffnit, I. Steinbach, *Metall. Mater. Trans. A*, 2005, vol. 36A, September, pp. 2327-2340.

Chapter 8

Detailed phase-field modeling of austenite growth in a ferrite-pearlite structure

Abstract

In this chapter the growth of austenite grains near a source of carbon (at the pearlite-ferrite and ferrite-cementite boundaries) and away from a source of carbon (at the ferrite-ferrite boundaries) is modeled in detail using a phase-field approach. It is shown that the interface velocity of the austenite-ferrite interfaces strongly depends on the local conditions, e.g. the way in which carbon redistribution can take place. The austenite-ferrite interface moves almost 10 times faster into the pearlite grain than into the pro-eutectoid ferrite grain. Even within the pearlite grain the growth velocity of the austenite-ferrite interface is not uniform and depends on the position of the cementite lamellae being the source of carbon. The growth of austenite grains away from the source of carbon mostly depends on how quickly the carbon can be transported and on the local concentration patterns.

8.1. Introduction

Austenite nucleation in the ferrite-pearlite microstructures was already discussed in previous chapters. It was shown that the most favorable places for austenite nucleation are the pearlite-pearlite and pearlite-ferrite grain boundaries. They are attractive places because they are high-energy boundaries and because the presence of carbon makes the newly formed austenite nuclei stable. In chapter 4 it was shown that nucleation on the ferrite-ferrite grain boundaries can also take place in the early stages of the transformation (when the pearlite phase is still present in the microstructure). The austenite nuclei formed on those grain boundaries had a carbon concentration lower than equilibrium, but higher than the concentration of carbon in the ferrite phase. Further, in chapter 5 it was shown that the growth rate of those metastable nuclei was much lower than that of the austenite nucleated near the source of carbon (pearlite phase). In chapter 6 the phase-field model for the pearlite+ferrite-to-austenite transformation during continuous heating, however, failed to reproduce this type of growth. It was argued that the simplifications applied in the model as well as some limitations of the MICRESS[®] software can be responsible for that.

The aim of the current simulation is to investigate austenite growth at different locations taking into account the lamellar structure of the pearlite: near the source of carbon, the pearlite-ferrite and ferrite-cementite boundaries, and away from the source of carbon, the ferrite-ferrite grain boundary. The carbon evolution during the transformation for each grain and for the microstructure in general is of high interest since it determines behavior and growth rates at different locations.

8.2. Simulation conditions

A two-dimensional phase-field simulation of isothermal holding at 727 °C (above the eutectoid temperature) of an Fe-C alloy with a pearlite-ferrite microstructure were performed using the MICRESS[®] code [1].

The model developed in chapter 6 with governing Eqs. (6.2) and (6.5) was used in the current simulations, with the uniform pearlite being substituted with the real phases – ferrite and cementite. Pearlite was modeled explicitly with the ferrite-cementite lamellae (see Fig. 8.1). Four different locations were tested:

- austenite growth near the source of carbon:
 - a) on the pearlite-ferrite grain boundary, grain γ_1 ;
 - b) inside the pearlite grain on the ferrite-cementite interface, grain γ_2 .
- austenite growth away from the source of carbon:
 - c) on the ferrite-ferrite grain boundary, grain γ_3 ;
 - d) on the triple point, grain γ_4 .

The starting carbon concentration of the austenite nuclei was set to be equal to the experimentally measured value of $x_\gamma = 0.27$ % wt. (see chapter 4.4.1, Fig. 4.5). The carbon content of the ferrite and cementite phases was taken to be equal to $x_\alpha^C = 0.01867$ wt. % (carbon concentration in ferrite that is in equilibrium with austenite at $T = 727$ °C) and $x_\theta^C = 6.7$ wt. % respectively. The cementite phase is considered to be a stoichiometric phase. The linearized phase diagram used in simulations is shown in Fig. 8.2. Diffusion data are summarized in Table 6.1. The diffusion parameters for the cementite phase do not play a role, since the cementite phase has a constant composition.

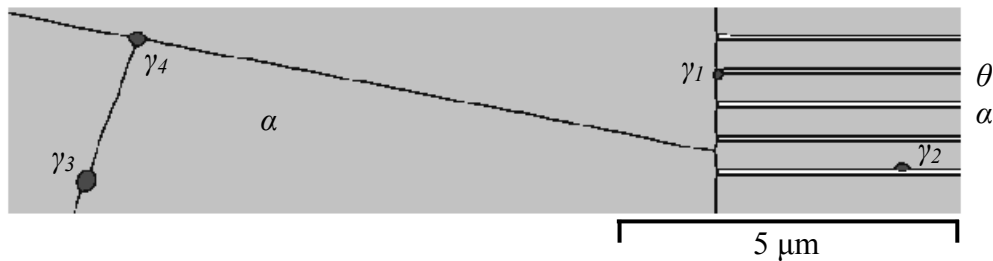


Figure 8.1. Initial simulated microstructure. α = ferrite, γ = austenite, θ = cementite.
 * Austenite growth near the source of carbon: on the pearlite-ferrite grain boundary, γ_1 , and inside the pearlite grain on the ferrite-cementite interface, γ_2 .
 ** Austenite growth away from the source of carbon: on the ferrite-ferrite grain boundary γ_3 , and triple point, γ_4 .

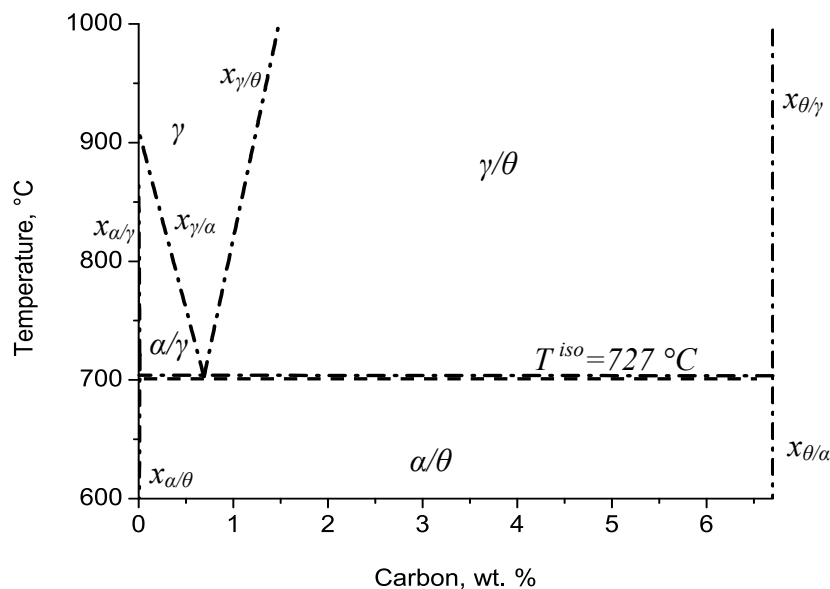


Figure 8.2. Linearized phase diagram used in calculations.

The mobilities of the $\gamma:\gamma$, $\gamma:\alpha$ and $\alpha:\alpha$ interfaces were treated individually as temperature dependent parameters, based on the lattice dimensions and calculated according to Eq. (6.3) and Tables 3.3, 6.2 and 6.3. The values for the activation energies for the $\gamma:\theta$ interface mobility is taken to be equal to the activation energy of the $\gamma:p$ interface mobility (see chapter 6, Table 6.3) and is equal to 150 kJ mol^{-1} . The mobility of the $\alpha:\theta$ interface is taken to be low as it is known to be a coherent interface. The interfacial energies are shown in Table 8.1.

Table 8.1. Interfacial energies as used in the simulations of the ferrite-cementite-austenite structure.

	$\gamma:\gamma$	$\gamma:\alpha$	$\gamma:\theta$	$\alpha:\alpha$	$\alpha:\theta$	$\theta:\theta$
$\sigma_{ij} (\text{J m}^{-2})$	0.76	0.39	0.94	0.5	1.05	1.25

The problem that rises with the simulations on a small scale is that within the current formalism the effect of the diffuse interface is significant and the curvature effect appears to be overestimated (the term in round brackets in Eq. (6.2)). It has been chosen in the current simulations to correct the curvature term in Eq. (6.2) by varying the interfacial energy. For this reason the further analysis is aimed at finding effective values for the interfacial energies, in other words, the correction for the curvature term.

In order to estimate the realistic value for the curvature term of Eq. (6.2) the following procedure was applied. The isothermal transformation of a ferrite-austenite microstructure at $847 \text{ }^\circ\text{C}$ was simulated (see Fig. 8.3). The carbon content in austenite was assumed to be higher than equilibrium (with ferrite) and varied from 0.3 to 0.7 wt. %. The carbon content in ferrite was taken to be equal to 0.01 wt. %. This is slightly higher than the α/γ -equilibrium value, which is equal to 0.0064 wt. %. All the relevant data (governing equations, diffusion coefficients, mobilities etc.) are taken as described above and in chapter 6.

At the simulation conditions as described above the final microstructure, as resulting from the thermodynamic calculations [2], should consist of a ferrite-austenite mixture, where the carbon content in the austenite phase is equal to 0.21 wt. %. Since the carbon content in the initial austenite grains as well as in the ferrite grains is higher than the equilibrium values, it is expected that the austenite grains grow into the ferrite grains, increasing the austenite volume fraction and simultaneously decreasing the average carbon content in the austenite and ferrite phases towards the equilibrium values of 0.21 and 0.0064 wt. % C respectively. However, if the interfacial energies from Table 6.2 are used, contrary to expectations, the austenite grains transform very quickly to ferrite, increasing the average carbon content in it to a value far above the equilibrium value. This indicates that the curvature term in Eq. (6.2) is too large and it is energetically more favorable for the

system to form a purely ferritic structure than to contain a ferrite-austenite mixture. To estimate more realistic values for the curvature term (in other words - interfacial energies) the following steps were taken.

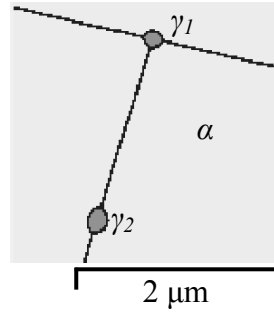


Figure 8.3. Initial microstructure used in simulations that are aimed at the estimation of the interfacial energies. Light – ferrite, dark – austenite.

The free energy of the simulated microstructure was estimated for two situations:

1. for the microstructure with only the ferrite phase;
2. for the ferrite-austenite mixture.

1. In the first case the free energy of the system, which contains only the ferrite phase with average carbon concentration, is equal to:

$$V_0 G_{\alpha}^{\text{system}} = V_{\alpha} \cdot G_{\alpha}(x_0^C) + A^{\alpha\alpha} \sigma^{\alpha\alpha}, \quad (8.1)$$

where V_{α} is the ferrite volume and in this case is equal to the total volume of the system, V_0 ,

$G_{\alpha}(x_0^C)$ is the Gibbs free energy per unit volume at the average carbon concentration,

$A^{\alpha\alpha}$ is the area of the ferrite-ferrite grain boundary with grain boundary with interfacial energy $\sigma_{\alpha\alpha}$.

2. In the second case, when the microstructure consists of a ferrite-austenite mixture, the free energy of the system is equal to:

$$V_0 G_{\gamma\alpha}^{\text{system}} = V_{\gamma} \cdot G_{\gamma}(x_{\gamma}^C) + V_{\alpha} \cdot G_{\alpha}(x_{\alpha}^{Ceq}) + A_{\gamma\alpha} \cdot \sigma_{\gamma\alpha} + A'_{\alpha\alpha} \cdot \sigma_{\alpha\alpha}, \quad (8.2)$$

where $G_\gamma(x_\gamma^C)$ is the Gibbs free energy per unit volume of the austenite phase at the tested composition;

$G_\alpha(x_\alpha^{Ceq})$ is the Gibbs free energy per unit volume of the ferrite phase at $x_\alpha^{Ceq}=0.0064$ wt. %;

V_γ and V_α are the volumes of austenite and ferrite grains and $A_{\alpha\alpha}$ and $A_{\gamma\alpha}$ are the interfacial areas for $\alpha\alpha$ and $\gamma\alpha$ interfaces respectively,

$$V_\gamma x_\gamma^C + V_\alpha x_\alpha^{Ceq} = V_0 x_0 \text{ and } A_{\gamma\alpha} + A'_{\alpha\alpha} > A_{\alpha\alpha}.$$

The ferrite-austenite microstructure contains more interfacial energy than the ferrite microstructure. On the other hand, the chemical free energy (the term $V_i \cdot G_i$) is smaller for the ferrite-austenite microstructure, to a degree that depends on the carbon content. Taking realistic values for the interfacial energies, the critical carbon content, being the carbon content for which both free energies for the whole system are equal, can be calculated.

On the next step, the grain boundary energies $\sigma_{\gamma\alpha}$ and $\sigma_{\alpha\alpha}$ for the phase field simulations were varied such that the critical carbon concentration value as calculated above for the real situation coincided the one for the phase-field approach. That led to a reduction coefficient for the interfacial energies of around 10, e.g. the interfacial energies for the phase-field approach had to be reduced by a factor 10 to give the same critical concentration value (see Table 8.2).

Table 8.2. Corrected interfacial energies as used in the simulations of the ferrite-cementite-austenite structure.

	$\gamma:\gamma$	$\gamma:\alpha$	$\gamma:\theta$	$\alpha:\alpha$	$\alpha:\theta$	$\theta:\theta$
σ_{ij} (J m ⁻²)	0.076	0.039	0.094	0.05	0.105	0.125

The last parameters that have to be mentioned are the node size, which was taken to be $\Delta x=0.023$ μm and interfacial thickness η , which is taken to be $\eta = 4\Delta x$ [3].

8.3. Results and discussion

Figures 8.4 and 8.5 show the evolution of the microstructure and carbon redistribution after 1 and 11 s of isothermal holding at 727 °C.

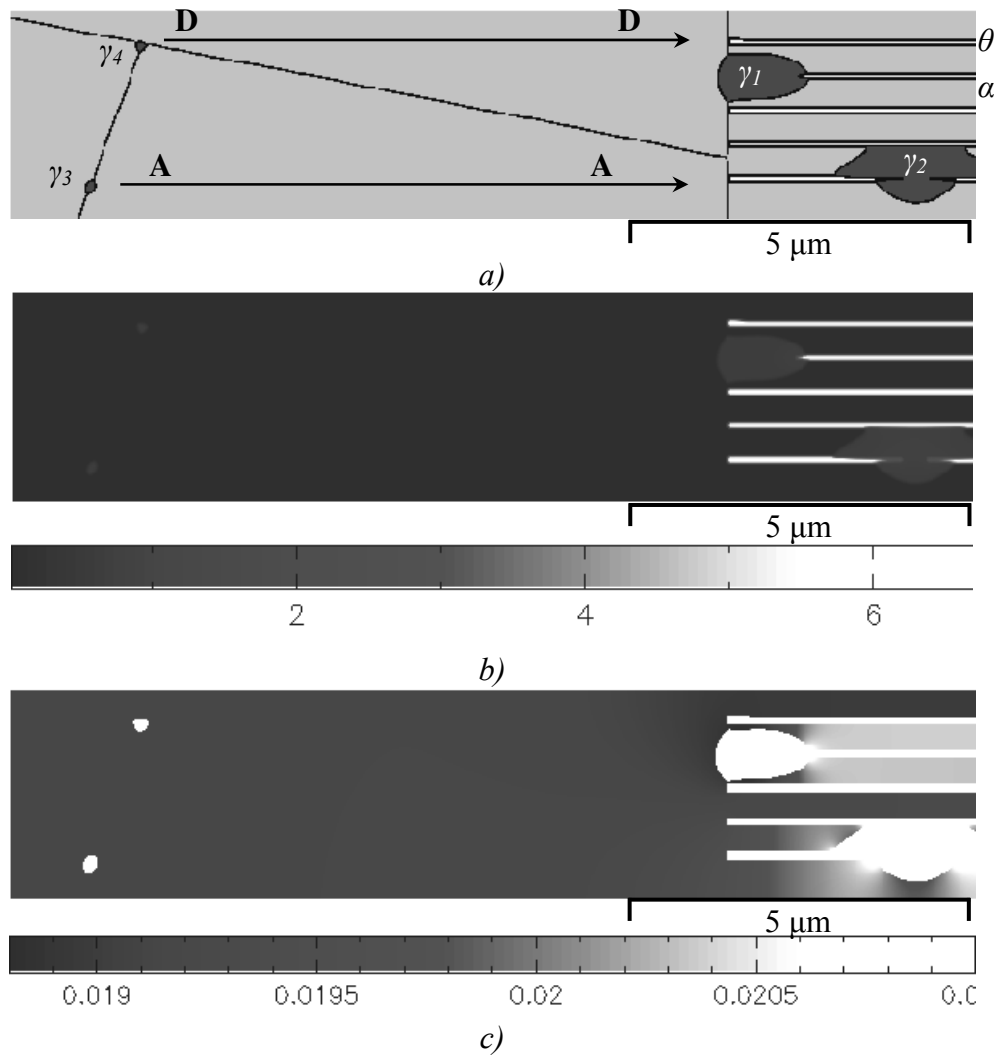


Figure 8.4. The evolution of the microstructure after 1 s of the isothermal holding at 727 °C. a) general view of the microstructure, b) general carbon redistribution profile and c) carbon gradients in ferrite. α = ferrite, γ = austenite, θ = cementite. For the color version refer to the appendix.

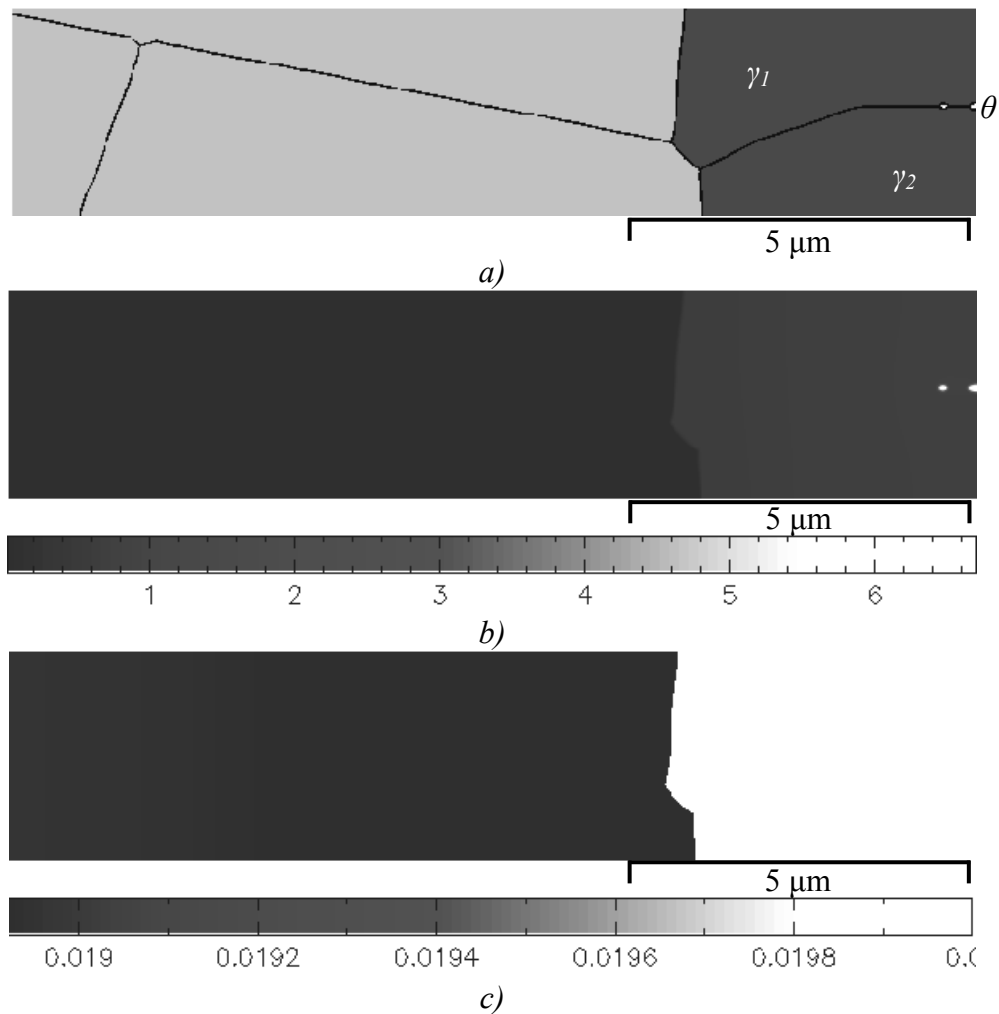


Figure 8.5. The evolution of the microstructure after 11 s of the isothermal holding at 727 °C. a) general view of the microstructure, b) general carbon redistribution profile and c) carbon gradients in ferrite. α = ferrite, γ = austenite, θ = cementite. For the color version refer to the appendix.

The present results support the general idea that austenitization of the ferrite-pearlite structure proceeds in three major steps:

- 1) dissolution of pearlite (fast process);
- 2) ferrite-to-austenite transformation (slow process);
- 3) austenite grain growth and carbon homogenization.

The results of the current simulations confirm that those three different steps do not necessarily follow one after the other and can overlap as the transformation

proceeds. This is in a good agreement with the experimental observations (see chapter 4 and 5).

The general tendency clearly seen from Figs. 8.4 and 8.5 is that austenite grains near the source of carbon (on the ferrite-pearlite grain boundary, γ_1 , and inside the pearlite grain on the ferrite-cementite interface, γ_2) grow much faster than the austenite grains that are away from the source of carbon (on the ferrite-ferrite grain boundary, γ_3 , and on the triple point, γ_4). This agrees well with previous observations that were already discussed in the earlier chapters. Even though the uncertainty in the interfacial energies prohibits an accurate quantitative interpretation of the data, qualitatively it is possible to say that the austenite growth rate into pearlite in the current simulations is about 10 times higher than of the austenite growth into proeutectoid ferrite, which is in good agreement with the experimental data (see chapter 5, section 5.3.3).

After the first second of the isothermal holding strong carbon gradients develop in the microstructure in both the austenite and ferrite phases (see Fig. 8.4). Ferrite in contact with cementite has higher carbon content than ferrite that is in contact with austenite. This is a direct result of the equilibrium phase diagram (see Fig. 8.2). Thus, a carbon flux develops towards the austenite grains that are located on the ferrite-ferrite grain boundaries. As the transformation proceeds the carbon gradients first diminish and eventually vanish after some time (see Fig. 8.5).

Figure 8.6 a,b shows carbon concentration profiles in the ferrite grain along the lines A-A and D-D (see Fig. 8.4a) at different time steps. In the initial microstructure (dashed line) the amount of carbon is equal to the α/γ -equilibrium concentration, $x_{\alpha\gamma}^{Ceq} = 0.01867$ wt. %.

After the first second the amount of carbon in the ferrite grain increases significantly and at the ferrite-cementite interface it is much higher than near the ferrite-austenite interface. Even though the diffusion of carbon in the ferrite phase is rather fast (two orders of magnitude higher than in the austenite phase) the development of the carbon concentration profile indicates that carbon diffusion in ferrite does play a role in the austenite formation kinetics. At $t = 2$ s (dash-dot line) further increase of the amount of carbon in the ferrite grain between γ_3 and the pearlite grain (see Fig. 8.6a line A-A) has taken place and stronger carbon gradients develop.

The situation for the line D-D is slightly different from that of line A-A. After 2 s a reverse carbon concentration profile develops, e.g. more carbon near the γ_4 grain and less near the pearlite grain. This is related to the fact that the austenite grain γ_1 is present at the interface and absorbs carbon from the close vicinity (a more detailed description of the carbon evolution near the γ_1 grain will be given later).

The concentration of carbon in ferrite near the ferrite-austenite interface for both situations (line A-A and line D-D) does not change between 1 s and 2 s; however it stays away from its equilibrium value. Since ferrite is oversaturated with carbon, there will be a driving force for its transformation to austenite. This driving force is approximately proportional to the degree of supersaturation of carbon in ferrite on the ferrite-austenite interface (see Fig. 8.7), i.e. a higher value of the carbon concentration

will result in a larger driving force. However, as is seen from Fig. 8.7, the driving force is not the only condition to form a new volume of austenite. Some redistribution of carbon has to take place and only the austenite phase with a carbon content above some critical value, $x_{\alpha}^{critical}$ will be stable. This critical value is $x_0 > x_{\alpha}^{critical} > x_{\gamma\alpha}^{Ceq}$ and is determined by the amount of carbon in ferrite. The concentration of carbon in ferrite on the ferrite-austenite interface, even though it is higher than the equilibrium value, it is nevertheless significantly lower than the critical value, $x_1 \ll x_{\alpha}^{critical}$. Thus, carbon has to be supplied from the pearlite grain, the source of carbon; however, due to a rather large diffusion distance for carbon, austenite growth on the ferrite-ferrite grain boundary will be sluggish.

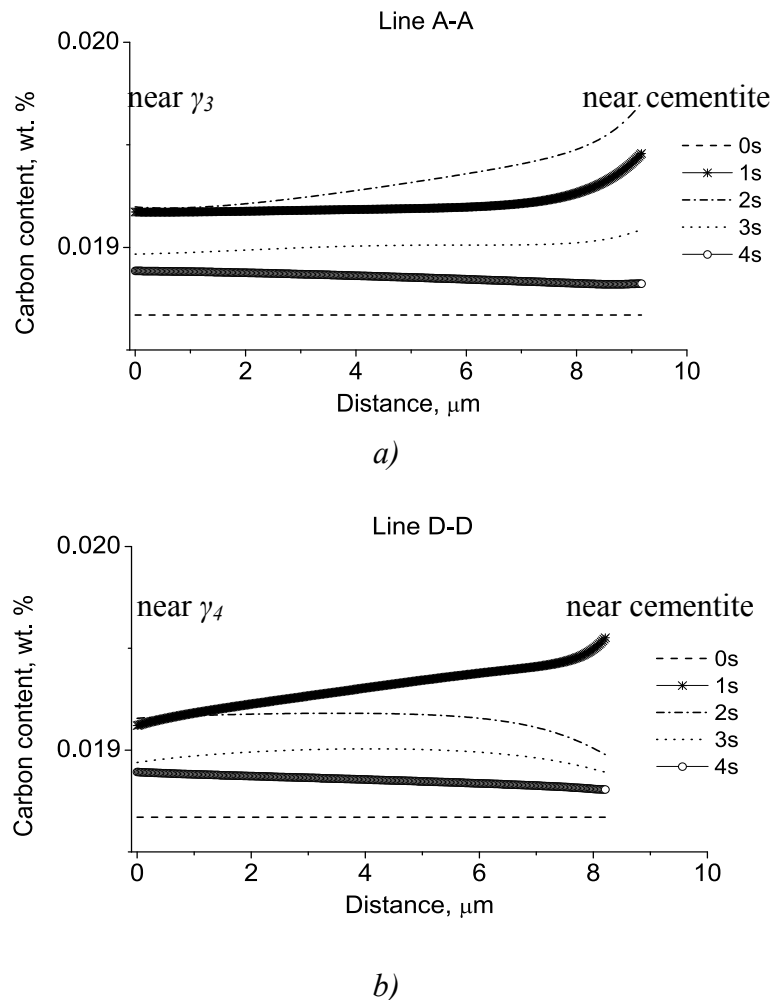


Figure 8.6. Carbon concentration profile in the ferrite grain at different time steps along a) the line A-A and b) the line D-D as shown in Fig. 8.4a.

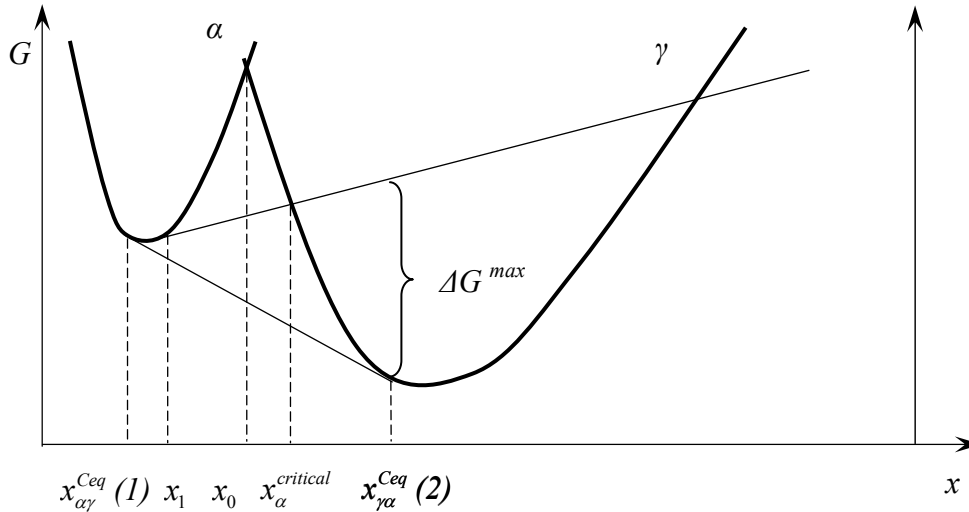


Figure 8.7. Schematic representation of the Gibbs free energy G as a function of the carbon concentration in ferrite (α) and austenite (γ) at a temperature above A_1 . Numbers in brackets correspond to figurative points (1)-(5) in Figs. 4.1, 4.2.

8.3.1. Austenite growth near the source of carbon

As was already mentioned, two locations near the source of carbon were tested: on the pearlite-ferrite grain boundary, γ_1 , and inside the pearlite grain on the ferrite-cementite interface, γ_2 . Even though it was shown by different authors [4-7] (see also chapter 2) that austenite nucleation inside the pearlite grain is not favorable, it was nevertheless interesting to trace and compare the growth of austenite and carbon evolution for the two cases. It is also necessary to keep in mind the limitations of the current simulations, e.g. that crystallographic orientation relations between the ferrite and cementite lamellae, as well as between the pro-eutectoid ferrite and ferrite and cementite in the pearlite grain, are not accounted for. Also, similar values for the interfacial energies for the interfaces were chosen. In reality, however, the same ferrite-cementite interface inside the pearlite grain and on the ferrite-pearlite grain boundary will have different characteristics, since in the first case, due to the crystallographic orientation relationship between ferrite and cementite lamellae, it is a low-energy boundary.

Figures 8.8 and 8.9 show the growth of austenite grains after 1 s and 11 s of isothermal holding. Austenite grains as well as the ferrite phase (both pro-eutectoid and pearlitic) are seen to contain significant concentration variations, which are dictated by the local conditions prior to the transformation. Those concentration variations can be present in the microstructure for some time: after 11 s, even though

the pearlite grain is completely transformed to austenite, the carbon distribution is still not homogeneous.

It is interesting also to notice that the transformation of the ferrite and cementite lamellae is not the same. After 11 s some cementite is still present in the austenite matrix.

The growth rate of the austenite-ferrite interface is not constant. The austenite grain, γ_1 , grows much faster into the pearlite grain than in the opposite direction, into the neighboring ferrite grain (the average growth rate into pearlite is estimated to be 1.1 $\mu\text{m/s}$ and into pro-eutectoid ferrite 0.1 $\mu\text{m/s}$). Even inside the pearlite grain the austenite-ferrite interface is not flat and grows much faster when it is in contact with cementite than in the center of the ferrite lamella (compare the experimental results as shown in chapter 4 in Fig. 4.4a). Thus, there will be a range of the interfacial velocities rather than a unique value. It can be seen in Fig. 8.8 that the grain γ_1 in 1 s grew along the θ lamella for 1.1 μm , whereas it grew only 0.3 μm in the perpendicular direction. The average concentration of carbon inside the austenite grain γ_2 is higher than in γ_1 (see Fig. 8.8b). This is probably related to the fact that when austenite is formed on the pearlite-ferrite grain boundary it grows further into two grains, pearlite and pro-eutectoid ferrite, although with different velocities. When the austenite-ferrite interface propagates into pro-eutectoid ferrite, a significant amount of carbon will be absorbed from the nearest regions. There are two possible sources of carbon in this case: the austenite grain and the pro-eutectoid ferrite grain. In the first case carbon will have to diffuse from the cementite-austenite interface through the austenite grain (see Fig. 8.8b). Since the diffusion in austenite is rather slow, this will lead to the smaller average amount of carbon inside the austenite grain γ_1 in comparison to the austenite grain growing inside the pearlite grain, γ_2 .

On the other hand, the pro-eutectoid ferrite, which has an excess of carbon related to the concentration gradients (already previously discussed), will supply carbon towards the austenite-ferrite interface. Thus, the amount of carbon in pro-eutectoid ferrite near the austenite grain will be reduced and a situation close to equilibrium will be established. This leads to a smaller driving force for the transformation and slow movement of the austenite-ferrite interface.

Figure 8.8c shows the carbon inhomogeneities in the ferrite phase. It is essential to consider these since that gives insight into the remarkable behavior of the austenite-ferrite interface. The velocity of the interface is proportional to the driving force. In turn, the amount of free energy that the system gains with the formation of austenite depends on the concentration of carbon dissolved in ferrite. Near the triple points (ferrite-cementite-austenite, inside the pearlite grain) the concentration of carbon in ferrite is relatively high. The austenite-ferrite interface will move very quickly since the driving force is large and carbon is already present at the reaction point. The concentration of carbon in ferrite on the austenite-ferrite interface will depend on the location of the austenite grain: inside the pearlite grain, γ_2 , it will have a higher value than in the case when austenite is in contact with the pro-eutectoid ferrite, γ_1 .

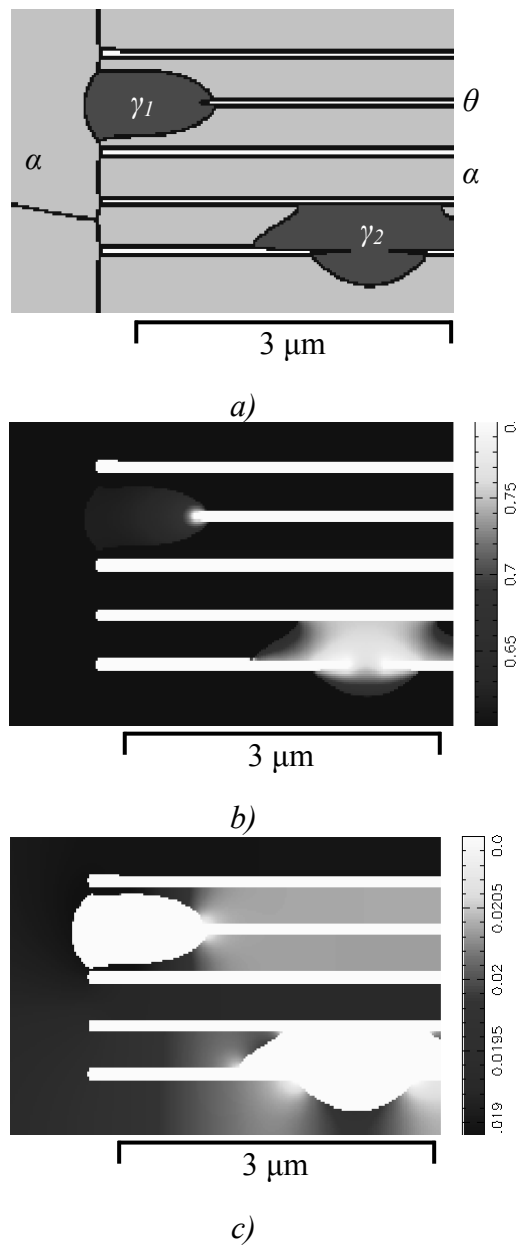


Figure 8.8. Austenite growth near the source of carbon: on the pearlite-ferrite grain boundary, γ_1 , and inside the pearlite grain on the ferrite-cementite grain boundary, γ_2 . Isothermal holding at 727°C for 1 s. a) general view of the microstructure, b) carbon gradients in austenite and c) carbon gradients in ferrite. α = ferrite, γ = austenite, θ = cementite.

For the color version refer to the appendix.

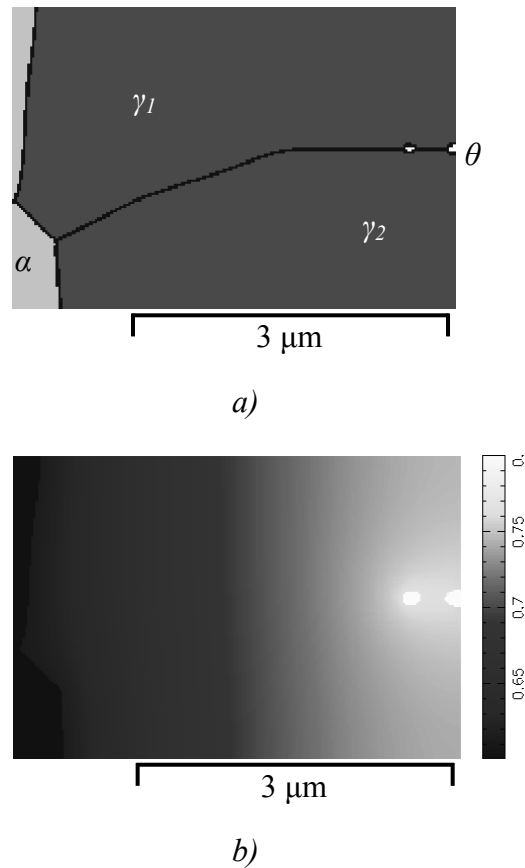


Figure 8.9. Austenite growth near the source of carbon: on the pearlite-ferrite grain boundary, γ_1 , and inside the pearlite grain on the ferrite-cementite grain boundary, γ_2 . Isothermal holding at 727 °C for 11 s. a) general view of the microstructure and b) carbon gradients in austenite. α = ferrite, γ = austenite, θ = cementite. For the color version refer to the appendix.

8.3.2. Austenite growth away from the source of carbon

Figure 8.10 shows the growth of austenite and the carbon development during isothermal holding for 1, 2.5 and 9 s for the two grains that are formed away from the source of carbon, e.g. on the ferrite-ferrite grain boundary, γ_3 , and on the triple point, γ_4 . In the initial microstructure the amount of carbon inside the austenite grain is set to be equal to 0.27 wt. % (see the experimental results of chapter 4 section 4.4.1). Since those grains have much less carbon than the equilibrium value, after the first second of isothermal holding the size of each grain decreases and the average carbon content inside each austenite grain increases until the equilibrium value is reached (see also Figs. 8.11, 8.12). During the next seconds the curvature effect (see Eqs. 6.2 and 8.2)

starts to play a significant role. For a system it is energetically more favorable to contain one big grain instead of two small ones and grain growth takes place.

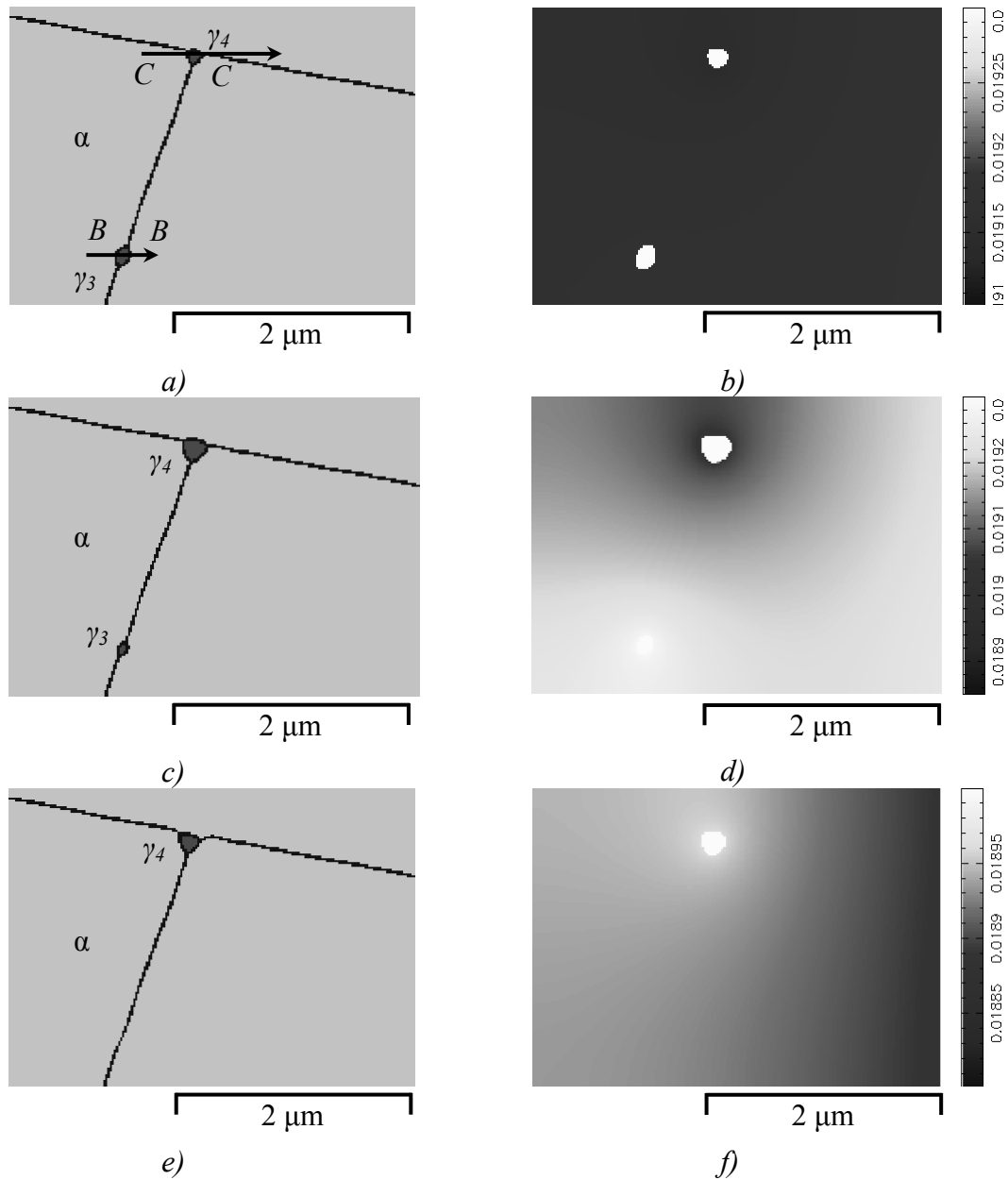


Figure 8.10. Austenite growth away from the source of carbon: on the ferrite-ferrite grain boundary, γ_3 , and on the triple point, γ_4 . Isothermal holding at 727 °C for. a), b) 1 s; c), d) 2.5 s and e), f) 9 s.

a), c), e) general view of the microstructure and b), d), f) carbon gradients in ferrite. α = ferrite, γ = austenite.

For the color version refer to the appendix.

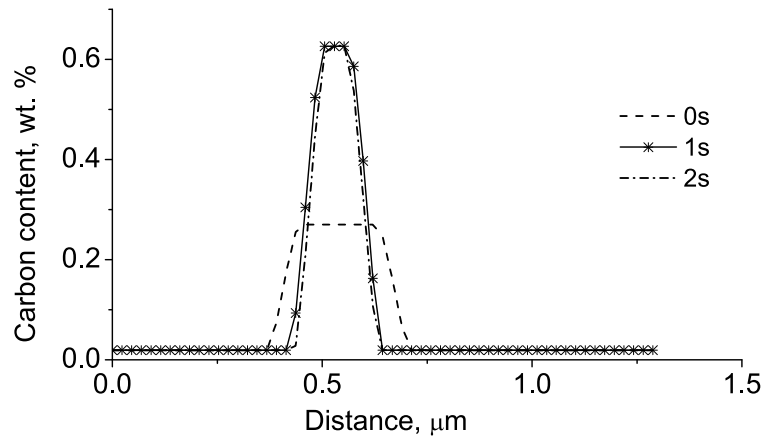


Figure 8.11. Carbon concentration profile along the line B-B (see Fig. 8.10a) at different time steps.

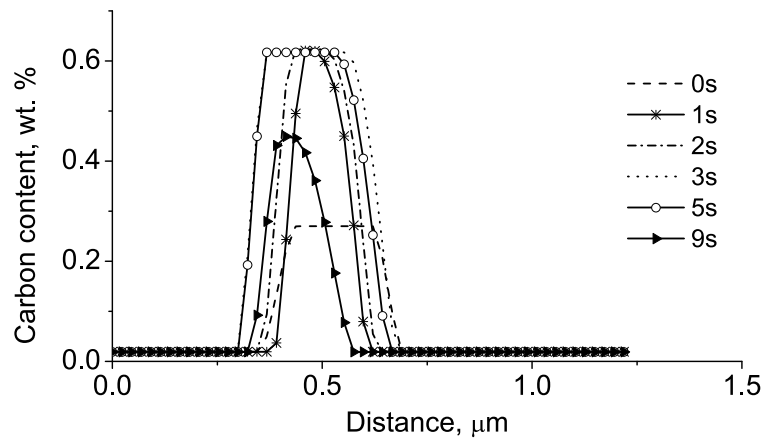


Figure 8.12. Carbon concentration profile along the line C-C (see Fig. 8.10a) at different time steps.

The austenite grain on the ferrite-ferrite grain boundary, γ_3 , is less stable in comparison to the triple point grain, γ_4 , since the shrinkage of the grain γ_4 would require more α/α interfacial area to form. Thus, the austenite grain on the ferrite-ferrite grain boundary, γ_3 , shrinks first and after 3 s of isothermal holding this grain has disappeared. During the shrinkage process, carbon from the γ_3 grain diffuses through the pro-eutectoid ferrite and a carbon concentration gradient is established in the direction of the austenite grain on the triple point, γ_4 (see Fig. 8.10b). This extra

carbon in addition to the excess carbon that is already present in proeutectoid ferrite (see section 8.3), is absorbed by the austenite grain γ_4 and results in its growth.

The austenite-ferrite interface velocity of the γ_4 grain is estimated to be 0.02 $\mu\text{m/s}$ and is on the same order of magnitude as the growth rate of the austenite-ferrite interface of the γ_1 grain (formed near the source of carbon on the ferrite-pearlite interface) into pro-eutectoid ferrite (see section 8.3.1). This indicates that since grain γ_4 is away from carbon source, the diffusion in ferrite is an important factor in austenite transformation kinetics and has to be taken into account. Although carbon diffusion in ferrite is much faster than in austenite, in comparison with the growth rate of the austenite-ferrite interface of grain γ_1 into pearlite, the growth rate of grain γ_4 is more than 10 times less because of the much larger diffusion distances involved.

After 9 s of isothermal holding the shrinkage of the γ_4 grain becomes apparent. At this time step the microstructure consists of a ferrite-austenite mixture. The carbon gradient in the pro-eutectoid ferrite (between austenite formed in pearlite, near the source of carbon, and in ferrite, away from the source of carbon, lines A-A and D-D) not only reduces significantly but the slope also changes the sign. As was already mentioned above, as the grain γ_1 grows it absorbs carbon not only from pearlite but also from the pro-eutectoid ferrite grain. Thus, the carbon concentration in pro-eutectoid ferrite that is in contact with the grains γ_1 and γ_2 is lowered and a reverse carbon concentration gradient establishes. This results in a carbon flux towards the austenite grain γ_1 , and in combination with the curvature effect leads to the shrinkage of the grain γ_4 . During this process, for the chosen simulation conditions, similar to the shrinkage of the austenite grain γ_3 , carbon is pushed into pro-eutectoid ferrite and the γ_4 grain decreases in size and finally disappears. Pro-eutectoid ferrite in the area where the austenite grain was present prior to the shrinkage, for some time is oversaturated with carbon. However, during further isothermal holding due to the differences in chemical potentials this carbon is pushed towards the grains γ_1 and γ_2 . After some time, the final microstructure consists of an austenite-ferrite mixture, in which the concentration of carbon in each phase reaches its equilibrium value.

The results of the current simulations show that austenite grains with metastable composition can survive and even grow for some time during isothermal holding above the eutectoid temperature. During this process carbon within such grains reaches its equilibrium value before shrinkage, due to the interfacial energy, takes place. The growth rate of such grains heavily depends on the distance between the source of carbon and the grain. It is necessary to mention, however, that in the current simulations the effect of Mn was not taken into account. Manganese is expected to play a significant role in the growth of the metastable austenite grains. As was already mentioned in chapter 6, at low heating rates Mn can redistribute locally in the vicinity of the interface, thus reducing the driving force for back transformation (austenite into ferrite) and stabilizing metastable austenite grains. The degree in which this effect can influence the growth kinetics of austenite grains is, however, difficult to estimate; new simulations have to be performed.

The effect of the grain boundary diffusion was also not taken into account in the current simulations. It is however expected to play a role in transformation

kinetics, since the grain boundary diffusion is an order of magnitude higher than the bulk diffusion.

8.4. Conclusions

In this chapter the ferrite/pearlite-to-austenite transformation was simulated on a small scale. Pearlite was modeled explicitly as a mixture of two phases: ferrite and cementite. Different locations for austenite grains were tested: near the source of carbon (pearlite-ferrite grain boundary and ferrite-cementite interface) and away from the source of carbon (ferrite-ferrite grain boundary). It was shown that austenite growth into pearlite is 10 times faster than into pro-eutectoid ferrite, which is in good agreement with the experimental data. It was shown that the carbon evolution during the transformation is responsible for the different growth rates. Strong concentration gradients develop during the transformation in both austenite and ferrite.

Metastable austenite grains that formed on the ferrite-ferrite grain boundaries can survive and even grow for some time, but due to the evolution of carbon gradients and the curvature effect eventually shrink and dissolve. The growth kinetics of such grains depends on the distance of the grain from the source of carbon.

References

- [1] MICRESS®, Software developed in ACCESS, an independent research center associated with the Technical University of Aachen.
- [2] B. Sundman, B. Jansson, J.-O. Andrésson, The Thermo-Calc databank system, *CALPHAD* 9, 1985, pp. 153-190.
- [3] M. Militzer, M.G. Meozzi, J. Sietsma, S. van der Zwaag, *Acta Mater.*, 2006, vol. 54, pp. 3961-3972.
- [4] G. R. Speich, A. Szirmai, *Trans. Metall. Society*, 1969, vol. 245, pp. 1063-1074.
- [5] F.G. Caballero, C. Capdevila, C. Garcia de Andrés, *Mater. Sci. Tech.*, 2001, vol. 17, pp. 1114-1118.
- [6] R. F. Mehl, *Trans. Amer. Society for Metals*, 1941, vol. 29, p. 813.
- [7] A. Roósz, Z. Gácsi, E.G. Fuchs, *Acta Metall.*, 1983, vol. 31, no. 4, pp. 509-517.

Summary

The production process of almost all modern steels involves austenitization – formation of the austenite phase upon continuous heating. Many of the microstructural features and properties that are obtained upon subsequent cooling are to a large extent determined by the evolution of the microstructure and chemical inhomogeneities during austenitization. In spite of its importance, austenitization so far has received much less attention than the transformations on cooling; however, the interest is continuously increasing, especially for the development of new types of steels (*Dual-Phase steel, TRansformation-Induced Plasticity steel etc.*).

At the current stage of the research almost no information is available on the austenite nucleation, which makes it difficult to build a realistic model for the austenitization process. The carbon redistribution during the austenitization, even though it did receive some attention in the literature, still involves a lot of question marks. For example, most of the models that are developed for the ferrite-to-austenite transformation are based on the idea that the local equilibrium conditions are present at the austenite-ferrite interface. The results of the present work show that this is not always the case and depending on the heating conditions a transition from the diffusion-controlled to mixed mode transformation occurs (chapter 6).

In the current work the austenitization process was studied from two different sides: experimental and by modeling. This is believed to be the best approach since experimental data are necessary to build and validate a model which in turn provides additional data (for example carbon content on the austenite-ferrite interface). The experimental study of the austenitization was performed on a series of C-Mn steels (C22, C35, C45 and C60) with an initial ferrite-pearlite microstructure. The following techniques were applied (chapter 3):

- optical and scanning electron microscopy: to reveal the microstructural features (on quenched samples);
- electron probe microanalysis: to study the redistribution of alloying elements between different phases (on quenched samples);
- dilatometry: to study the austenite transformation kinetics during continuous heating with different heating rates (in-situ measurements);
- three-dimensional X-ray diffraction microscopy: to study austenite nucleation and growth (in-situ measurements).

A combination of all the above mentioned techniques gave a more general and complete description of the austenitization process than was beforehand available in the literature. Austenite formation, as most phase transition phenomena, consists from two major stages: nucleation and growth. The most favorable sites for austenite nucleation are the pearlite-pearlite and pearlite-ferrite grain boundaries (chapter 5).

They are advantageous sites because:

- i. they are high-energy boundaries, and
- ii. the presence of carbon makes the newly formed austenite nuclei relatively stable.

An interesting outcome of the current research is the formation of metastable austenite on the ferrite-ferrite grain boundaries. This metastable austenite appears at the early stages of the transformation, when only pearlite is expected to transform to austenite, and contains less carbon than the equilibrium value (chapter 4). It was argued that although austenite is formed with a carbon concentration less than equilibrium its formation is nevertheless thermodynamically possible. The growth kinetics of such austenite is measured to be very slow, since the carbon diffusion distances involved are large (chapter 5). On the other hand, the growth rate of austenite that is formed on the pearlite-ferrite grain boundaries (for which pearlite serves as a source of carbon) is almost 10 times higher than to the one for austenite formed on the ferrite-ferrite grain boundaries (away from the source of carbon).

The microstructural features of austenite formation show that the character of austenite formation strongly depends on the heating rate. Different growth morphologies were observed, among which the finger-type growth is the most interesting and the less understood phenomenon (chapter 4). The formation of different phases upon cooling (martensite, bainite) is related to the carbon inhomogeneities that are present in the microstructure prior to cooling (chapter 4).

The unique experimental data on austenite nucleation that were performed by 3DXRD microscopy show two different nucleation regimes: initial fast nucleation, likely taking place on pearlite colonies, and slower nucleation, possibly on the ferrite/ferrite grain boundaries (chapter 5). The value of the nucleation parameter ψ , which contains information about the shape of the nucleus (geometric factors) and the interfacial energies that are involved in the nucleation process, are extremely low for both nucleation regimes. This indicates that the specific nucleation conditions for nucleation to take place on the high-energy sites such as triple and quadruple points, are highly advantageous.

Another unique outcome of the 3DXRD measurements is the observation of different growth types of individual austenite grains. Three different austenite grain-growth types were observed. Type A is similar to the overall transformation behavior, with fast pearlite decomposition into austenite and slow ferrite-to-austenite transformation. In this case, once an austenite grain consumed all pearlite, it continues to grow further into pro-eutectoid ferrite with the same crystallographic orientation. Growth type B is related to austenite nucleation and growth on the ferrite-ferrite grain boundaries, away from the source of carbon. In this case, the formation of low-carbon austenite, compared to the growth type A, can be expected. In growth type C, an acceleration of the transformation at the last stages of the transformation is observed and is likely to be related to a change in transformation mode – from partitioning to massive.

For the modeling part the phase-field approach and the code MICRESS[®] was used to simulate the pearlite+ferrite-to-austenite transformation (chapter 6-8). In the model, the pearlite phase is considered as a uniform phase with eutectoid composition (chapter 6). Classical nucleation theory and experimental data from 3DXRD measurements were used to model the nucleation. The simulated microstructures and kinetics correlate well with the experimentally found ones, but not all the individual single-grain austenite growth types, as observed experimentally, were reproduced in the simulations, possibly due to the simplifications applied in the model.

The model also delivered valuable information on the carbon redistribution/partitioning during continuous heating, which cannot be obtained experimentally. The redistribution/partitioning of carbon on the ferrite-austenite interface does not follow the diffusion-controlled mode for all the heating rates, as most literature models suggest. Instead, a shift from the diffusion-controlled to mixed-mode transformation is observed with increasing heating rate. It was also shown that the overlap of the pearlite-to-austenite and ferrite-to-austenite transformations is related to the heating rate, e.g. with increasing heating rate the degree in which the two transformations overlap increases.

Finally, simulations on a smaller scale, where pearlite was modeled explicitly as a mixture of two phases, ferrite and cementite, were performed (chapter 8). Different nucleation sites were tested: near the source of carbon (pearlite-ferrite grain boundary and ferrite-cementite interface) and away from the source of carbon (ferrite-ferrite grain boundary). It was shown that austenite growth into pearlite is 10 times faster than growth into pro-eutectoid ferrite, which is in a good agreement with the experimental data. The carbon concentration profile development during the transformation is responsible for the different growth rates. Strong concentration gradients that develop during the transformation in both austenite and ferrite phases can lead to the formation of different phases (ferrite, martensite, bainite) upon cooling (the formation of such structures was experimentally observed in chapter 4).

Austenite grains formed on the ferrite-ferrite grain boundaries with relatively low carbon content can survive for some time, but due to the carbon gradient development and the curvature effect will eventually shrink (chapter 8). The growth kinetics of such growth will depend on the distance between the grain and the source of carbon.

Based on the results of the current work the following recommendations for the future work can be proposed:

1. Developing further insight on the different growth morphologies (in particular “finger-type”).
2. Further development of the theory describing nucleation with $\Delta G^* < kT$.
3. The massive transformation during austenitization needs further experimental evidence and theory development.
4. Nucleation on the ferrite-ferrite grain boundaries during austenitization, even though it is a minor effect in an annealed structure, can be more important in a deformed structure. Although some work was already done by J. Huang

(“*Microstructural evolution during processing of Dual-phase and TRIP steels*”, PhD thesis, University of British Columbia, 2004), further theory development is necessary.

5. Manganese (and other alloying elements) redistribution during austenitization needs more attention. Incorporation of both redistribution of alloying elements during the transformation and grain boundary diffusion in MICRESS would improve the simulations.
6. Diffusion of carbon in ferrite during austenitization needs further studies (experimental as well as modeling). Diffusion of carbon in ferrite cannot be ignored and has to be incorporated in the austenitization models.
7. New models for the phase transformations during heating, based on a mixed-mode approach, need to be developed. They will give a better description of the austenitization process.

Samenvatting

Het productieproces van alle moderne staalsoorten bevat een stadium waarin *austenitization* plaatsvindt - austenietvorming tijdens voortdurende opwarming. Veel van de microstructurele karakteristieken en eigenschappen die worden verkregen tijdens het afkoelen zijn voor een groot gedeelte bepaald door de evolutie van de microstructuur en chemische inhomogeniteiten gedurende het austenitiseren. Ondanks het belang van austenitiseren is er veel minder onderzoek aan gedaan dan aan de transformatieprocessen tijdens de afkoelfase van het productieproces. De interesse is neemt echter toe als gevolg van de ontwikkeling van nieuwe typen staal (*Dual-Phase* staal, *TRansformation-Induced Plasticity* staal *etc.*).

In de huidige fase van het onderzoek is er bijna geen informatie beschikbaar over de austeniet nucleatie. Dit maakt het moeilijk om een realistisch model te maken van het vormingsproces van austeniet. De herverdeling van koolstof gedurende de austenitisatie bevat nog steeds veel vraagtekens, ondanks het feit dat enige aandacht hieraan is gegeven in de literatuur. Bijvoorbeeld, veel modellen die zijn ontwikkeld voor de ferriet-naar-austeniet transformatie zijn gebaseerd op het idee dat lokaal evenwichtscondities aanwezig zijn aan het austeniet-ferriet grensvlak, hetgeen betekent dat de transformatiekinetiek bepaald wordt door diffusie van koolstof. De resultaten van het in dit proefschrift beschreven onderzoek laten zien dat dit is niet altijd het geval is en dat, afhankelijk van de opwarmingscondities, een transitie van diffusie-gecontroleerde transformatie naar mixed-mode transformatie optreedt (hoofdstuk 6).

In dit werk is het austenitisatieproces bestudeerd van verschillende kanten: experimenteel en door modellering. Verondersteld wordt dat dit de beste manier is omdat experimentele gegevens nodig zijn om een model te bouwen en valideren, waarna door gebruikmaking van het model additionele informatie verkregen wordt (bijvoorbeeld de concentratie van koolstof aan het austeniet-ferriet grensvlak). De experimentele studie van de austenitisatie is uitgevoerd aan een serie van C-Mn staalsoorten (C22, C35, C45 en C60) met een initiële ferriet-perliet microstructuur.

De volgende technieken zijn toegepast (hoofdstuk 3):

- Optische en scanning electronen-microscopie: om de microstructurele karakteristieken vast te stellen (op proefstukken die snel zijn afgekoeld);
- electron probe microanalysis; om de herverdeling van legeringselementen tussen verschillende fasen te bestuderen (op proefstukken die snel zijn afgekoeld);
- dilatometrie; om de kinetiek van de austenietvorming gedurende continu opwarmen met verschillende snelheden (in-situ metingen);
- 3D Röntgendiffractie-microscopie; om de austenietnucleatie en -groei te bestuderen (in-situ metingen);

De combinatie van alle bovengenoemde technieken geeft een meer generieke en complete beschrijving van het austenitisatieproces dan voorheen in de literatuur beschikbaar was. Austenietformatie, zoals de meeste faseformatiefenomenen, omvat twee belangrijke fases: nucleatie en groei. De plaatsen waar austeniet nucleatie preferentieel plaatsvindt zijn de perliet-perliet en perliet-ferriet korrelgrenzen (hoofdstuk 5). Dit zijn favoriete plaatsen omdat:

- i. deze korrelgrenzen een relatief hoge energie hebben,
- ii. de aanwezigheid van koolstof de nieuw gevormde austenietnuclei relatief stabiel maakt.

Een interessante uitkomst van het onderzoek is de formatie van metastabiel austeniet op ferriet-ferriet korrelgrenzen. Deze metastabiele austeniet vormt zich in de beginfase van de transformatie, waar verwacht wordt dat alleen perliet transformeert naar austeniet, en bevat minder koolstof dan de evenwichtswaarde (hoofdstuk 4). In de literatuur wordt betwist dat deze formatie van relatief koolstofarme austeniet thermodynamisch mogelijk is. In hoofdstuk 4 wordt de thermodynamische basis van dit proces bediscussieerd. Er is gemeten dat de groei kinetiek van dergelijke austeniet zeer langzaam is, omdat de afstanden voor de aanvoer van koolstof middels diffusie groot zijn (hoofdstuk 5). Daarom is de groeisnelheid van austeniet dat wordt gevormd op de perliet-ferriet korrelgrens (alwaar perliet de bron vormt voor koolstof) bijna 10 keer hoger dan de austenietformatie op de ferriet-ferriet korrelgrens (waar geen koolstofbron aanwezig is).

De microstructurele karakteristieken van de austenietformatie laten zien dat het karakter van austenietformatie zeer afhankelijk is van de opwarmingssnelheid. Verschillende groei morfologieën zijn waargenomen, waarbij *finger-type* groei het meest interessante maar minst begrepen fenomeen is (hoofdstuk 4). De formatie van verschillende fasen bij afkoeling (martensiet, bainjiet) is gerelateerd aan de koolstofinhomogeniteiten die aanwezig zijn in de (gedeeltelijk) austenitische microstructuur voor afkoeling (hoofdstuk 4).

De unieke experimentele gegevens van austeniet nucleatie die gevonden zijn bij 3D-XRD microscopie laten twee verschillende nucleatie regimes zien: initiële snelle nucleatie, waarschijnlijk plaatsvindend op perliet kolonies, en langzame nucleatie, mogelijk op de ferriet-ferriet korrelgrenzen (hoofdstuk 5). De waarde van de nucleatie parameter ψ , welke informatie bevat over de vorm van de nucleus en de korrel grensenergieën die betrokken zijn bij het nucleatie proces, zijn extreem laag voor beide nucleatie regimes. Dit geeft aan dat de specifieke condities voor nucleatie zeer gunstig zijn.

Een andere unieke uitkomst van de 3D-XRD metingen is de waarneming van verschillende groeitypen van individuele austeniet korrels. Drie verschillende groeitypen zijn waargenomen voor austeniet korrels. Groeitype A is gelijk aan het algemene transformatiegedrag, met snelle transformatie van perliet in austeniet en langzame ferriet-naar-austeniet transformatie. In dit geval groeit de austeniet korrel met dezelfde kristallografische oriëntatie verder in pro-eutectoïdische ferriet, wanneer

de perliet is omgezet. Groeitype B is gerelateerd aan austeniet nucleatie en -groei op ferriet-ferriet korrelgrenzen, relatief ver verwijderd van de koolstofbron. In dit geval kan de formatie van austeniet met een laag koolstofgehalte, vergeleken met groeitype A, verwacht worden. In groeitype C is een acceleratie van de transformatie in het laatste stadium van de transformatie waargenomen. Deze transitie komt waarschijnlijk voort uit een verandering van transformatiemechanisme – van *partitioning* (waarbij koolstof herverdeeld wordt) naar massief (waarbij de zich vormende fase dezelfde koolstofconcentratie heeft).

In het modelleergedeelte van dit proefschrift (de hoofdstukken 6, 7 en 8) is de *phase field* aanpak en de code MICRESS® gebruikt om de perliet+ferriet-naar-austeniet transformatie te simuleren. In het model is de perliet fase beschouwd als een uniforme fase met de eutectoïdische samenstelling (hoofdstuk 6). De klassieke nucleatie theorie en experimentele data van de 3D-XRD metingen zijn gebruikt om de nucleatie te modelleren. De gesimuleerde microstructuren en kinetiek correleren goed met de gevonden resultaten uit de experimenten. Toch worden niet alle groeitypen voor de individuele austeniet korrels, zoals bij de experimenten waargenomen, gereproduceerd in de simulaties, mogelijk als gevolg van de simplificaties in het model.

Het model leverde ook waardevolle informatie over de herverdeling van koolstof gedurende continue opwarming, die experimenteel niet verkregen kan worden. De herverdeling van koolstof aan het ferriet-austeniet grensvlak geeft aan dat de transformatie niet het diffusie-gecontroleerde mechanisme volgt voor alle opwarmsnelheden, in tegenstelling tot wat de meeste modellen in de literatuur suggereren. In plaats daarvan is een verschuiving van diffusie-gecontroleerde naar mixed-mode transformatie waargenomen bij het verhogen van de opwarmsnelheid. Er is tevens aangetoond dat de overlap van perliet-naar-austeniet en ferriet-naar-austeniet transformatie gerelateerd is aan de oververhitting (d.w.z. de overschrijding van de evenwichtstemperatuur), m.a.w. met het verhogen van de oververhitting zal de overlap tussen de twee transformaties vergroten.

Tenslotte zijn simulaties op kleinere schaal uitgevoerd, waarin perliet expliciet gemodelleerd is als een combinatie van de twee fasen, ferriet en cementiet (hoofdstuk 8). Verschillende nucleatie plaatsen zijn getest: bij de koolstofbron (perliet-ferriet korrelgrens en ferriet-cementiet grensvlak) en op grotere afstand van de koolstofbron (ferriet-ferriet korrelgrenzen). Er is aangetoond dat austeniet groei vanuit perliet $10\times$ zo snel is als groei vanuit pro-eutectoïdisch ferriet, het geen goed aansluit bij de experimentele gegevens. De ontwikkeling van het koolstof concentratieprofiel gedurende de transformatie is verantwoordelijk voor de verschillende groeistadia. Sterke concentratiegradiënten die zich ontwikkelen gedurende de transformatie van verschillende fasen in zowel austeniet als ferriet kunnen leiden tot de formatie van verschillende fasen (ferriet, martensiet, bainiet) tijdens afkoeling (de formatie van zulke structuren was waargenomen tijdens de experimenten in hoofdstuk 4).

Austeniet korrels die gevormd worden op de ferriet-ferriet korrelgrenzen met relatief lage koolstofgehalten kunnen lange tijd bestaan, maar door de ontwikkeling van koolstofgradiënten en het effect van de korrel grensenergie zullen ze uiteindelijk

slinken (hoofdstuk 8). De kinetiek van dergelijke groei is afhankelijk van de afstand tussen de korrel en de koolstofbron.

Op basis van de resultaten van dit onderzoek worden de volgende aanbevelingen gedaan voor toekomstig werk:

1. Het verder ontwikkelen van inzicht in de verschillende groeimorfologiën (in het bijzonder de *finger-type* morfologie) is noodzakelijk.
2. Verdere ontwikkeling van de theorie voor de nucleatie met $\Delta G^* < kT$.
3. Het eventuele optreden van massieve transformatie gedurende austenitisatie vereist meer experimenteel onderzoek en theoretische onderbouwing.
4. Nucleatie op de ferriet-ferriet korrelgrenzen gedurende austenitisatie, die weliswaar weinig invloed heeft in een goed uitgegloeide structuur, kan veel invloed hebben als de structuur gedeformeerd is. Ondanks dat er al onderzoek is gedaan door J. Huang ("*Microstructural evolution during processing of Dual-phase and TRIP steels*", *PhD thesis, University of British Columbia, 2004*), is hier verdere theoretische ontwikkeling nodig.
5. De herverdeling van mangaan (en andere legeringselementen) gedurende austenitisatie heeft meer aandacht nodig. De implementatie van de herverdeling van legeringselementen gedurende de transformatie en van korrelgrensdiffusie in MICRESS kan de kwaliteit van de simulaties verbeteren.
6. Diffusie van koolstof in ferriet gedurende austenitisatie heeft verdere studie nodig (experimenteel en modelmatig). Diffusie van koolstof in ferriet kan niet genegeerd worden en dient meegenomen te worden in de austenitisiemodellen.
7. Nieuwe modellen voor de fasetransformatie gedurende opwarming, welke gebaseerd zijn op een mixed-mode benadering, dienen ontwikkeld te worden. Deze zullen een betere beschrijving geven van het austenitatieproces.

Acknowledgments

This work was done within the framework of the research program of the Materials Innovation Institute M2i (www.m2i.nl), project MC5.03171. First of all, many thanks to M2i for paying for my Master studies here in TU Delft and allowing me to work part-time as a student-assistant. And secondly, thanks for accepting me as a PhD researcher and giving me the opportunity to get a PhD degree. Without M2i support everything that I have done would not be possible.

My first thoughts of gratitude go also to L. Kestens and J. Sietsma. Leo - thanks for being my promoter and giving me the opportunity to get a PhD degree. Jilt - thanks for being my supervisor, for sharing your knowledge, for your inspiration and motivation, for fruitful discussions and critical comments. I have learned a lot from you.

The support of Corus RD&T and especially of the group of M. Maier, for this project is acknowledged. Special thanks to D. Hanlon for being my industrial supervisor during these four years and to J. Bakels and J. Colijn for being my supervisors during my internship at Corus.

I would like to express my gratitude to E. Offerman without whom chapter 5 of this thesis would not be possible. Thanks for sharing the data as well as for allowing me to use your software to analyze the raw data, thanks for sharing your knowledge of nucleation phenomena. I would also like to thank N. van Dijk for his valuable comments and discussion on austenite nucleation. I would like to acknowledge the European Synchrotron Radiation Facility for provision of synchrotron radiation facilities and to thank S. Grigull, L. Margulies, E.M. Lauridsen, S. van der Zwaag, and H.F. Poulsen for general support to this work.

Thanks also go to our technicians E. Peekstok and N. Geerlofs for helping with the experiments, samples preparation and optical microscopy. I would also like to mention the help of C. Kwakernaak, W.G. Sloof and A. Rijkenberg (Corus) for performing the EPMA and SEM measurements.

I would like specially mention the great help of R. Huizenga. Thanks for adopting all the possible models for me and thanks for your endless help.

I want to acknowledge a valuable help from R. Thiessen. Thanks for introducing me to MICRESS and sharing your knowledge about the phase-filed simulations of the ferrite-pearlite microstructures. I also would like to thank A. Murugaiyan for the help with thermo-dynamic calculations and MICRESS simulations. Special thanks to Ph. Schaffnit from MICRESS (Aachen) for consulting and technical support.

For the companionship and pleasant atmosphere I would like to thank all the MCM members. I want to specially mention Y. van Leeuwen for being my daily supervisor during the first two years of my PhD. In addition, I would like to mention the great help and support from D. Eskin. His friendship is highly acknowledged. The

Acknowledgments

support of the “Russian-Ukrainian-speaking” community is gratefully acknowledged as well.

Finally, I would like to thank my family for their love and support during all those years. Special thanks to my mom, who gave me life, who taught me how to live, who gave me a good education, who always supported me in everything I did, for her unwavering faith in me.

Last but not the least, I’m eternally grateful to my husband, Sebastiaan, for all his help, love, support and understanding. We did it!!!

List of publications

1. V.I. Savran, S.E. Offerman, J. Sietsma, Austenite nucleation and growth on the level of individual grains observed by 3DXRD microscopy, *Metall. Mater. Trans. A*, (submitted).
2. V.I. Savran, Y. van Leeuwen, D.N. Hanlon, C. Kwakernaak, W.G. Sloof, J. Sietsma, Microstructure features of austenite formation in C35 and C45 alloys, *Metall. Mater. Trans. A*, 2007, vol. 38A, May, pp. 946-995.
3. V.I. Savran, S.E. Offerman, N.H. van Dijk, E.M. Lauridsen, L. Margulies, J. Sietsma, Growth of individual austenite grains measured with 3DXRD microscopy, *Materials Science Forum*, 2007, vol. 561-565, pp. 2301-2304.
4. V.I. Savran, Y. van Leeuwen, D.N. Hanlon, J. Sietsma, Austenite formation in C35 and C45 alloys, *Materials Science Forum*, 2007, vol. 539-543, Part 5, pp. 4637-4642.
5. D.G. Eskin, V.I. Savran, L. Katgerman, Effects of melt temperature and casting speed on the structure and defect formation during Direct Chill casting of an Al-Cu alloy, *Metall. Mater. Trans. A*, July 2005, vol. 36A, no. 7, pp. 1965-1976A.
6. Suyitno, D.G. Eskin, V.I. Savran, L. Katgerman, Effects of alloy composition and casting speed on structure formation and hot tearing during DC casting of Al-Cu alloys, *Metall. Mater. Trans. A*, 2004, vol. 35A, no.11, pp.3551-3561A.
7. D.G. Eskin, J. Zuidema (jr.), V.I. Savran, L. Katgerman, Structure formation and macrosegregation under different process conditions during DC casting, *Mater. Sci. Eng. A*, 2004, vol. 384, no.1-2, pp.232-244.
8. D.G. Eskin, J. Zuidema (jr.), V.I. Savran, L. Katgerman, Effect of process parameters on structure formation during direct-chill casting of Al-Cu alloy, *Materials Forum*, 2004, vol. 28, pp. 487-493.

Curriculum vitae

Viktoriya Ivanivna Savran

Born on 4 April 1974 in Zaporizhzhya, Ukraine

Education

- 1992 – 1997** **Diploma of mechanical engineer with honor, specialization: Materials Science**
Zaporizhzhya State Technical University (ZSTU), Ukraine
Thesis title: “Influence of refractory elements on high temperature corrosion of nickel-base superalloys”.
- 2002 – 2004** **Master of science, International MSc program: Materials science and Engineering**
TU Delft, the Netherlands.
Thesis title: “Investigation of relationship between parameters of direct chill casting and the macro and microstructures of aluminum alloys”
- 2004-2008** **PhD in Materials science**
M2i (Materials Innovation Institute); TU Delft; the Netherlands.
Thesis title: “Austenitization of C-Mn steels”

Work experience

- 1999 – 2002** Designer-engineer (design and manufacturing of Power Transformers), Scientific and Engineering center “ZTZ-Service”, Zaporizhzhya, Ukraine
- 1997 – 1999** Designer-engineer (design and manufacturing of Power Transformers, bureau of Metallic Constructions), Zaporizhzhya Transformer Corporation (ZTR), Zaporizhzhya, Ukraine
- 2008 – present** Valorization manager, M2i (Materials Innovation Institute), the Netherlands

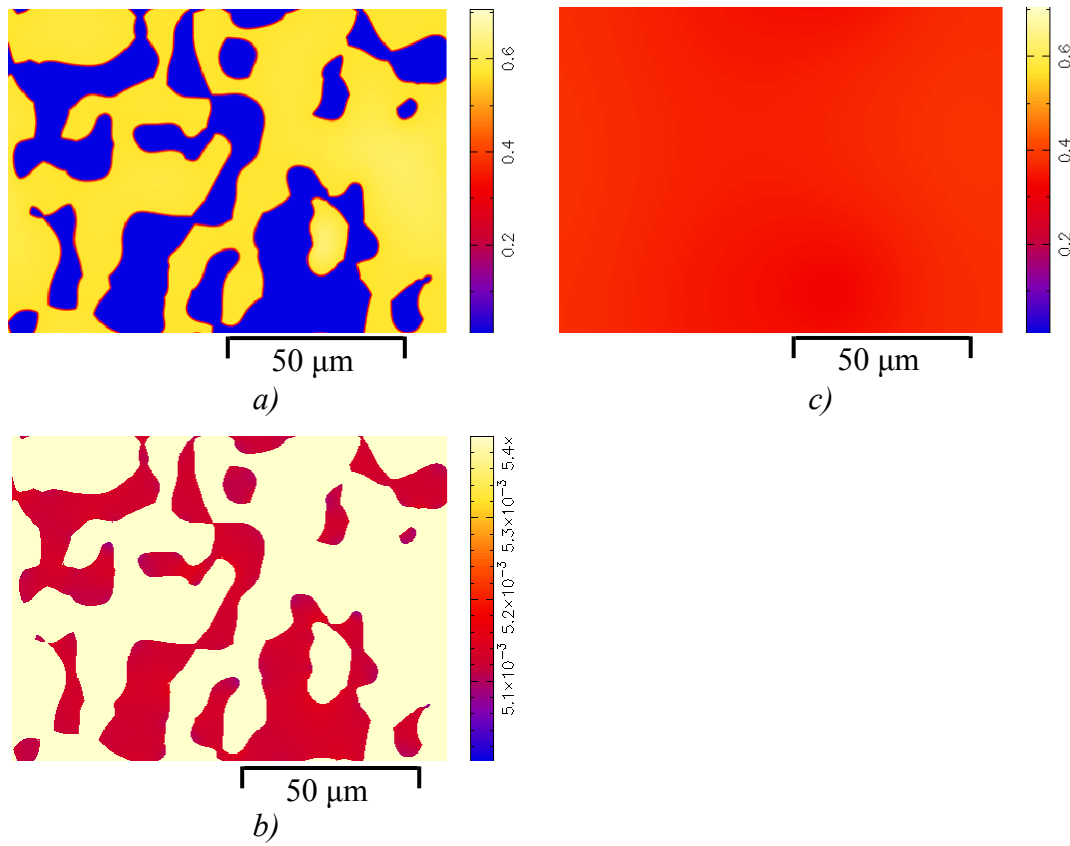


Figure 6.11. Carbon concentration maps for C35 alloy heated with 0.05 °C/s to a), b) 745 °C and c) 805 °C. b) shows the carbon gradients in the ferrite phase.

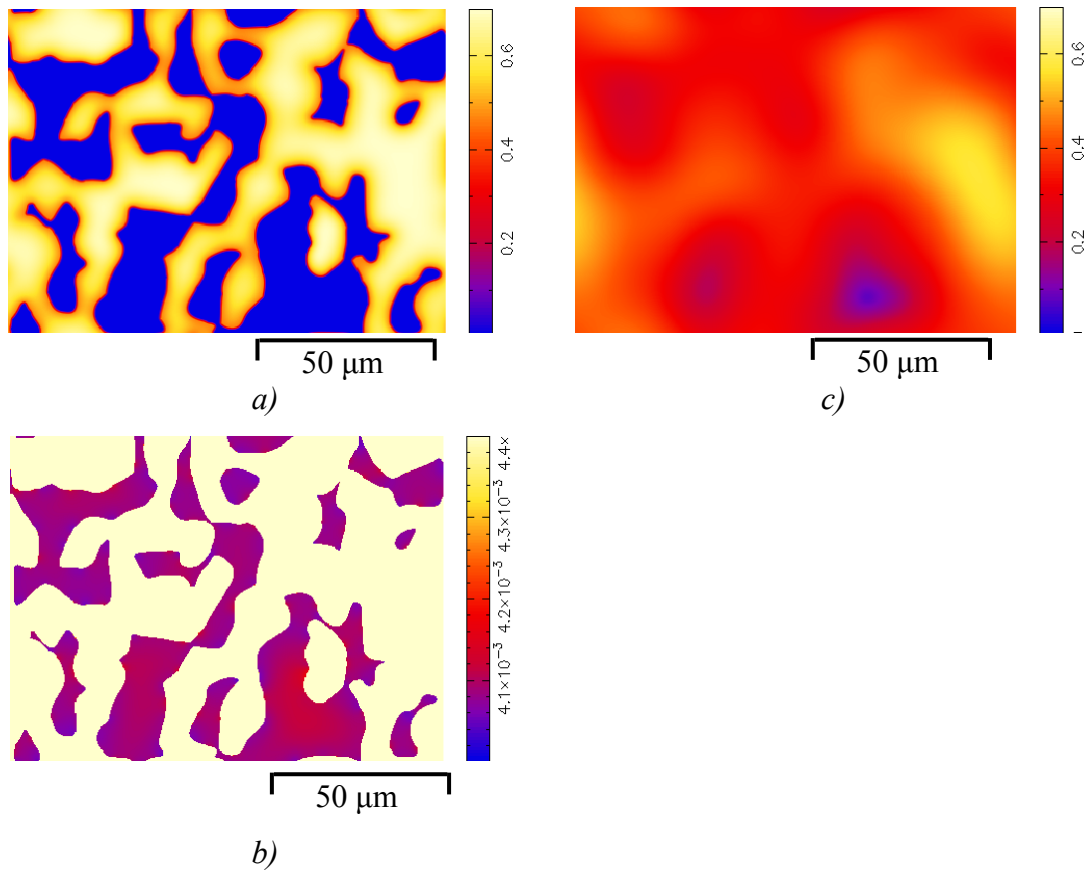


Figure 6.12. Carbon concentration maps for C35 alloy heated with 3 °C/s to a), b) 760 °C and c) 835 °C. b) shows the carbon gradients in the ferrite phase.

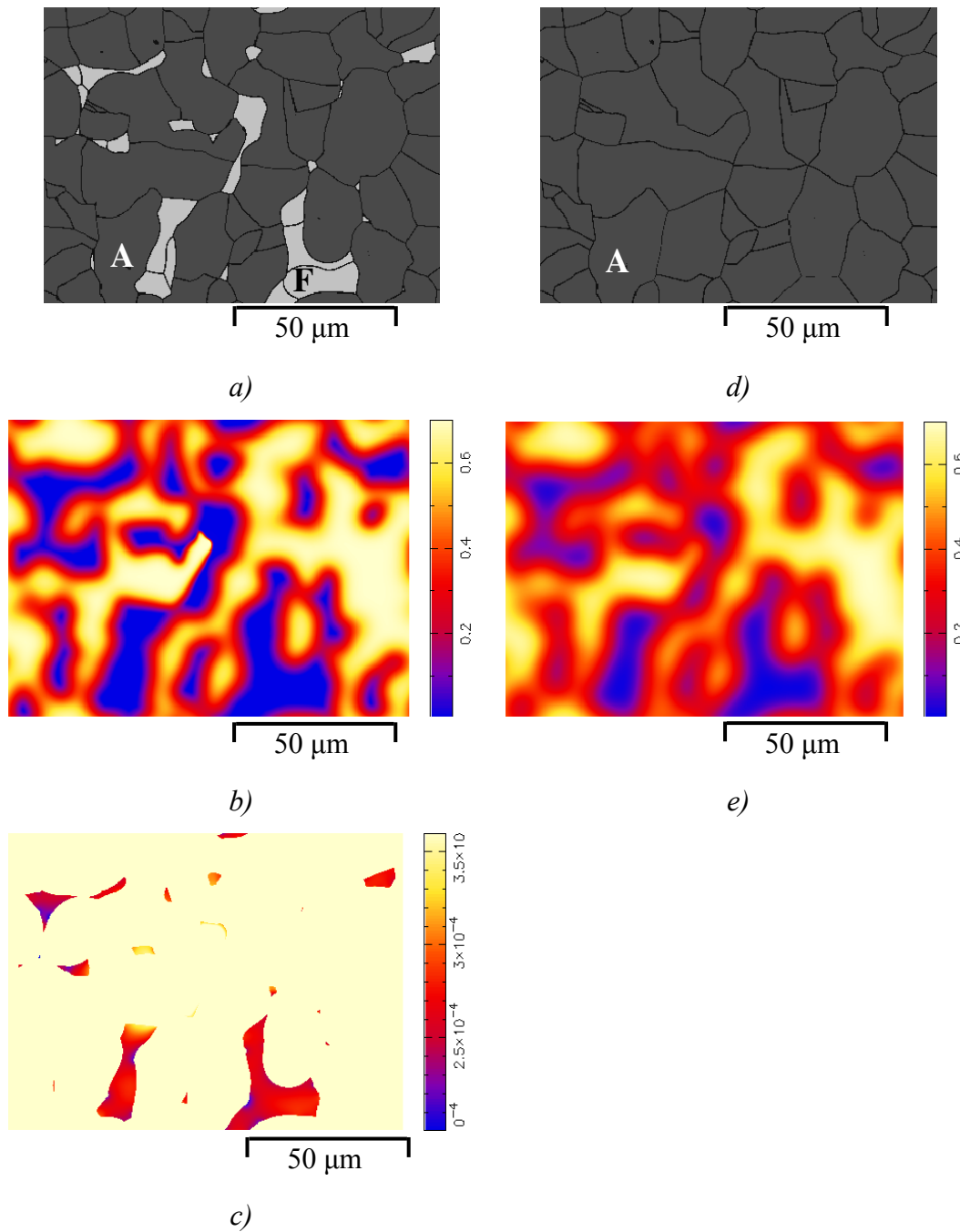


Figure 7.1. The evolution of the microstructure for the C35 alloy heated with 50 °C/s heating rate to a)-c) 850 °C and d)-e) 900 °C. a), d) show microstructures; b), e) show carbon profiles; c) shows carbon gradients in the ferrite phase. A = austenite, F = ferrite.

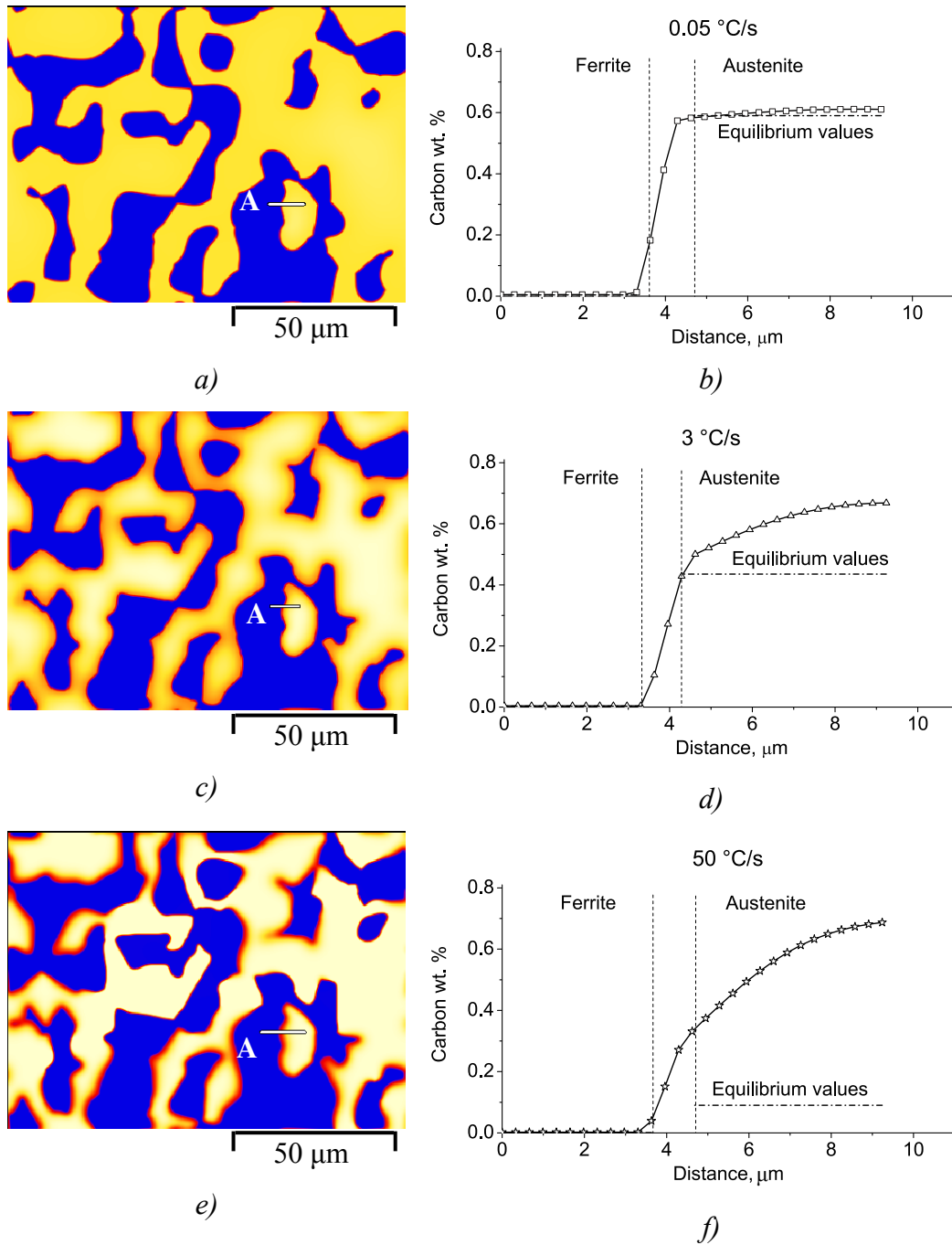


Figure 7.4. Carbon concentration maps a), c), e) and carbon profiles along the line A b), d), f) for C35 alloy at a), b) 745 °C; c), d) 762 °C and e), f) 812 °C. In a), b) alloy was heated with 0.05 °C/s; c), d) 3 °C/s and e), f) 50 °C/s heating rate.

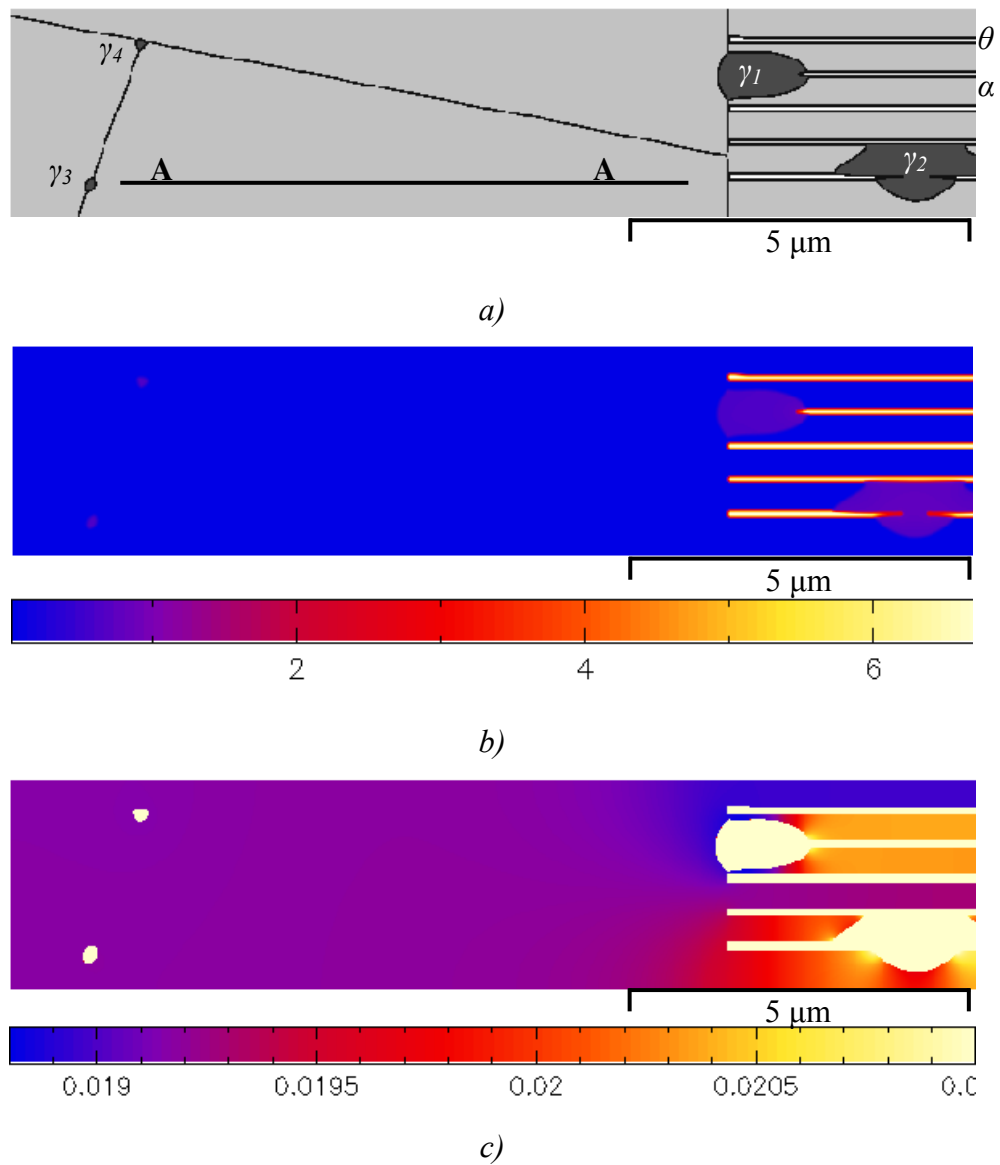


Figure 8.4. The evolution of the microstructure after 1 s of the isothermal holding at 727 °C. a) general view of the microstructure, b) general carbon redistribution profile and c) carbon gradients in ferrite. α = ferrite, γ = austenite, θ = cementite.

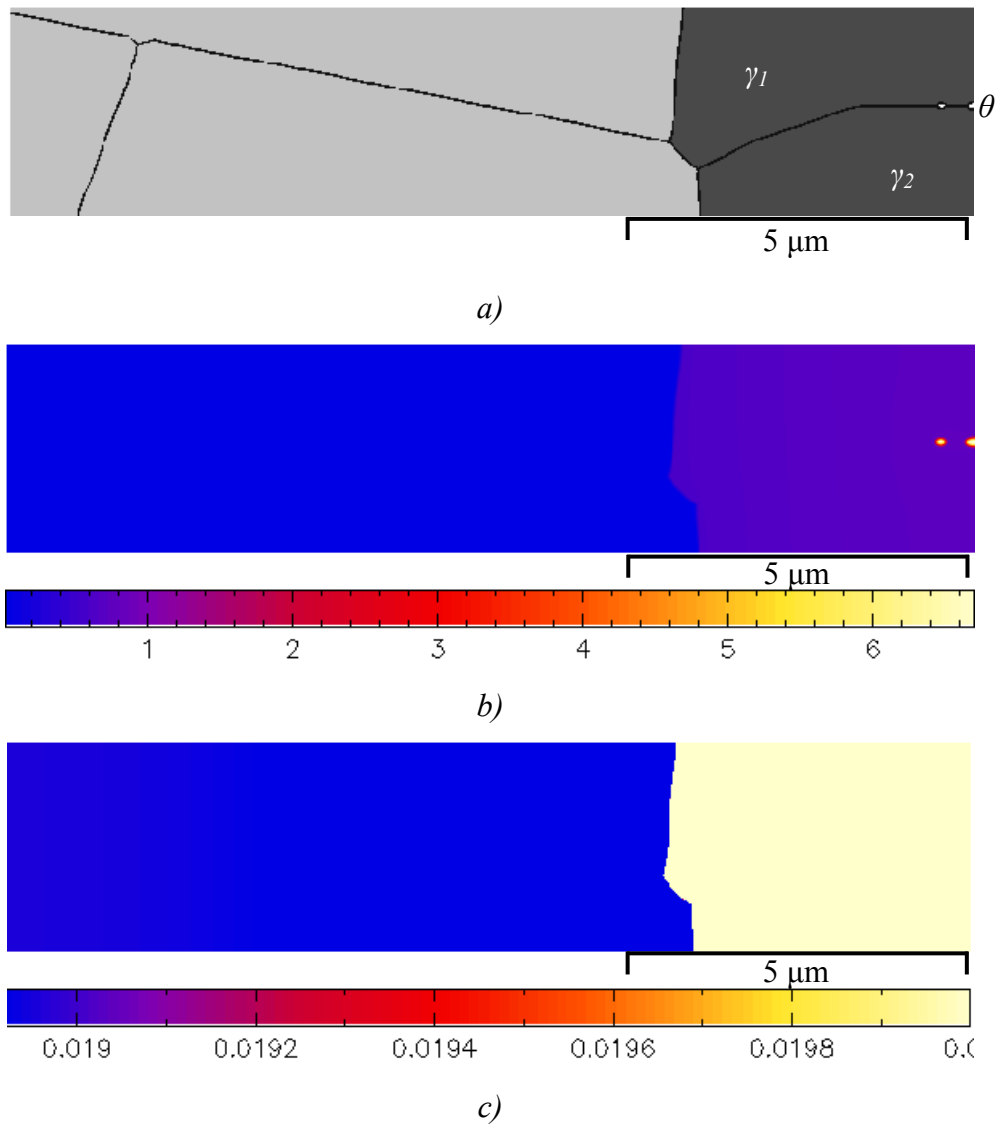


Figure 8.5. The evolution of the microstructure after 11 s of the isothermal holding at 727 °C. a) general view of the microstructure, b) general carbon redistribution profile and c) carbon gradients in ferrite. α = ferrite, γ = austenite, θ = cementite.

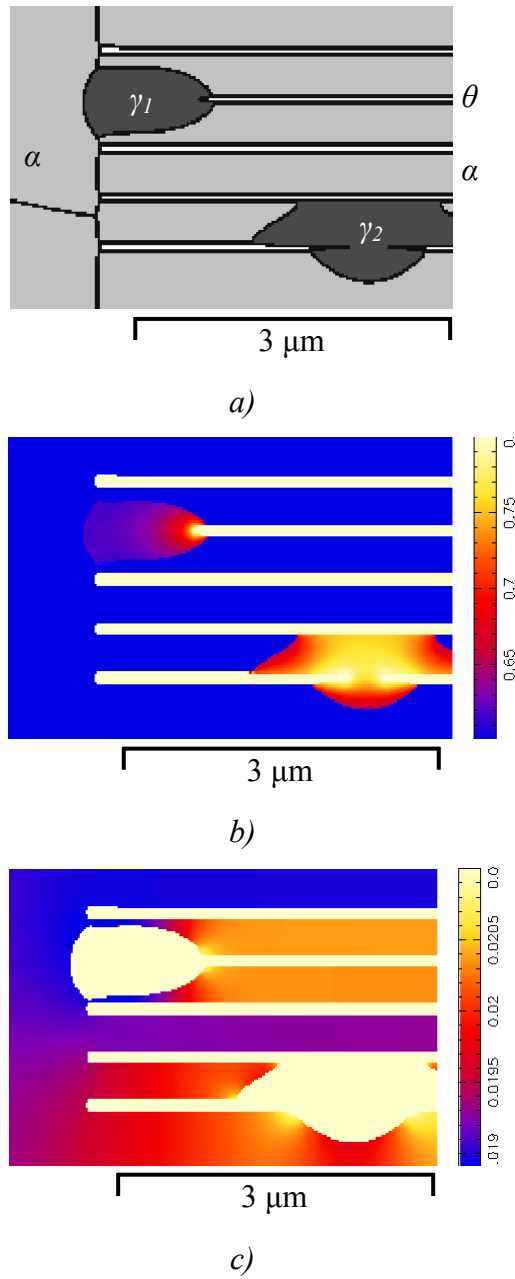
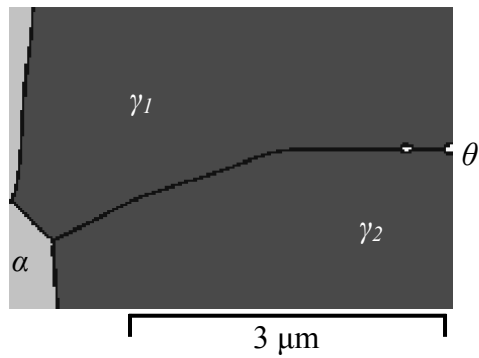
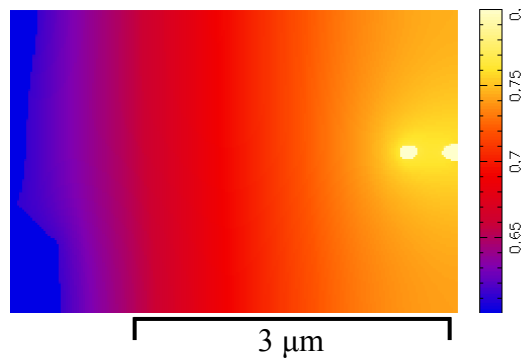


Figure 8.8. Austenite growth near the source of carbon: on the pearlite-ferrite grain boundary, γ_1 , and inside the pearlite grain on the ferrite-cementite grain boundary, γ_2 . Isothermal holding at 727 °C for 1 s. a) general view of the microstructure, b) carbon gradients in austenite and c) carbon gradients in ferrite. α = ferrite, γ = austenite, θ = cementite.



a)



b)

Figure 8.9. Austenite growth near the source of carbon: on the pearlite-ferrite grain boundary, γ_1 , and inside the pearlite grain on the ferrite-cementite grain boundary, γ_2 . Isothermal holding at 727°C for 11 s. a) general view of the microstructure and b) carbon gradients in austenite. α = ferrite, γ = austenite, θ = cementite.

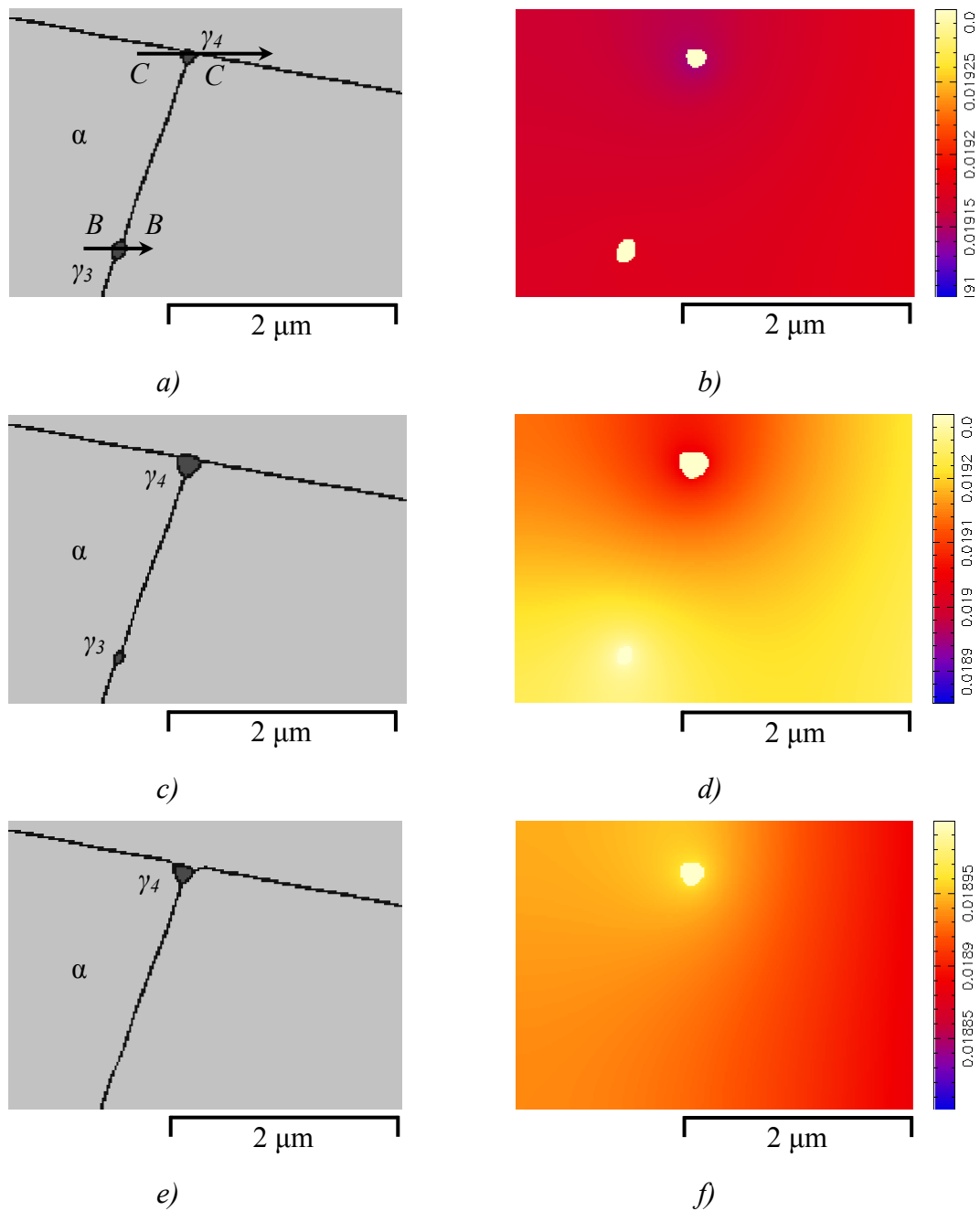


Figure 8.10. Austenite growth away from the source of carbon: on the ferrite-ferrite grain boundary, γ_3 , and triple point, γ_4 . Isothermal holding at 727 °C for. a), b) 1 s; c), d) 2.5 s and e), f) 9 s. a), c), e) general view of the microstructure and b), d), f) carbon gradients in ferrite. α = ferrite, γ = austenite.

Cover background photo:
Titel: *Rusty Curves*
Fotograaf: *Piet Osefius* (www.dutchphotoday.nl)